UNIVERSITÀ
DEGLI STUDI
DI PADOVA

Sede Amministrativa: Università degli Studi di Padova

Dipartimento di Ingegneria Civile, Edile ed Ambientale

SCUOLA DI DOTTORATO DI RICERCA IN: Scienze dell'Ingegneria Civile ed Ambientale
INDIRIZZO: via Loredan 20, 35131 Padova
CICLO XXVI

BOND BEHAVIOR IN FIBER REINFORCED POLYMER COMPOSITES AND FIBER REINFORCED CEMENTITIOUS MATRIX COMPOSITES

Direttore della Scuola: Ch.mo Prof. Stefano Lanzoni
Supervisore: Ch.mo Prof. Carlo Pellegrino
Co-Supervisore: Ch.ma Prof. Lesley H. Sneed

Dottorando: Tommaso D'Antino

Acknowledgements

The author gratefully acknowledges Prof. Carlo Pellegrino (University of Padova) for giving him the opportunity to work on this topic during his PhD studies. The author would like to thank Prof. Christian Carloni (University of Hartford) and Prof. Lesley H. Sneed (Missouri S&T) for their priceless guidance and for giving him the opportunity to perform the experimental work at Missouri S&T. The author would like to express his appreciation to the National University Transportation Center (NUTC) at Missouri S&T for providing financial support for the experimental campaign and Ruredil S.p.A. of San Donato Milanese, Italy, for providing the composite materials.

Abstract

The use of fiber reinforced composites for strengthening reinforced concrete (RC) structures has gained great popularity in the last few decades. Fiber reinforced polymer (FRP) composites represent an effective solution for strengthening existing reinforced concrete structures due to their mechanical properties and relatively low cost. FRP composites have been extensively studied, and design codes/recommendation/guidelines are available. One of the most important concerns regarding the use of FRP for strengthening RC structures is the proper design to preclude debonding failure. The bond behavior of FRP-concrete joints is studied in this thesis by means of a fracture mechanics approach, assuming that the debonding is characterized by a pure Mode II failure. The most important analytical formulations for the evaluation of the bond strength of FRP-concrete joints are analyzed and discussed. The accuracy of each analytical model studied is assessed through the use of a wide experimental database including different test set-ups and composite materials. Furthermore, the accuracy of several analytical models for the evaluation of the effective bond length, i.e. the minimum length needed to fully develop the bond strength of the FRP-concrete joint, is assessed.

A promising alternative to FRP composites is fiber reinforced cementitious matrix (FRCM) composites. FRCM composites are comprised of high strength fibers applied to the concrete substrate through the use of inorganic cementitious matrix. FRCM composites are still in their infancy, and very limited work is available in the literature. In the second part of this thesis, an extensive experimental campaign conducted on PBO FRCM-concrete joints is presented and discussed. Since the weakness of FRCM-concrete joints is located at the matrix-fiber interface, the study of the stress-transfer mechanism between the fibers and the matrix is of particular importance. Specimens with different bonded lengths and bonded widths are presented. The fracture mechanics approach used to study the FRP-concrete joints is extended to the study of FRCM-concrete joints, and the exsistence of an effective bond length similar to that observed for FRP-concrete joints is investigated. The results obtained through the fracture mechanics approach are used for the implementation of numerical models to investigate the fiber-matrix interface bond behavior for FRCM-concrete joints that include more than one layer of matrix.

Sommario

L'utilizzo di compositi fibrorinforzati per il rinforzo e l'adeguamento di strutture esistenti in calcestruzzo armato (c.a.) ha raggiunto una grande popolarità negli ultimi decenni. Tra i materiali compositi, l'utilizzo dei cosiddetti polimeri fibrorinforzati (fiber reinforced polymer, FRP) rappresenta una soluzione efficace per l'intervento su strutture esistenti in c.a. grazie all'elevata resistenza meccanica ed al costo relativamente non elevato del materiale. Gli FRP sono stati largamente studiati negli ultimi anni e sono attualmente disponibili diverse linee guida per la progettazione di questo tipo di rinforzo in tutto il mondo. Uno dei problemi di maggiore importanza nell'utilizzo di compositi FRP è costituito dalla valutazione della resistenza al distacco (debonding) del composito dal supporto su cui è applicato. In questa tesi viene analizzato il comportamento di giunti FRP-calcestruzzo nel contesto della meccanica della frattura, assumendo che la rottura per distacco sia assimilabile ad un modo di rottura di tipo II. Le più importanti formulazioni analitiche per la valutazione della resistenza d'adesione del composito al substrato sono analizzate e discusse. L'accuratezza di ognuno dei modelli analitici considerati è stata valutata per mezzo di un esteso database sperimentali in cui sono presenti i risultati di test condotti su diversi materiali compositi e con diverse configurazioni di prova. Viene inoltre valutata l'accuratezza di alcuni modelli analitici per il calcolo della lunghezza effettiva d'aderenza, cioè della lunghezza minima necessaria per poter sviluppare appieno il meccanismo di adesione FRP-calcestruzzo.

Una promettente alternativa all'utilizzo dei compositi FRP è rappresentata dai cosiddetti materiali compositi a matrice cementizia (fiber reinforced cementitious matrix, FRCM), costituiti da fibre lunghe ad alta resistenza applicate a supporti in calcestruzzo per mezzo di matrici cementizie. I compositi FRCM rappresentano una novità nel mondo del rinforzo di strutture esistenti in c.a. e la letteratura disponibile a riguardo è ancora assai limitata. Nella seconda parte di questa tesi viene presentata e discussa una vasta campagna sperimentale condotta su provini di FRCM di diversa lunghezza e larghezza costituiti da fibre in PBO e matrice cementizia applicata su supporti in calcestruzzo. Dal momento che la rottura nei giunti FRCM-calcestruzzo avviene all'interfaccia fibra-matrice, lo studio del meccanismo di trasmissione degli sforzi da fibra a matrice è di particolare importanza in questi compositi. L'approccio di meccanica della frattura applicato nel caso di giunti FRP-calcestruzzo è esteso al caso dei compositi FRCM ed è indagata la possibile esistenza di una lunghezza effettiva d'aderenza simile a quella osservata nei compositi FRP. I risultati ottenuti dall'approccio di meccanica della frattura sono utilizzati per l'implementazione di modelli numerici che permettono di studiare il comportamento di adesione fibra-matrice in compositi che includano più di uno strato di matrice cementizia.

Summary

INTRODUCTION

In the last few decades, the construction industry has witnessed a rapid growth of interest regarding strengthening and retrofitting of existing reinforced concrete (RC) structures.

In general, each structure should be designed to fulfill the purpose for which it was built for a certain amount of time, guaranteeing certain safety standards. Nevertheless, a growing number of RC structures need rehabilitation or strengthening because of improper design or construction, change of the design loads, damage caused by environmental and/or human factors, seismic events, etc. Several different systems have been developed and used to strengthen existing RC structures. They include replacing structural members, adding new material to improve their performance, modifying the restraint conditions, introducing post-tension, etc. These techniques have been proven to be effective, but in some cases they can be quite expensive and difficult to apply. The use of fiber reinforced composites externally-bonded (EB) to existing structural elements may represent a cost-effective alternative to such traditional strengthening techniques.

Among fiber reinforced composites, strengthening by means of fiber reinforced polymers (FRP) has gained great popularity in the last decades because of its high mechanical properties and relatively low cost. FRP composites are comprised of high strength fibers (usually carbon, glass, or aramid), applied to the concrete surface through thermosetting organic matrices, usually epoxy resin. The fibers are meant to carry the tensile forces, whereas the matrix transfers the stress to the concrete support. They are easy to install, have a high strength-to-weight ratio, and have suitable mechanical properties. Although a large number of experimental, analytical, and numerical studies regarding FRP composites are available in literature, there are issues still under discussion within the scientific community. Among them, debonding of the FRP composite from the concrete substrate is the most important concern in this type of application. Furthermore, high temperature and fire exposure, deterioration due to UV exposure, and lack of permeability with respect to the concrete support represent other important issues strictly related to the organic matrices employed.

Promising newly-developed types of matrix that potentially overcome the limits of FRP composites and represent a valid alternative to polymeric matrices are the so-called inorganic matrices. Composite materials that employ modified cement-based inorganic matrix are usually referred to as fiber-reinforced cementitious matrix (FRCM) composites. The literature regarding FRCM composites is still very limited, and no design codes/recommendations are available. The studies available on FRCM-concrete joints report that the weakness is located at the matrix-fiber interface rather than within the substrate or at the matrix-concrete interface, as is typically observed with FRP composites. This could have potential benefits in certain structural strengthening or hardening applications that rely on ductility or energy dissipation, such as seismic retrofitting.

In the case of both FRP- and FRCM-concrete joints debonding of the composite from the substrate is the most important and dangerous failure mode because of its brittle nature. It occurs with no warning at stress levels significantly lower than the strength of the strengthening composite.

In this work the bond mechanism between fiber reinforced composites and concrete support is investigated. The most important existing bond models for the evaluation of the FRP-concrete bond strength were assessed through the use of a wide experimental database collected from the literature. The database allowed to measure the accuracy of each analytical model in evaluating the FRP-concrete bond strength.

A wide experimental campaign including single- and double-lap direct-shear tests on FRCM-concrete joints is presented and discussed. Following the approach used to study the FRP-concrete bond properties, the experimental results were used to study the interaction between FRCM composites and concrete substrate. In particular, a fracture mechanics approach was adopted to describe the load-slip behavior of FRCM-concrete joints. Numerical modeling of the experimental results confirm the findings and the analytical formulations put forth during this work.

1 FRP COMPOSITES FOR STRENGTHENING RC STRUCTURES

1.1 Abstract

In the last few decades, fiber reinforced polymer (FRP) composites have been extensively used for strengthening and retrofitting existing reinforced concrete (RC) structures. The weakness of FRP strengthened RC elements is reported to be within a thin layer of the concrete substrate. The stress-transfer mechanism between the externally bonded (EB) FRP and the concrete substrate was investigated by several authors, and a great number of scientific contributions are available in the literature. In this chapter the stress-transfer mechanism of FRP-concrete joints will be presented and discussed. The single-lap direct-shear test is used to study the load response FRP-concrete joints. Starting from the single-lap direct-shear test, a fracture mechanics approach is used to derive the equations that describe the bond behavior of FRP-concrete joints.

1.2 Introduction

The use of fiber reinforced polymer (FRP) composites for strengthening reinforced concrete (RC) structures has gained popularity in the last few decades. FRP composites are comprised of high strength fiber applied to concrete substrates by means of thermosetting organic matrices. The most common fibers employed in FRP composites are carbon, glass, and aramid fiber, whereas the most common matrices are epoxy resins. Fibers are usually applied in the form of a continuous pre-impregnated sheet (laminate), or a continuous dry sheet that is impregnated in situ (post-impregnated sheet).

Several experimental, analytical, and numerical works available in literature have shown that the use of FRP for strengthening RC structural members is an effective technique for flexural strengthening (e.g. [94, 85, 82, 60]), shear strengthening (e.g. [110, 66, 86, 87, 83, 90]), and confinement of elements mostly subjected to compressive load (e.g. [83, 67, 90, 59]). Some of these studies resulted in the formulation of design codes, recommendations, and guidelines, e.g. the European *fib* Bulletin 14-2001 [48], the Italian CNR-DT 200/2004 [36], and the American ACI 440.2R-08 [6]. Nevertheless, some issues concerning the behavior of FRP composites are still under discussion. In particular, debonding of the composite from the concrete substrate is the most important concern in this application because it is a brittle phenomenon that may happen with no visible warning at load levels significantly lower than the tensile strength of the composite. Considering a RC beam retrofitted with FRP composites (laminates or

sheets), two main types of debonding can be recognized (Figure 1): 1) plate end interfacial debonding (indicated as mode 1 in CNR-DT 200/2004 [36]) or cover delamination (as termed in ACI 440.2R-08 [6]), which typically occurs at the end of the FRP strip and mostly involves the concrete cover. Several authors studied the plate end debonding and concluded that it can be prevented through the use of anchorages at the ends of the FRP strip [52], for example in the form of FRP stirrups [33]. 2) Intermediate crack-induced debonding, which may start at flexural cracks (indicated as mode 2 in CNR-DT 200/2004 [36]), or flexural-shear cracks (indicated as mode 3 in CNR-DT 200/2004 [36]). Intermediate crack-induced debonding usually takes place within a thin layer of concrete, rich of mortar, in which the epoxy impregnated the substrate, and does not propagate into the concrete cover [26]. Since plate end debonding failure can be prevented by applying anchorages at the end of the FRP reinforcement, many researchers have concentrated on the study of intermediate crack-induced debonding. Codes, recommendations, and guidelines commonly accepted in different countries currently limit the value of the strain in the FRP strengthening in order to prevent the intermediate crack-induced debonding. Nevertheless, several different analytical formulations for the evaluation of the FRP-concrete bond strength are available, and the discussion is still open.

In this chapter the bond behavior of FRP-concrete joints will be described and discussed. The cohesive nature of the debonding process will be studied using a fracture mechanics approach, and the assumptions on which the codes, recommendations, and guidelines are based are presented and discussed showing the need of further investigation and discussion.

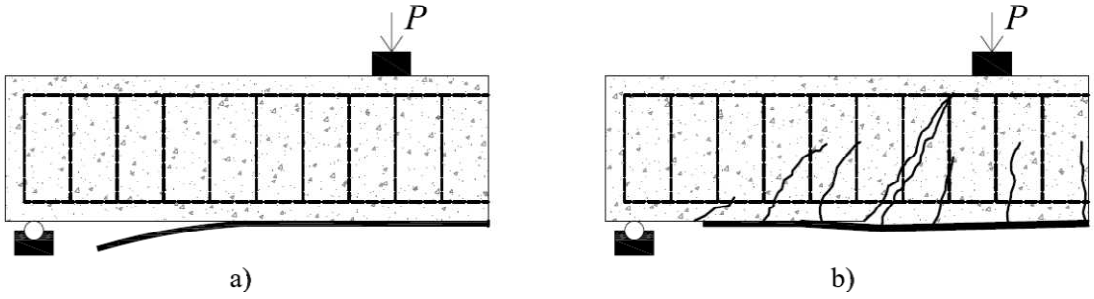

Figure 1. a) Plate end interfacial debonding. b) Intermediate crack-induced debonding.

1.3 Experimental test set-ups

The bond behavior of FRP-concrete joints can be studied using different types of experimental test set-ups. Certainly, full-scale flexural beam tests represent the most reliable and effective tests [96, 92] to study the FRP bond behavior and to assess the effectiveness of the FRP strengthening in enhancing the beam flexural strength. However, full-scale beam tests are expensive, and the investigation of the FRP-concrete bond behavior is complicated by the presence of various strength mechanisms, i.e. the

load sharing between the internal reinforcing steel and the externally bonded (EB) FRP composite, and the crack-pattern that is difficult to predict and has a strong influence on the beam overall behavior. For these reasons, Chajes et al. [31], Taljsten [103], and Bizindavyi and Neal [18] were among the first to employ a single-lap direct-shear test to investigate the bond properties of FRP reinforcement. A single-lap direct-shear test is comprised of one or more layers of FRP strips bonded to one surface of a concrete prism (Figure 2). During single-lap tests the eccentricity between the FRP composite and the concrete prism generates a flexural moment that may influence the results. Some authors [118] analyzed the effect of the flexural moment in single-lap direct-shear test concluding that the influence of a small loading angle can be neglected for long bonded length. Nevertheless, to overcome this issue, a double-lap direct-shear test was used by some researchers to study the bond behavior of FRP-concrete joints under shear stress only. Double-lap direct-shear tests are comprised of two concrete prisms jointed through two FRP composites bonded on opposite faces of the prisms (Figure 2). Other than the direct-shear tests, a small-scale flexural beam test was proposed. In small-scale flexural beam tests the FRP composite is applied to the tensile face of a small-scale concrete beam in which a hinge or a notch is provided in order to initiate debonding at a specific cross-section (Figure 2). A study of the influence of the test set-up on the composite bond behavior can be found in [32, 34, 118]. The debate about which test set-ups are suitable to capture the complex stress transfer mechanism between FRP composites and the concrete substrate is still open. Nevertheless, it is recognized that the direct-shear tests are appropriate to capture the debonding phenomenon [27]. Furthermore, the use of small-scale flexural beam test is arguable because the results are strongly influenced by different mechanism developing in small-scale beams respect to full-scale beams, e.g. the size effect, the presence of friction that cannot be neglected in small-scale specimens, etc.

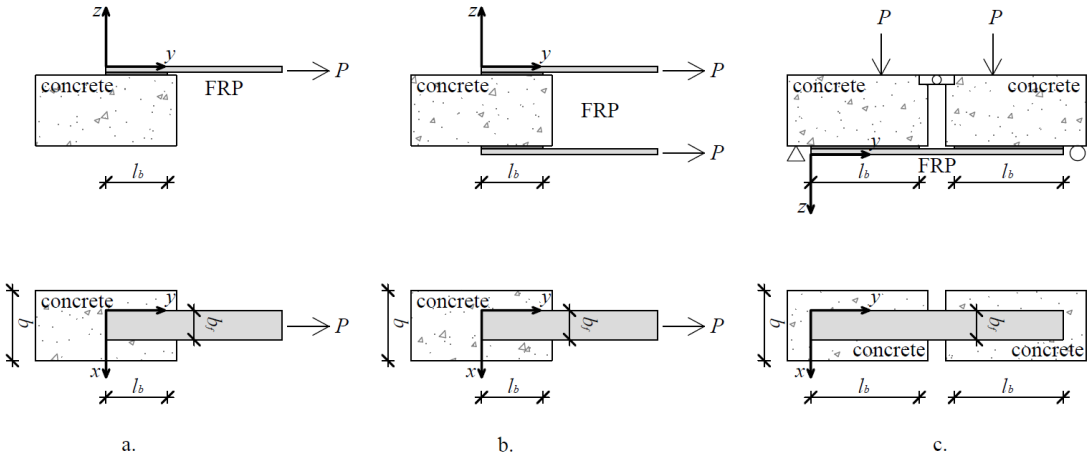

Figure 2. Test set-ups for the evaluation of the FRP-concrete bond strength. a. Single-lap direct-shear test set-up. b. Double-lap direct-shear test set-up. c. Small-scale flexural beam test-set-up.

1.4 Idealized load response of FRP-concrete joints

In a single-lap direct-shear test of an FRP-concrete joint, the FRP composite is pulled while the concrete prism is restrained against movement; this configuration is also known as near-end supported single-shear test [118]. During the test the force applied to the FRP composite, termed P, is measured. The relative displacement between the concrete prism and the FRP composite is measured by means of two displacement transducers placed at the edge of the composite at the end of the composite bonded length. The average between the displacement measured by the transducers is used to control the test and is named global slip g. Since debonding failure is a brittle phenomenon, the test must be carried out in displacement control using an increasing rate of the global slip sufficiently small to capture the debonding crack growth.

In Figure 3 the idealized Applied Load vs. Global Slip response of an FRP-concrete joint with a relatively long bonded length is reported. The load response is characterized by an initial linear-elastic increasing response of the applied load up to point A. A nonlinear response is then observed between point A and point B. The region AC is characterized by the initiation of the debonding crack, as it will be shown through the analysis of the FRP strain presented in the next section (§1.5). Finally, after point B the applied load remains constant until point C. Considering FRP-concrete joints with different bonded length it is possible to recognize different load responses. The maximum applied load P_{max} increases with the increase of the FRP composite bonded length up to a limiting value $\overline{P}_{max}$. Further increasing of the bonded length provides the same value of the maximum load $P_{max} = \overline{P}_{max}$ and only results in the extension of the constant branch BC. This result suggests the existence of a bond length beyond which no further enhancement of the maximum applied load is possible. This length is referred to as the *effective bond length* l_e [32] or the *development length* [6]. The concept of effective bond length will be further clarified in the next section.

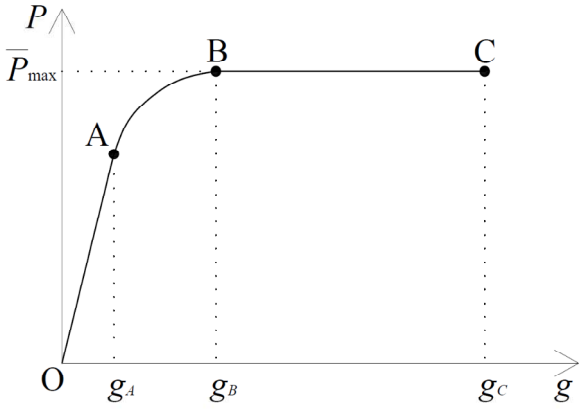

Figure 3. Idealized Applied Load P vs. Global Slip g behavior of an FRP-concrete joint with long bonded length.

1.5 Strain analysis of FRP-concrete joint subjected to direct-shear test

In order to study the stress-transfer mechanism between the EB FRP composite and the concrete substrate, the strain profile along the FRP bonded length is analyzed. The strain can be measured by means of strain gauges applied over the composite surface or through the use of an optical technique known as Digital Image Correlation [101, 100]. The Digital Image Correlation (DIC) technique is able to capture the strain profile over the whole composite surface area and enables the study of the stress-transfer mechanism both along the length and the width of the composite [99].

Figure 4 shows the idealized strain profiles along the bonded length for points of the load response included in the regions depicted in Figure 3. As it can be seen, the strain distributions for any points along the bonded length are essentially equal to zero toward the free end. A rapid increase in the strain value can be seen toward the loaded end. The strain levels off at a value $\bar{\varepsilon}_{max}$ that remains nominally constant for any further increase of the global slip g, which is consistent with the observation that the applied load does not increase after the onset of debonding (Figure 3). Analysis of the strain profiles for different values of the applied load shows that the strain attains the maximum value $\bar{\varepsilon}_{max}$ when the applied load attains the maximum value $\overline{P}_{max}$. Thus, any points of the load response after point B are characterized by a complete (fully established) "S" shape of the strain profile. In other words, the stress transfer zone (STZ), which is the zone corresponding to the complete development of the "S" shape in the strain profile [99], is fully established when the applied load attains the maximum value $\overline{P}_{max}$ (Point B). Further increments of the global slip after g_B result in the translation of the STZ toward the unloaded end, indicating a self-similar growth of the debonding crack. According to these observations, the effective bond length l_e of the FRP-concrete joint can be evaluated by measuring the amplitude of the STZ, i.e. measuring the distance between the positions along the bonded length for which the strain is nominally equal to zero and equal to $\bar{\varepsilon}_{max}$. The length along which the strain is equal to $\bar{\varepsilon}_{max}$ corresponds to the debonded length l_{deb} (Figure 4).

It should be noted that for points of the load response after point C in Figure 3 the STZ is no longer fully established because the portion of the bonded length that is not cracked yet is shorter than the effective bond length. Any increment of the global slip beyond g_C determines a different failure pattern with respect to the failure pattern observed for points within the region OC [27, 28].

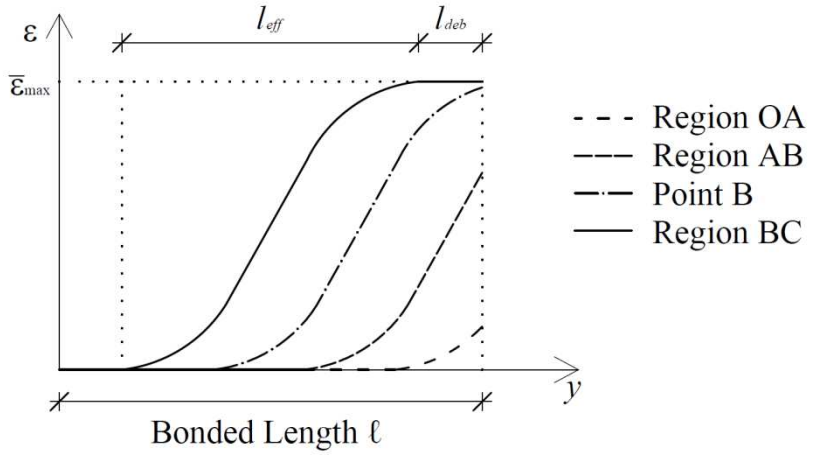

Figure 4. Idealized strain profile along the bonded length for the regions depicted in Figure 3.

In the majority of the studies available in the literature the strain profiles of FRP-concrete joints are measured through the use of strain gauges placed in proximity to the center of the FRP composite. Some researchers studied the strain profiles of FRP composites both along the bonded length l_b and the bonded width b_f [99, 89]. They observed that the longitudinal strain ε_{yy} decreases towards the composite edges, and it is possible to recognize a central area of the composite over which ε_{yy} remains nominally constant across the width b_f. Normalizing the applied load over the FRP area ($\sigma_{yy} = P/b_f t_f$) they observed an increase of σ_{yy} as the ratio between the composite width b_f and the concrete surface width b increases. The increase of the central region in which ε_{yy} is nominally constant is responsible for the increasing of the normalized applied load σ_{yy}. However, some researchers [32, 118] reported results that contradict the conclusion reported in [99, 89]. According to Chen and Teng [32] and Yao et al. [118] σ_{yy} decreases with an increase of the FRP-to-concrete width ratio b_f/b. Chen and Teng 2001 [32] proposed a corrective coefficient β_p that takes into account this strength reduction effect. It should be noted that the test results reported by Chen and Teng 2001 [32] were conducted on specimens with a wide bonded width (greater than 25.4 mm), whereas the observation made by Subramaniam et al. 2005 [99] was based on the results of specimens with bonded widths within 12 mm and 46 mm. Furthermore, part of the data reported in [32] were obtained from tests in which steel plates were employed instead of FRP composites.

1.6 Mode II fracture mechanics approach

Debonding of FRP may occur within the concrete substrate, at the FRP-concrete interface, or at the fiber-matrix interface. As discussed in §1.2, intermediate crack-induced debonding takes place within a small layer of the concrete substrate. For this

reason, it is reasonable to study the debonding process within the framework of fracture mechanics applied to the quasi-brittle behavior of the concrete. Both Linear Elastic Fracture Mechanics (LEFM) and Nonlinear Fracture Mechanics (NLFM) were used to describe the debonding crack growth process [104]. Although LEFM should not be applied in concrete due to the presence of nonlinearity such as hardening and softening, the definition of a Fracture Process Zone (FPZ) allows the nonlinearity of the material to be taken into account and apply LEFM for quasi-brittle material [17, 27]. The FPZ represents a bridging zone between the uncracked and cracked material where progressive softening occurs [27]. The FPZ is a function of the material characteristics; in quasi-brittle material it is close in size with the region of nonlinearity, whereas in other material it can be mostly associated with the nonlinear hardening region (e.g. steel). In concrete the FPZ represents the region in which the microcracks coalesce giving continuity to the crack propagation. The FPZ in concrete can be described through the use of a simple cohesive crack model [62].

LEFM was used to describe the FRP debonding process considering a pure Mode II fracture process. The interface between the FRP composite and the concrete substrate is idealized as a zero-thickness layer characterized by well-defined mechanical properties [12, 116, 72]. It should be noted that the debonding crack does not follow an ideal path parallel to the FRP composite but follows a complicated path, related to the position of the aggregates and to the mixed-mode nature of the fracture process at the micro-scale, that requires the least amount of energy [53, 54]. Nevertheless, it can be assumed that at the micro-scale the debonding crack is subjected to a pure Mode II loading condition.

A cohesive material law is used to describe the relationship between the interfacial shear stress τ_{zy} and the corresponding relative slip s. It should be pointed out that the interfacial cohesive law $\tau_{zy}(s)$ defines the behavior of a fictitious interface that links the FRP composite and the concrete substrate. The shear stress acting through the depth of the concrete substrate is not related to the $\tau_{zy}(s)$ model. Although the stress state in concrete could have an influence on the stress-transfer mechanism [2], the LEFM model introduced describes the debonding process at the macro-scale and should not be affected by the stress field in concrete at the micro-scale.

Several authors attempted to estimate the cohesive interfacial law using different techniques. Ali-Ahamad et al. [12] employed DIC measurements to develop an experimental procedure to directly determine the cohesive interfacial law provided the FRP composite strain field. Ferracuti et al. [47], Mazzotti et al. [72], Carrara et al. [28] identified the $\tau_{zy}(s)$ law employing the measurements of strain gauges applied on the FRP-concrete joints subjected to single-lap direct-shear tests. Analogously, Pellegrino et al. [89] and Pellegrino and Modena [88] used double-lap direct-shear tests on specimens equipped with strain gauges to study the effect of the composite stiffness on the cohesive interfacial law. All these works adopted the fracture mechanics approach originally proposed by Taljsten [104] where a energy criterion is applied to identify the fracture energy associated with the crack growth.

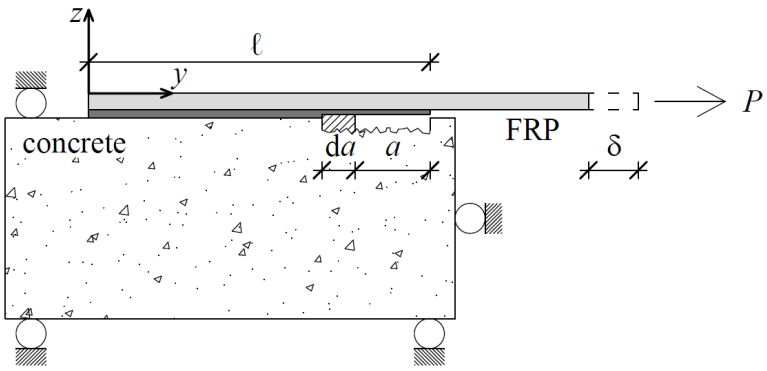

Figure 5. Evolution of the interfacial crack in single-lap direct-shear test.

Considering a single-lap direct-shear test as represented in Figure 5, the following assumptions are made: i) the FRP composite is homogenous and linear elastic; ii) the interface is subjected to pure Mode II loading condition; iii) the thickness and width of the FRP composite is constant along the bonded length; iv) the interface between the FRP and the concrete is assumed to be of infinitesimal thickness. For an interfacial crack of length a that propagates for a length da (Figure 5), the energy release rate G per unit width b_f of the composite can be written as:

$$G = \frac{1}{b_f}\frac{\mathrm{d}(F - U_e)}{\mathrm{d}a} \tag{1}$$

Where U_e is the elastic energy, and F is the work done by the applied load P. As a consequence of the application of the load P, the loaded end of the strip undergoes a relative displacement δ. Hence, the work done by the applied load P is equal to $P \cdot \delta$ and Eq. (1) becomes:

$$G = \frac{1}{b_f}\left(P\frac{\mathrm{d}\delta}{\mathrm{d}a} - \frac{\mathrm{d}U_e}{\mathrm{d}a}\right) \tag{2}$$

Since the FRP is linear elastic, the applied load can be written as:

$$P = K \cdot \delta = \frac{\delta}{C} \tag{3}$$

Where K is the stiffness of the FRP while C is its compliance. When the interface crack propagates it holds:

$$G = \frac{1}{b_f}\frac{P^2}{2}\frac{\partial C}{\partial a} \tag{4}$$

Eq. (4) can also be written as:

$$P = \sqrt{2 b_f G \Big/ \frac{\partial C}{\partial a}} \tag{5}$$

If the concrete deformation is neglected and the adhesive layer is idealized as a zero-thickness element, Eq. (6) is valid:

$$\frac{\partial C}{\partial a} = \frac{1}{b_f t_f E_f} \tag{6}$$

Where t_f and E_f are the FRP thickness and elastic modulus, respectively. When debonding propagates, the energy release rate G per unit width b_f represents the energy required to create and fully break the elementary unit area of the cohesive crack [27], i.e. the fracture energy $G_F = G$. Substituting Eq. (6) into Eq. (5) the relation between the applied load and the fracture energy G_F can be obtained [119, 117, 115]:

$$P = b_f \sqrt{2 \cdot G_F \cdot E_f \cdot t_f} \tag{7}$$

The same relations shown by Taljsten [104] can be obtained with a similar procedure based on the equality of the internal and external work in case of an FRP-concrete joint [61, 49, 69]. For the single-lap direct-shear test represented in Figure 5, the axial displacement of the concrete can be neglected because in most cases it is very small compared with the axial displacement of the FRP strip [120]. For this reason, the problem can be reduced to the equilibrium of an FRP segment of infinitesimal length $\mathrm{d}y$ (Figure 6). The axial stress in the FRP strip and the relative slip between FRP and concrete are denoted with $\sigma_{yy}(y)$ and $s(y)$, respectively. Since the axial displacement of the concrete is neglected, the relative slip $s(y)$ coincides with the axial displacement of the FRP strip.

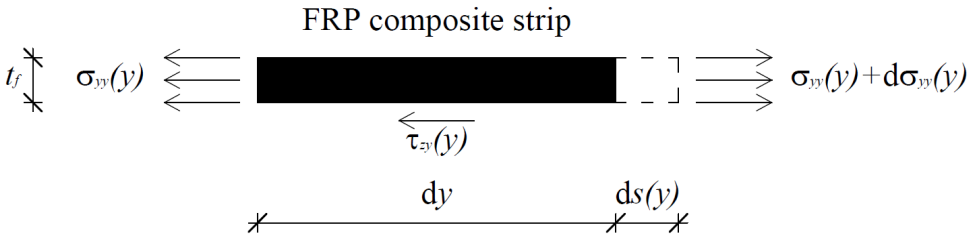

Figure 6. Equilibrium of an infinitesimal segment of fiber of length *dy*.

The equilibrium, constitutive, and compatibility equations can be written as:

$$\left(\sigma_{yy}(y) + \mathrm{d}\sigma_{yy}(y) - \sigma_{yy}(y)\right) \cdot b_f t_f = \tau_{zy}(y) \cdot b_f \cdot \mathrm{d}y \tag{8}$$

$$\sigma_{yy}(y) = E_f \cdot \varepsilon(y) \tag{9}$$

$$\frac{\mathrm{d}s(y)}{\mathrm{d}y} = \frac{\sigma_{yy}(y)}{E_f} \tag{10}$$

Where $\tau_{zy}(y)$ and $\varepsilon(y)$ are the interfacial shear stress and the FRP axial strain, respectively. Considering the fiber segment represented in Figure 6 as a free-body, the work done by the external forces can be written as:

$$\mathrm{d}W_{ext} = \left[\left(\sigma_{yy}(y) + \mathrm{d}\sigma_{yy}(y)\right)\cdot\left(s + ds\right) - \sigma_{yy}(y)\cdot s\right]\cdot b_f \cdot t_f - \tau_{zy}(y)\cdot b_f \cdot \mathrm{d}y \tag{11}$$

Neglecting the terms of higher order and substituting Eq. (8), Eq. (11) can be written as:

$$\mathrm{d}W_{ext} = \sigma_{yy}(y)\cdot b_f \cdot t_f \cdot \mathrm{d}s \tag{12}$$

From Eq. (8), Eq. (13) can be obtained:

$$\mathrm{d}\sigma_{yy}(y)\cdot b_f \cdot t_f = \tau_{zy}(y)\cdot b_f \cdot \mathrm{d}y \tag{13}$$

$$\sigma_{yy}(y)\cdot b_f \cdot t_f = b_f \int_0^y \tau_{zy}(y)\,\mathrm{d}y \tag{14}$$

Applying Eq. (14), Eq. (12) can be written as:

$$\mathrm{d}W_{ext} = b_f \int_0^y \tau_{zy}(y)\,\mathrm{d}y \cdot \mathrm{d}s = b_f \int_0^s \tau_{zy}(s)\,\mathrm{d}s\,\mathrm{d}y \tag{15}$$

Let Π be the bonded area of the FRP composite, i.e. $\Pi = \int_0^y b_f\,\mathrm{d}y$. Integrating Eq. (15) over Π:

$$W_{ext} = b_f \int_0^y \left(\int_0^s \tau_{zy}(s)\,\mathrm{d}s\right)\mathrm{d}y \tag{16}$$

Let:

$$G(s) = \int_0^s \tau_{zy}(s)\,\mathrm{d}s \tag{17}$$

Eq. (17) represents the area under the $\tau_{zy} - s$ curve. Let s_d be the slip corresponding to the complete separation of the interface. When $s = s_d$ Eq. (17) provides the fracture energy G_F, which is the energy required to create and fully break the elementary unit area of the cohesive crack [27]. Thus $G_F = G(s_d)$.

The work done by the internal forces in the infinitesimal segment of FRP is defined by:

$$\mathrm{d}W_{\mathrm{int}} = \int_0^{\varepsilon(y)} \sigma_{yy}(y)\,\mathrm{d}\varepsilon \tag{18}$$

Let $\Psi = \int_0^y b_f \cdot t_f\,\mathrm{d}y$ be the volume of the FRP segment from 0 to y. Integrating Eq. (18) over the volume Ψ we obtain:

$$W_{\text{int}} = b_f \cdot t_f \cdot \int_0^y \left(\int_0^{\varepsilon(y)} \sigma_{yy}(y)\, \mathrm{d}\varepsilon \right) \mathrm{d}y = \frac{b_f \cdot t_f}{2 \cdot E_f} \int_0^y \sigma_{yy}{}^2(y)\, \mathrm{d}y \tag{19}$$

Since the internal work and the external work must be equal:

$$\frac{b_f \cdot t_f}{2 \cdot E_f} \int_0^y \sigma_{yy}{}^2(y)\, \mathrm{d}y = b_f \int_0^y G(s)\, \mathrm{d}y \tag{20}$$

$$\int_0^y \left(\frac{b_f \cdot t_f}{2 \cdot E_f} \sigma_{yy}{}^2(y) - b_f \cdot G(s) \right) \mathrm{d}y = 0 \tag{21}$$

Eq. (21) must be satisfied for each length $0 \le y \le l_b$, which implies:

$$\frac{b_f \cdot t_f}{2 \cdot E_f} \sigma_{yy}{}^2(y) - b_f \cdot G(s) = 0 \tag{22}$$

Applying Eq. (9) for $y = l_b$, Eq. (22) gives:

$$P = b_f \sqrt{2 \cdot G(s) \cdot E_f \cdot t_f} \tag{23}$$

When $s = s_d$, i.e. onset of debonding, Eq. (23) provides the relation between the theoretical debonding load P_{deb} (also referred to as the theoretical load carrying capacity of the FRP-concrete interface), and the fracture energy of the interface G_F (Eq. (24)).

$$P_{deb} = b_f \sqrt{2 \cdot G_F \cdot E_f \cdot t_f} \tag{24}$$

The applied load value provided by Eq. (24) is different for the debonding value measured experimentally $\overline{P}_{\max}$ because Eq. (24) does not take into account the variations of the strain ε_{yy} along the FRP width (width effect).

Since the fracture energy G_F is equal to the area under the $\tau_{zy} - s$ curve (Eq. (17)), it does not depend on the shape of the cohesive material law. Thus, the theoretical load-carrying capacity of the interface depends only on the fracture energy and not on the shape of the $\tau_{zy} - s$ curve [117]. However, several researchers proposed different analytical $\tau_{zy} - s$ functions to describe the stress-transfer mechanism under a pure Mode II loading condition [37, 47, 120]. For example, Wu et al. [115] proposed an analytical approach able to predict the snap-back phenomenon observed by other researchers [11], and Leung and Yang [68] solved the differential equilibrium equation for certain boundary conditions taking into account the adhesive shear strain.

Some researchers used Eq. (24) to compute the value of the fracture energy G_F assuming that the experimental load-carrying capacity is equal to the theoretical load-carrying capacity ($\overline{P}_{\max} = P_{deb}$):

$$G_F = \frac{P_{deb}^{\ 2}}{2 \cdot b_f^{\ 2} \cdot E_f \cdot t_f} \tag{25}$$

The fracture energy obtained by Eq. (25) scales with the width of the FRP composite. Hence, it does not represent a true fracture parameter because it depends on the width of the FRP and not only on the material properties of the interface.

Subramaniam et al. 2007 [99] showed that G_F is a true fracture parameter because it is nominally invariant with the composite width, provided that it is computed from the strain measurements along the FRP central region and not using Eq. (25). According to [99] Eq. (25) cannot be used to compute the fracture energy because it does not take into account the width effect. Some works presented in the literature contradict these results and report that G_F decreases with increasing ratio b_f/b [55]. Czardersky et al. [38] measured the strain close to the edge of the FRP and observed that G_F increases when the FRP width decreases. Some researchers proposed fracture mechanics approaches that provide a formulation of G_F that depends on the FRP width [32]. On the contrary, Dai et al. [41] stated that the fracture energy is a true fracture parameter that has a certain value for particular combination of FRP and concrete. Mazzotti et al. [72] observed that the fracture energy does not scale with the width of the composite due to the small size of the aggregate.

It should be noted that all these works determined the fracture energy G_F using single-lap direct-shear tests. Although the cohesive material law obtained by single-lap direct-shear test was shown to be directly applicable to beam tests [33], the Mode II fracture energy G_F should be higher in the case of the flexural beam test because of the presence of the curvature effect that exerts additional compression on the interface [53].

1.7 Alternative fracture mechanics approaches

The fracture mechanics approach originally proposed by Taljsten 1996 [104] is based on the assumption that the FRP-concrete fracture interface is subjected to a nominally pure Mode II loading configuration. The results obtained through this Mode II fracture mechanics approach, although reasonable when applied to a single-lap direct-shear test, are arguable when used to describe the intermediate crack-induced debonding in a full-scale flexural beam test. The main concern is regarding the presence of a macro-scale Mode I fracture condition (peeling) that should not be confused with the Mode I condition recognized before at the micro-scale level. Few works are available in the literature regarding Mode I and mixed-mode failure of FRP-concrete joints [113, 43,

10]. The Mode I fracture propagation is described through the relationship between the normal stress σ_{zz} (peeling stress) and the crack opening w [71, 29]. Since the fracture energy corresponding to the Mode I fracture condition, i.e. the area under the $\sigma_{zz} - w$ curve, is considerably lower than the Mode II fracture energy [104, 54], even a small peeling stress can significantly reduce the load-carrying capacity of the interface. The presence of a Mode I fracture condition was explained considering the opening of a flexural-shear crack in a full-scale flexural beam test [50]. When the crack propagates the two faces of the crack undergo a relative vertical displacement that induced a mixed-mode failure propagation. Other researchers [53] studied the effect of the shear strength on the debonding failure of full-scale flexural beam tests observing that, for beams sufficiently strong in shear, the relative vertical displacement between the crack faces is limited, and the mixed-mode condition would rapidly merge into a Mode II condition upon debonding propagation. These researchers also proposed an alternative fracture mechanics approach that computes the amount of energy dissipated during debonding by calculating the change in the potential energy of the system. The model proposed included a geometrical-empirical coefficient k_b to take into account the effect of the composite width. Some researchers [118] studied the effect of the Mode I failure condition introducing a small inclination angle (offset) in the applied load. They observed that the effect of the offset is negligible for relatively long bonded length, whereas it significantly reduces the bond strength for relatively short bonded length. Mazzucco et al. [73] described the coupled effect of shear and peeling stress through a numerical simulation of the debonding process with the use of a contact-damage model. Neubauer and Rostasy [75] studied the mixed-mode failure in FRP strengthened RC beams through a truss model with shear crack friction and observed that the bond strength reduction around flexural-shear cracks is limited (within 10% in most cases).

The use of a fictitious zero-thickness interface to describe the FRP-concrete debonding was questioned by some researchers [3, 4]. Observing that debonding usually occurs within the concrete substrate, the Mode I fracture energy of concrete was employed to describe the debonding process. The authors also observed that the estimation of the fracture energy G_F through the fracture mechanics models available in the literature is not reliable.

2 ASSESSMENT OF DESIGN PROCEDURES AND ANALYTICAL MODELS FOR THE EVALUATION OF THE FRP-CONCRETE BOND STRENGTH

2.1 Abstract

Although many experimental and analytical studies fiber reinforced polymers (FRP) applied to reinforced concrete (RC) structures are available in literature, there are issues still under discussion in the research communities. Since the typical failure mode of FRP-concrete joints is reported to be debonding of the composite from the concrete substrate the estimation of the bond strength between FRP and concrete substrate represents a key issue for the proper use of these composites. Despite several analytical models for the evaluation of the FRP-concrete bond strength and some models for the estimation of the effective bond length are available in the literature, they were not assessed by means of an appropriate experimental database. This chapter shows an assessment of twenty analytical models for the evaluation of the FRP-concrete bond strength. The assessment is based on the analysis of a wide experimental database collected from the literature. The results are provided distinguishing between the test set-up adopted and the material used. The accuracy of each model is evaluated by means of a statistical analysis. The influence of the test set-up and material employed on the accuracy of the models was analyzed as well. Furthermore, the accuracy of twelve analytical models for the estimation of the effective bond length was assessed.

2.2 Introduction

Debonding of the FRP composite from the concrete substrate represents the most important issue in designing FRP strengthened RC elements. Debonding failures take place in regions of high interfacial stress caused by material discontinuities or inherent cracks [54] and may occur with no warning at stress levels in the FRP significantly lower than the strengthening composite strength.

Various test set-ups were used to study the FRP-concrete debonding mechanism [118]. Among them, the most used are the single-lap direct-shear test and the double-lap direct-shear test. In addition to direct-shear tests, the small- and full-scale flexural beam test (also referred to as bending test) were employed by some researchers to investigate the debonding process in an attempt to reproduce the actual working conditions of a real beam. Small-scale bending tests are carried out on small-scale specimens where a notch or a hinge is provided in order to initiate debonding at a specific cross-section. In full-

scale flexural beam tests, a RC beam is strengthened by means of FRP composites and tested using a bending configuration (generally a three- or four-point bending configuration). It should be noted that the use of small-scale bending tests for the study of the debonding process is arguable. In fact, in small-scale beams the cross-section curvature, the scale-effect, and the presence of non-negligible friction due to the high height-to-weight ratio may affect the FRP-concrete bond strength. Although the full-scale beam test is recognized to be the optimal test to characterize the FRP-concrete bond [96, 92], the complex load sharing between the externally bonded FRP and the internal steel reinforcement, the curvature that exerts additional compression on the crack interface [53], and the formation of a not-easily predicted crack pattern, represent important issues in evaluating the FRP-concrete bond strength.

Analyzing the behavior of an FRP strengthened RC beam, two main types of debonding failure may be observed: i) the plate end debonding, and ii) intermediate crack-induced debonding. The former generally takes place at the end of the composite strip and can be prevented using anchorages [33, 52], whereas the latter is triggered by flexural or flexural/shear cracks near the region of maximum flexural moment and propagates toward the direction of decreasing moment [27]. The intermediate crack-induced debonding has been widely studied in the last decades and many procedures and analytical models for the evaluation of the FRP-concrete bond strength have been proposed. Some of the proposed analytical models constitute the basis of current codes, recommendations, and guidelines for FRP strengthening design [6, 36, 48].

In this chapter, twenty analytical models for the evaluation of the FRP-concrete bond strength will be presented. In order to assess the accuracy of each analytical model in evaluating the FRP-concrete bond strength, a wide experimental database was collected from the literature and used to compare the experimental results with the analytical provisions. The accuracy of the analytical approaches was assessed through computing the coefficient of variation of each model. The results are provided distinguishing between the test set-up adopted (single-lap or double-lap direct-shear test, flexural beam test) and the composite used (post-impregnated sheets or pre-impregnated laminates). The experimental tests of small-scale notched beams were discarded, and only the results of full-scale strengthened RC beams subjected to bending test were included in the database.

The maximum capacity of an FRP-concrete joint is related to the composite bonded length through the concept of effective bond length l_e [6, 32]. The effective bond length, which is a characteristic value defined by geometric and material properties [54], represents the minimum length needed to fully develop the FRP-concrete bond strength capacity, i.e. is the bonded length beyond which no further increase of bond strength is possible. The definition of the effective bond length is of critical importance in the study of the stress-transfer mechanism in FRP-concrete joints. Several models for the evaluation of l_e were proposed by different authors in the last decades, each considering different parameters and leading to different results. In this chapter, twelve analytical

models for the evaluation of the FRP effective bond length l_e were studied. The experimental database used to assess the analytical bond strength models was also employed to assess the accuracy of the effective bond length analytical models. The assessment was carried out without distinguishing between different test set-ups and composite used due to the reduced number of experimentally measured effective bond length values.

2.3 Current analytical models for predicting FRP-concrete bond strength

The most important analytical models for the evaluation of the FRP-concrete bond strength have been collected. Twenty models, including those adopted by the European [48], American [6] and Italian [36] guidelines, are considered. Each model is hereafter described using the same notation adopted by the authors in the original works. In all models the elastic modulus, thickness and width of the FRP composite are indicated as E_f, t_f, and b_f, respectively. All the analytical models were applied without using partial safety factors, assuming that they provide the mean value of the maximum force which can be carried by the FRP-concrete joint. The mechanical parameters that were not reported in the original works were computed using the data available and applying the design codes or standard associated to each model, i.e. the EN 1992-1-1 2004 [45], and the ACI 318M-05 [5]. Where not specified, all the parameters are expressed in SI units (length in millimeters, force in Newton). For any further details about the analytical formulations the reader can refer to the original works.

2.3.1 fib Bulletin 14-T.G. 9.3 2001 [48]

The formulation proposed by the European *fib* Bulletin 14-2001 [48] is based on the work carried out by Neubauer and Rostasy [76]. According to it, the maximum force $N_{fa,\max}$ which can be anchored by the FRP can be obtained as:

$$N_{fa,\max} = \alpha\, c_1 k_c k_b b \sqrt{E_f t_f f_{ctm}} \qquad \text{[N]} \tag{26}$$

where α is a reduction factor taking into account the influence of inclined cracks; f_{ctm} is the mean value of the concrete tensile strength; c_1 may be obtained through calibration with test results and, in case of CFRP, is equal to 0.64; k_c is a factor accounting for the state of compaction of the concrete, and k_b is a geometrical coefficient computed as:

$$k_b = 1.06 \sqrt{\frac{2 - b_f/b}{1 + b_f/400}} \geq 1 \qquad \text{[-]} \tag{27}$$

where b and b_f are the cross-section width of the strengthened element and of the FRP composite, respectively. If the bonded length l_b is less than the effective bond length $l_{b,\max}$, the maximum force $N_{fa,\max}$ is reduced according to Eq. (28):

$$N_{fa} = N_{fa,\max} \frac{l_b}{l_{b,\max}} \left(2 - \frac{l_b}{l_{b,\max}} \right) \quad \text{[N]} \tag{28}$$

2.3.2 CNR-DT 200/2004 [36]

The Italian recommendations CNR-DT 200/2004 [36] propose a formulation similar to that of the *fib* Bulletin 14-2001 [48]. Using a fracture mechanics approach it quantifies the maximum stress in the FRP composite, f_{fdd}, as a function of the fracture energy, Γ_{Fk}, of the FRP-concrete interface. The maximum stress which can be carried by the FRP-concrete joint is computed as:

$$f_{fdd} = \frac{k_{cr}}{\gamma_{f,d}\sqrt{\gamma_c}} \sqrt{\frac{2E_f \Gamma_{Fk}}{t_f}} \quad \text{[MPa]} \tag{29}$$

where $\gamma_{f,d}$ and γ_c are the composite and concrete safety factors, respectively.

If the bonded length l_b is less than the effective bond length l_e, the maximum stress is reduced according to Eq. (30):

$$f_{fdd,rid} = f_{fdd} \frac{l_b}{l_e} \left(2 - \frac{l_b}{l_e} \right) \quad \text{[MPa]} \tag{30}$$

The maximum force which can be anchored by the FRP is finally calculated multiplying the cross-sectional area of the composite by the maximum stress obtained with Eq. (29) and (30). The reduction factor k_{cr} distinguishes between different types of delamination ($k_{cr} = 1.0$ in case of plate end delamination, whereas $k_{cr} = 3.0$ in case of intermediate delamination due to flexural cracking).

The specific fracture energy of the FRP-concrete interface is calculated as:

$$\Gamma_{Fk} = 0.03 k_b \sqrt{f_{ck} \cdot f_{ctm}} \quad \text{[N/mm}^2\text{]} \tag{31}$$

where f_{ck} is the characteristic compressive cylinder strength of concrete, and k_b is a geometrical factor equal to:

$$k_b = 1.06 \sqrt{\frac{2 - b_f / b}{1 + b_f / 400}} \geq 1 \quad \text{[-]} \tag{32}$$

2.3.3 CNR-DT 200 R1/2013 [35]

A new version of the Italian guidelines, CNR DT-200 R1/2013 [35] has been recently published. It provides new equations that can improve the model accuracy with respect to the previous version [36]. New equations for computing the fracture energy, which has a different value depending on the material used, the effective bond length, and the FRP-concrete strength are provided. The maximum stress f_{fdd} that can be carried by the composite preventing the plate end debonding failure is calculated as:

$$f_{fdd} = \frac{k_{cr}}{\gamma_{f,d}} \sqrt{\frac{2E_f \Gamma_{Fd}}{t_f}} \qquad \text{[MPa]} \tag{33}$$

$$f_{fdd,rid} = f_{fdd} \frac{l_b}{l_e}\left(2 - \frac{l_b}{l_e}\right) \quad for\ l_b < l_e \qquad \text{[MPa]} \tag{34}$$

The specific fracture energy Γ_{Fd} is computed according to Eq.(35):

$$\Gamma_{Fd} = \frac{k_b \cdot k_G}{FC} \cdot \sqrt{f_{cm} \cdot f_{ctm}} \qquad \text{[N/mm}^2\text{]} \tag{35}$$

$$k_b = \sqrt{\frac{2 - b_f/b}{1 + b_f/b}} \geq 1 \qquad \text{[-]} \tag{36}$$

where $k_G = 0.023$ in case of pre-impregnated laminate, and $k_G = 0.037$ in case of post-impregnated sheet. *FC* is an additional safety factor. In order to avoid the intermediate crack-induced debonding failure the maximum FRP stress must be less or equal to $f_{fdd,2}$:

$$f_{fdd,2} = \frac{k_q}{\gamma_{f,d}} \sqrt{\frac{E_f}{t_f} \cdot \frac{2 \cdot k_b \cdot k_{G,2}}{FC} \cdot \sqrt{f_{cm} \cdot f_{ctm}}} \qquad \text{[MPa]} \tag{37}$$

where $k_{G,2}$ is an empirical coefficient equal to 0.10, and $k_q = 1.25$ in case of distributed load, and $k_q = 1.0$ in all other cases.

2.3.4 ACI 440.2R 2008 [6]

The guidelines of the American Concrete Institute calculate the maximum bond strength, in case of flexural strengthening, multiplying the maximum strain in the FRP composite at the ultimate limit state, named effective strain ε_{fe}, by the elasticity

modulus of the FRP composite E_f, assuming perfectly elastic behavior. The effective strain ε_{fe} in the FRP composite is limited to the strain value at which debonding may occur, ε_{fd}, as defined in Eq. (38) and (39). The effective stress in the FRP reinforcement f_{fe} is then obtained considering the mode of failure for a given neutral axis depth, as shown in Eq. (39) and (40). "If the left term of the inequality (39) controls, concrete crushing controls flexural failure of the section. If the right term of the inequality (39) controls, FRP failure (rupture or debonding) controls flexural failure of the section"[6]. It should be noted that the FRP rupture is not actually possible since the composite ultimate strain ε_{fu} is limited as per Eq. (38).

$$\varepsilon_{fd} = 0.41\sqrt{\frac{f'_c}{nE_f t_f}} \le 0.9\varepsilon_{fu} \qquad [-] \tag{38}$$

$$\varepsilon_{fe} = \varepsilon_{cu}\left(\frac{d_f - c}{c}\right) \le \varepsilon_{fd} \qquad [-] \tag{39}$$

$$f_{fe} = E_f \cdot \varepsilon_{fe} \qquad [\text{MPa}] \tag{40}$$

In this guide, n indicates the number of plies of FRP reinforcement, t_f is the thickness of one ply of FRP reinforcement, f'_c is the specified concrete compressive strength, ε_{cu} is the ultimate axial strain of unconfined concrete, taken as 0.003, and d_f and c are the FRP composite depth and neutral axis depth, respectively. The maximum force which can be anchored by the composite is finally obtained multiplying the area of the composite by the effective stress f_{fe}.

In case of shear or simply axial strengthening the maximum bond strength is calculated multiplying the maximum strain in the FRP reinforcement at the ultimate limit state, ε_{fe}, according to Eq. (41) (valid in case of U-wraps or bonded face plies), by the FRP elastic modulus, assuming perfectly elastic behavior as for flexural strengthening (Eq. (40)). In this case the effective strain is limited by means of an empirical coefficient, k_v as follows:

$$\varepsilon_{fe} = k_v\, \varepsilon_{fu} \le 0.004 \qquad [-] \tag{41}$$

$$k_v = \frac{k_1\, k_2\, l_e}{11900\, \varepsilon_{fu}} \le 0.75 \qquad [-] \tag{42}$$

k_1 and k_2 are modification factors taken equals to 1.0 in case of pure axial tension.

In addition to these models, sixteen other formulations proposed by various authors were considered. The expressions for computing the maximum force, N_f, carried by the FRP-concrete joint are hereafter briefly reported for the sake of completeness. The meaning of the symbols is indicated in the following if not already reported.

2.3.5 Van Gemert [112]

$$N_f = 0.5 \cdot b_f \cdot l_b \cdot f_{ctm} \quad \text{[N]} \tag{43}$$

2.3.6 Tanaka [32]

$$N_f = (6.13 - \ln l_b) \cdot b_f \cdot l_b \quad \text{[N]} \tag{44}$$

2.3.7 Hiroyuki and Wu [63]

$$N_f = b_f \cdot l_b \left(5.88 \cdot l_b^{-0.669}\right) \quad \text{[N]} \tag{45}$$

where the quantity within the brackets represents the average bond strength τ_u expressed in MPa, and l_b within the brackets is expressed in centimeters.

2.3.8 Maeda et al. [32]

$$N_f = 110.2 \cdot 10^{-6} \cdot E_f \cdot t_f \cdot b_f \cdot l_e \quad \text{[N]} \tag{46}$$

2.3.9 Neubauer and Rostàsy [76]

$$N_f = 0.64 \cdot k_p \cdot b_f \cdot \sqrt{f_{ctm} \cdot E_f \cdot t_f} \quad \text{[N]} \qquad \text{if } l_b \geq l_e \tag{47}$$

$$N_f = 0.64 \cdot k_p \cdot b_f \cdot \sqrt{f_{ctm} \cdot E_f \cdot t_f} \cdot \frac{l_b}{l_e} \cdot \left(2 - \frac{l_b}{l_e}\right) \quad \text{[N]} \qquad \text{if } l_b < l_e \tag{48}$$

where k_p is a geometrical factor calculated according to Eq. (49):

$$k_p = \sqrt{1.125 \frac{2 - b_p / b_c}{1 + b_p / 400}} \quad \text{[-]} \tag{49}$$

2.3.10 Khalifa et al. [66]

$$N_f = 110.2 \cdot 10^{-6} \cdot \left(\frac{f_{ck}}{42} \right)^{2/3} E_f \cdot t_f \cdot b_f \cdot l_e \qquad \text{[N]} \tag{50}$$

2.3.11 Adhikary and Mutsuyoshi [7]

$$N_f = b_f \cdot l_b \cdot \left(0.25 \cdot f_{ck}^{2/3} \right) \qquad \text{[N]} \tag{51}$$

2.3.12 Chen and Teng [32]

$$N_f = 0.315 \cdot \beta_p \cdot \beta_L \cdot \sqrt{f_{ck}} \cdot b_f \cdot l_e \qquad \text{[N]} \tag{52}$$

$$\beta_p = \sqrt{\frac{2 - b_f / b}{1 + b_f / b}} \qquad \text{[-]} \tag{53}$$

$$\beta_L = \begin{cases} 1 & if\ l_b \geq l_e \\ \sin \dfrac{\pi l_b}{2 l_e} & if\ l_b < l_e \end{cases} \qquad \text{[-]} \tag{54}$$

2.3.13 De Lorenzis et al. [44]

$$N_f = b_f \cdot \sqrt{2 \cdot E_f \cdot t_f \cdot G_f} \qquad \text{[N]} \tag{55}$$

where G_f is the fracture energy per unit area of the joint, assumed equal to 1.43 Nmm/mm^2. It should be noted that Eq. (55) was originally proposed by Taljsten [104].

2.3.14 Yang et al. [70]

$$N_f = \left(0.5 + 0.08 \cdot \sqrt{\frac{E_f \cdot t_f}{1000}} \right) \cdot b_f \cdot l_e \cdot 0.5 \cdot f_{ctm} \qquad \text{[N]} \tag{56}$$

2.3.15 Izumo [64]

$$N_f = \left(3.8 \cdot f_{ck}^{2/3} + 15.2\right) \cdot l_b \cdot b_f \cdot E_f \cdot t_f \cdot 10^{-3} \qquad \text{[N]} \tag{57}$$

2.3.16 Iso [64]

$$N_f = b_f \cdot l_e \cdot 0.93 \cdot f_{ck}^{0.44} \qquad \text{[N]} \tag{58}$$

2.3.17 Sato [64]

$$N_f = \left(b_f + 7.4\right) \cdot l_e \cdot 2.68 \cdot f_{ck}^{0.2} \cdot E_f \cdot t_f \cdot 10^{-5} \qquad \text{[N]} \tag{59}$$

2.3.18 Dai et al. [41]

$$N_f = \left(b_f + 7.4\right) \cdot \sqrt{2 \cdot E_f \cdot t_f \cdot G_f} \qquad \text{[N]} \tag{60}$$

$$G_f = 0.514 f_c^{0.236} \qquad \text{[N/mm]} \tag{61}$$

where f_c is the concrete compressive strength.

2.3.19 Lu et al. [70]

$$N_f = \beta_l \cdot b_f \cdot \sqrt{2 \cdot E_f \cdot t_f \cdot G_f} \qquad \text{[N]} \tag{62}$$

$$\beta_l = \sin\left(\frac{\pi \cdot l_b}{2 \cdot l_e}\right) \qquad \text{[-]} \tag{63}$$

$$G_f = 0.308 \cdot \beta_w^2 \sqrt{f_t} \qquad \text{[N/mm]} \tag{64}$$

$$\beta_w = \sqrt{\frac{2.25 - b_f / b}{1.25 + b_f / b}} \qquad \text{[-]} \tag{65}$$

where f_t is the concrete tensile strength.

2.3.20 Camli and Binici [22]

$$N_f = \sqrt{\tau_f \cdot \delta_u} \cdot \sqrt{E_f \cdot t_f} \cdot b_f \cdot \tanh\left(\frac{\theta \cdot l_b}{l_e}\right) \quad \text{[N]} \tag{66}$$

$$\theta = \sqrt{\frac{\tau_f}{\delta_u \sqrt{f_c}}} \quad \text{[rad]} \tag{67}$$

$$\tau_f = 3.5 f_c^{0.19} \quad \text{[MPa]} \tag{68}$$

$$\delta_u = f_c^{\alpha}\left(\frac{l_b}{l_e}\right)^{\beta}\left(\frac{b_f}{b}\right)^{\gamma} \quad \text{[mm]} \tag{69}$$

where α, β, and γ are coefficients determined through non-linear regression analysis and set equal to -0.40, 0.80, and 0.40, respectively.

2.4 Experimental database

A wide experimental database was collected from the literature and used to assess the FRP-concrete bond strength analytical models reported above. The database is comprised of 404 specimens, 231 of which were tested using the single-lap direct-shear test set-up [18, 23, 24, 30, 32, 74, 98, 99, 107, 118], including both pre-impregnated laminates (25 specimens), and post-impregnated sheets (206 specimens); 60 specimens were strengthened with post-impregnated sheet composites and tested using the double-lap direct-shear test set-up [32, 70, 89]; 113 full-scale beams were tested in bending [9, 46, 50, 77, 91, 97, 105], including both pre-impregnated laminates (74 specimens) and post-impregnated sheets (39 specimens). The detailed geometric properties and material characteristics of the specimens included in the database are reported in Appendix A.

2.5 Statistical procedure

The experimental results included within the database were compared with the analytical provisions obtained by each FRP-concrete bond strength analytical model. The values are provided in terms of the maximum experimentally measured force $P_{\exp}$, and theoretical force P_{th}, that can be carried by the FRP-concrete joint. Experimental vs. theoretical bond strength diagrams were built [70,97]. The accuracy of the various models was assessed through computing the coefficient of variation CoV, defined by Eq. (73), with respect to the optimum average value $Avg_{ref} = 1.0$, which indicates perfect matching of experimental and analytical bond strength. In addition, the average

Avg , and the standard deviation StD were calculated in Eq. (71) and Eq. (72), respectively:

$$x_i = P_{\exp,i} / P_{th,i} \tag{70}$$

$$Avg = \frac{\sum_{i=1}^{n} x_i}{n} \tag{71}$$

$$StD = \sqrt{\frac{\sum_{i=1}^{n} \left(x_i - Avg\right)^2}{n}} \tag{72}$$

$$CoV = \sqrt{\frac{\sum_{i=1}^{n} \left(x_i - Avg_{ref}\right)^2}{n}} \tag{73}$$

Figure 7 and Figure 8 report the diagrams obtained in case of the *fib* Bulletin 14-2001 [48], CNR-DT 200/2004 [36], and ACI 440.2R 2008 [6], and CNR-DT 200 R1/2013 [35] models. The left-hand graphs reported in Figure 7 and Figure 8 zoom the initial part of the corresponding right-hand graphs. The values above the line $P_{\exp} / P_{th} = 1$ are conservative since the experimental bond strength is greater than the corresponding analytical prediction, whereas values below the line $P_{\exp} / P_{th} = 1$ are non-conservative.

The statistical procedure was carried out distinguishing between different test set-ups (Figure 7), i.e. single-lap direct-shear test (*Single*), double-lap direct-shear test (*Double*), and full-scale bending test (*Bending*). In addition, FRP-concrete joints comprised of post-impregnated sheets (*Sheet*) and pre-impregnated laminates (*Laminate*) were analyzed separately to assess whether or not the composite used has an influence on the bond strength value (Figure 8).

Table 1 summarizes the results obtained for each model, listing the coefficient of variation CoV and the corresponding average value of the ratio between the experimental and theoretical value, Avg .

Table 1. Results of the statistical analysis to assess the FRP-concrete bond strength analytical models.

Analytical model	*Single*		*Double*		*Bending*		*Sheet*		*Laminate*		*Sheet + Laminate*	
	Avg	*CoV*	*Avg*	*CoV*	*Avg*	*CoV*	*Avg*	*CoV*	*Avg*	*CoV*	*Avg*	*CoV*
Van Gemert [112]	1.51	0.84	0.94	0.54	0.79	3.07	1.21	0.66	0.76	1.02	1.10	0.76
Tanaka [32]	1.75	1.20	1.40	0.70	-	-	1.88	1.00	1.96	2.54	1.77	1.21

Analytical model	*Single*		*Double*		*Bending*		*Sheet*		*Laminate*		*Sheet + Laminate*	
	Avg	*CoV*	*Avg*	*CoV*	*Avg*	*CoV*	*Avg*	*CoV*	*Avg*	*CoV*	*Avg*	*CoV*
Hiroyuki and Wu [63]	1.91	1.15	1.82	1.25	1.90	1.38	1.88	1.37	1.96	1.40	1.90	1.38
Maeda et al. [32]	0.97	0.24	1.05	0.32	1.34	0.91	1.09	0.56	1.07	0.44	1.09	0.53
Neubauer and Rostasy [76]	0.87	1.38	0.99	0.22	1.31	0.91	1.02	0.51	0.99	0.53	1.02	0.51
Khalifa et al. [66]	1.24	0.41	1.05	0.38	1.25	0.88	1.28	0.62	1.01	0.42	1.22	0.58
fib Bulletin 14-T.G. 9.3 2001	0.84	0.23	0.85	0.26	1.10	0.72	0.93	0.44	0.87	0.41	0.91	0.43
Adhikary and Mutsuyoshi [7]	0.90	0.41	0.55	0.55	0.20	0.81	0.72	0.47	0.45	0.81	0.65	0.57
Chen and Teng [32]	1.47	1.38	1.66	0.75	2.21	1.88	1.71	1.11	1.72	1.13	1.71	1.12
De Lorenzis et al. [44]	0.67	0.36	0.72	0.34	0.88	0.60	0.75	0.45	0.70	0.42	0.74	0.44
Izumo [64]	0.85	0.39	0.69	0.62	0.10	0.98	0.74	0.52	0.07	0.93	0.62	0.61
Iso [64]	1.06	0.26	0.96	0.31	1.06	0.77	1.10	0.49	0.87	0.41	1.04	0.47
Sato [64]	0.73	0.36	0.85	0.53	0.50	0.81	0.76	0.47	0.44	0.73	0.68	0.54
Yang et al. [70]	1.14	0.30	1.04	0.35	1.34	0.91	1.22	0.58	1.09	0.43	1.18	0.55
CNR-DT 200/2004 [36]	1.42	0.52	1.34	0.52	0.94	0.33	1.34	0.50	1.03	0.39	1.26	0.47
Dai et al. [41]	0.61	0.41	0.67	0.38	0.86	0.59	0.70	0.47	0.66	0.45	0.69	0.46
Lu et al. [70]	1.00	0.18	1.17	0.32	1.55	1.14	1.18	0.64	1.18	0.62	1.18	0.63
Camli and Binici [22]	1.01	0.31	0.84	0.37	0.60	0.56	0.93	0.35	0.68	0.52	0.87	0.40
ACI 440.2R 2008 [6]	1.45	0.59	1.78	0.94	2.23	1.50	1.54	0.72	2.12	1.40	1.68	0.93
CNR-DT 200 R1/2013[35]	1.30	0.44	1.22	0.42	1.26	0.77	1.23	0.36	1.41	0.91	1.28	0.55

2.6 Assessment of the FRP-concrete bond strength analytical models

Analyzing the results obtained for the most important guidelines [6, 36, 48], it can be noted that the predictions are sometimes non-conservative (Figure 7). However, the American guidelines [6] provide more conservative predictions in terms of maximum FRP-concrete bond strength with respect to the other models, though its accuracy is rather poor. This can be due to the fact that the American formulations are based on the regression of too few experimental data.

The statistical analysis applied to the different test set-ups shows that some models provide more accurate results (i.e. *CoV* close to 0.0) in case of single-lap direct-shear test, whereas other models provide more accurate results in case of double-lap direct-

shear tests (Table 1). The best result in terms of coefficient of variation was obtained by the model of Lu et al. [70] in case of single-lap direct-shear test ($CoV = 0.18$), whereas the model of Neubauer and Rostàsy [76] obtained the best result in case of double-lap direct-shear test ($CoV = 0.22$). It should be noted that, except for the previous version of the Italian guidelines [36] ($CoV = 0.33$), the analytical provisions are particularly inaccurate in the case of full-scale bending tests rather than direct-shear tests. This can be justified by the fact that all analytical models were formulated and calibrated mostly using single- and double-lap direct-shear tests, because of their lower cost with respect to full-scale bending tests. Furthermore, in case of full-scale bending tests, the maximum load that can be carried by the FRP-concrete interface is not directly measured, but it is calculated according to the flexural moment and the corresponding measured beam failure load ($2P$ in Figure 2c). Therefore, the hypotheses on which the above calculations are based, mainly related to the assumption that the cross-sections of the beam remain plane, may affect the estimation of the FRP-concrete bond strength. The new version of the Italian guidelines, CNR-DT 200 R1/2013 [35], provides better results with respect to the previous version [36] both in case of single- ($CoV = 0.44$), and double-lap ($CoV = 0.42$) direct-shear tests. When applied to full-scale bending tests, the CNR-DT 200 R1/2013 [35] seems to be particularly inaccurate ($CoV = 0.77$), especially if compared with the result obtained with the previous version [36] ($CoV = 0.33$). The same issue arises when the analytical model proposed by the CNR-DT 200 R1/2013 [35] is applied to the tests carried out using pre-impregnated laminate ($CoV = 0.91$, 2.3 times higher respect to the previous version). This inaccuracy affects the overall results of the model ($CoV = 0.55$).

A clear influence of the material employed (i.e. post-impregnated sheet and pre-impregnated laminate composites) was not observed. However, it should be pointed out that pre-impregnated laminates are usually employed in case of full-scale bending test, whereas post-impregnated sheets are more diffused in case of single- and double-lap direct-shear test. Furthermore, double-lap direct-shear tests carried out using FRP laminates were not available at the time in which the database was collected. For these reasons, for a given test set-up, the influence of the material used was not investigated.

The new version of the Italian guidelines [35] is particularly inaccurate in case of full-scale bending test and when applied to pre-impregnate laminate. Unfortunately, since the 75% of the full-scale bending test results included within the database are carried out using pre-impregnated laminates, it was not possible to distinguish the effects of the test set-up and of the material used on the model accuracy.

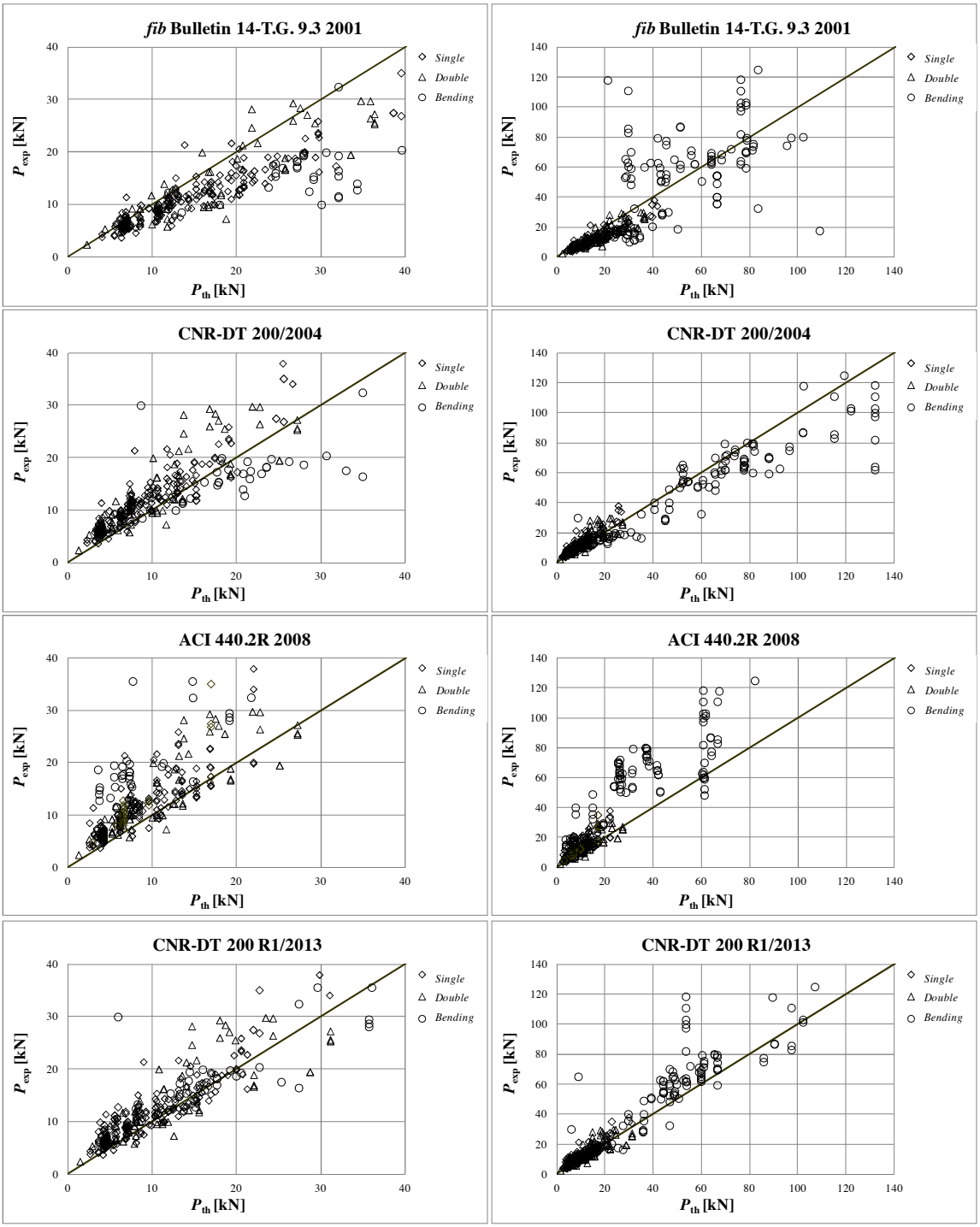

Figure 7. Comparison between experimental and analytical values of the FRP-concrete bond strength for different experimental set-ups (*Single*, *Double*, *Bending*) in case of the European [48], Italian [36, 35], and American [6] guidelines.

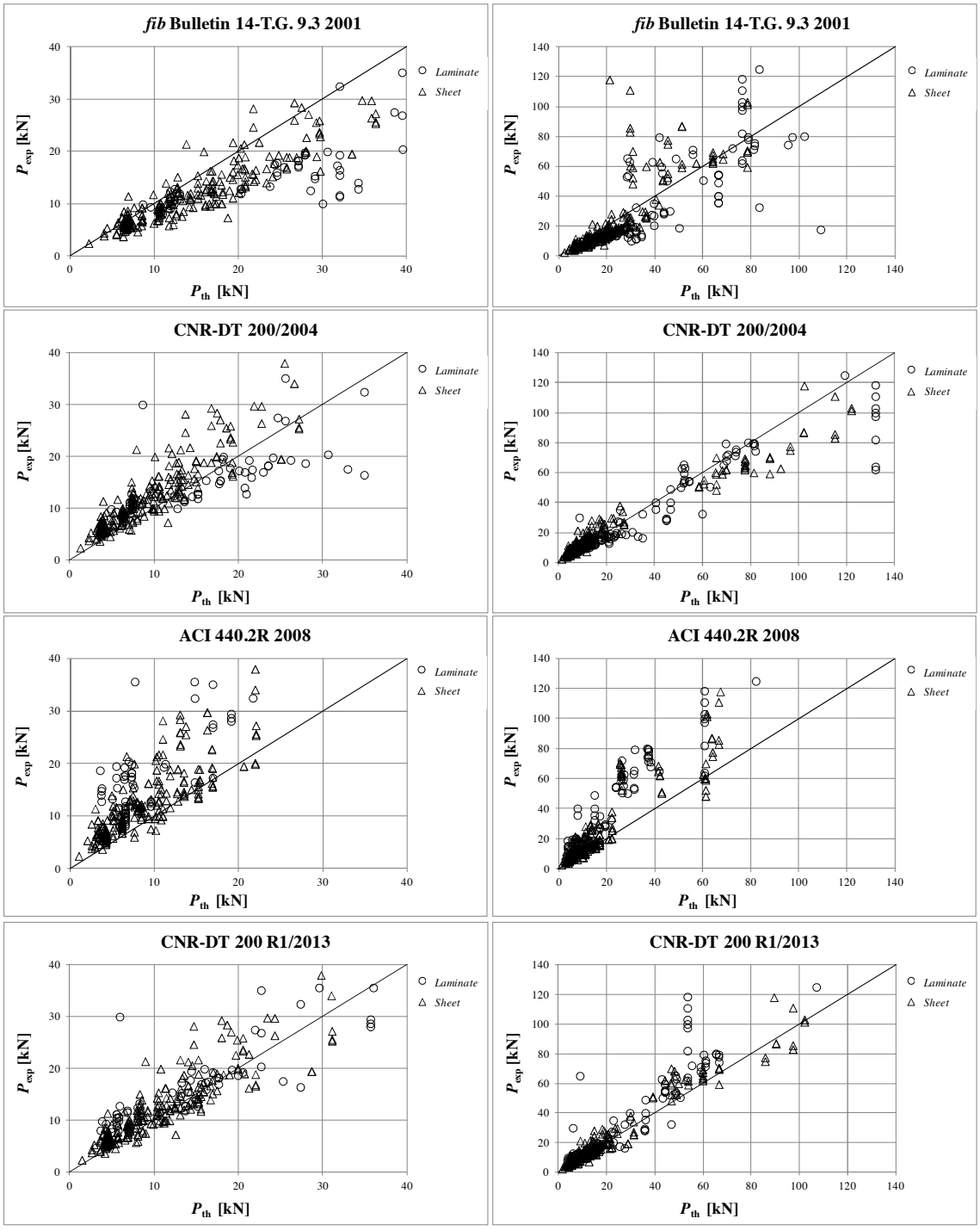

Figure 8. Comparison between experimental and analytical values of the FRP-concrete bond strength for different materials used (*Laminate*, *Sheet*) in case of the European [48], Italian [36, 35], and American [6] guidelines.

Considering the overall results without distinguishing between test set-ups and material used (*Sheet* + *Laminate* in Table 1), the statistical analysis shows that the analytical formulation proposed by Camli and Binici [22] for the evaluation of the FRP-concrete bond strength is the most accurate, having a coefficient of variation $CoV = 0.40$.

2.7 Analytical models for the evaluation of the effective bond length

The theoretical effective bond length, $l_{e,th}$, obtained through twelve different analytical models, was compared with the corresponding effective bond length experimentally measured value, $l_{e,exp}$. The analytical models employed to evaluate the effective bond length are hereafter briefly summarized, chronologically ordered, for the sake of clarity. Further details are provided in the original works.

2.7.1 fib Bulletin 14-T.G. 9.3 2001 [48] - CNR-DT 200/2004 [36] - Neubauer and Rostàsy [76]

The European [48], Italian [36], and Neubauer and Rostàsy [76] models propose the same formulation to compute the effective bond length for FRP strengthening:

$$l_e = \sqrt{\frac{E_f \, t_f}{2 \, f_{ctm}}} \qquad \text{[mm]} \tag{74}$$

2.7.2 ACI 440.2R 2008 [6]

The ACI 440.2R 2008 [6] defines the active bond length l_e as "the length over which the majority of the bond stress is maintained" [6]. The active bond length can be computed using Eq. (75):

$$l_e = \frac{23300}{(n_f t_f E_f)^{0.58}} \qquad \text{[mm]} \tag{75}$$

where n_f is the modular ratio of elasticity between FRP and concrete equal to E_f / E_c. It should be pointed out that in case of pure axial strengthening a bonded length equal to $2\,l_e$ is suggested in order to obtain the strain levels provided by Eq. (41).

2.7.3 CNR-DT 200 R1/2013 [35]

The CNR-DT 200 R1/2013 [35] computes the effective bond length, named optimum bond length, according to E q. (76) and (77).

$$l_e = \min\left\{ \frac{1}{\gamma_{Rd} \cdot f_{bd}} \sqrt{\frac{\pi^2 \cdot E_f \cdot t_f \cdot \Gamma_{Fd}}{2}}, 200 \right\} \qquad \text{[mm]} \tag{76}$$

$$f_{bd} = \frac{2 \cdot \Gamma_{Fd}}{s_u} \qquad [\text{N/mm}^2] \tag{77}$$

where $s_u = 0.25$ is the ultimate slip between the FRP and the concrete support, and $\gamma_{Rd} = 1.25$ is a safety modification factor.

2.7.4 Maeda et al. [32] - Khalifa et al. [66]

Khalifa et al. [66] adopted the same model proposed by Maeda et al. [32]:

$$l_e = e^{6.13 - 0.580 \ln E_f t_f} \qquad [\text{mm}] \tag{78}$$

2.7.5 Chen and Teng [32] - Camli and Binici [22]

Camli and Binici [22] adopted the same model originally proposed by Chen and Teng [32]. According to the model, the effective bond length increases with the FRP geometric and mechanical properties, whereas it decreases with the specified concrete compressive strength f'_c.

$$l_e = \sqrt{\frac{E_f t_f}{\sqrt{f'_c}}} \qquad [\text{mm}] \tag{79}$$

It should be noted that the effective bond length proposed in Eq. (79) is also reported in the ACI 440.2R 2008 [6] as the development length l_{db}.

2.7.6 Iso [64]

$$l_e = 1.89 \left(E_f t_f \right)^{0.4} \qquad [\text{mm}] \tag{80}$$

2.7.7 Sato [64]

$$l_e = 0.125 \left(E_f t_f \right)^{0.57} \qquad [\text{mm}] \tag{81}$$

2.7.8 Lu et al. [70]

$$l_e = a + \frac{1}{2\lambda_1} \ln \frac{\lambda_1 + \lambda_2 \tan\left(\lambda_2 a\right)}{\lambda_1 - \lambda_2 \tan\left(\lambda_2 a\right)} \qquad [\text{mm}] \tag{82}$$

$$\lambda_1 = \sqrt{\frac{\tau_{max}}{s_0 E_f t_f}} \qquad \text{[rad/mm]} \tag{83}$$

$$\lambda_2 = \sqrt{\frac{\tau_{max}}{(s_f - s_0) E_f t_f}} \qquad \text{[rad/mm]} \tag{84}$$

$$a = \frac{1}{\lambda_2} \arcsin\left[0.99\sqrt{\frac{s_f - s_0}{s_f}}\right] \qquad \text{[mm]} \tag{85}$$

τ_{max} is the maximum local bond stress defined as:

$$\tau_{max} = \alpha_1 \beta_w f_t \qquad \text{[MPa]} \tag{86}$$

where $\alpha_1 = 1.5$, and s_0 is the corresponding local slip calculated as:

$$s_0 = 0.0195 \cdot \beta_w f_t \qquad \text{[mm]} \tag{87}$$

β_w is the width ratio factor computed according to Eq. (65).

2.7.9 Camli and Binici [22]

$$l_e = \sqrt{\frac{E_f t_f}{\sqrt{f_c}}} \qquad \text{[mm]} \tag{88}$$

2.8 Assessment of the FRP-concrete effective bond length analytical models

Since there are few works in which the effective bond length was experimentally measured due to the practical difficulty of the procedure, the database was comprised of 48 specimens taken from [18, 89, 98, 99, 23, 24, 77]. The same statistical procedure adopted to assess the FRP-concrete bond strength models was carried out to assess the accuracy of the analytical models for the evaluation of the effective bond length.

Table 2 summarizes the results obtained for each model (models proposing the same analytical formulation were gathered together). The same statistical procedure carried out in case of FRP-concrete bond strength models were applied. The value of the coefficient of variation, CoV_e, and the corresponding average value of the ratio between the experimental and theoretical effective bond length, Avg_e, are reported. The coefficient of variation CoV_e, expresses the percentage distance between the ratio $l_{e,\exp}/l_{e,th}$ and the reference average value $Avg_{e,ref} = 1.0$, which indicates perfect matching of experimental and analytical effective bond strength. In addition, the standard deviation StD_e, and the percentage of the overestimated (not safe) effective

bond length values are reported in Table 2 for each model. The influence of the test set-up and material used were not investigated due to the small amount of available experimental data.

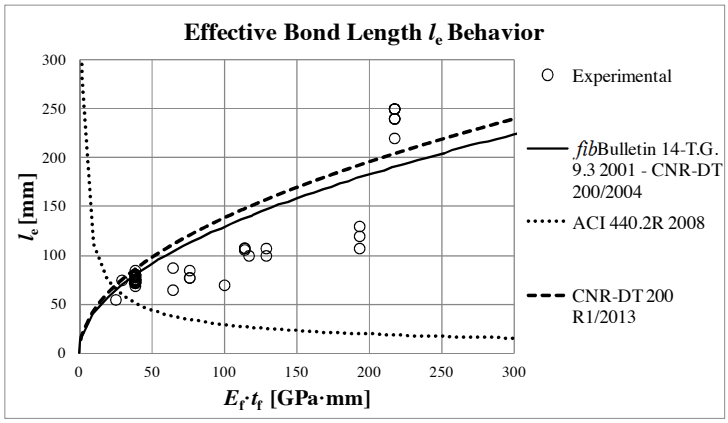

Figure 9. Comparison between experimental results and analytical formulation of the effective bond length as the FRP stiffness increases in case of the European [48], Italian [36, 35], and American [6] guidelines.

The trend of the effective bond length as the FRP stiffness ($E_f t_f$) increases was studied and reported in Figure 9 in case of the European [48], Italian [36, 35], and American [6] guidelines. A constant value $f_{ctm} = 3\,\text{MPa}$ was considered to study the trend of the analytical formulation provided by the Italian guidelines [36, 35] as the FRP stiffness increases. Observing the effective bond length vs. FRP stiffness ($E_f t_f$) diagrams (Figure 9), it can be seen that the predictions are generally good for small values of the FRP stiffness, whereas they become more scattered for higher values. The most accurate result ($CoV_e = 0.15$) was obtained by the new version of the Italian guidelines CNR-DT 200 R1/2013 [35], which improves the model originally proposed by Neubauer and Rostasy 1997 [76] and adopted by the European guidelines [48]. The model adopted by ACI 440.2R 2008 [6] shows an opposite trend with respect to the other main formulations (Figure 10). This can be due to the fact that the American model is based on the regression of few experimental results, without taking into account the cohesive nature of the concrete substrate. The new version of the Italian guidelines [35] shows a similar trend with respect to the previous version [36] (Figure 10) but predicts slightly higher effective bond length for the same FRP stiffness value.

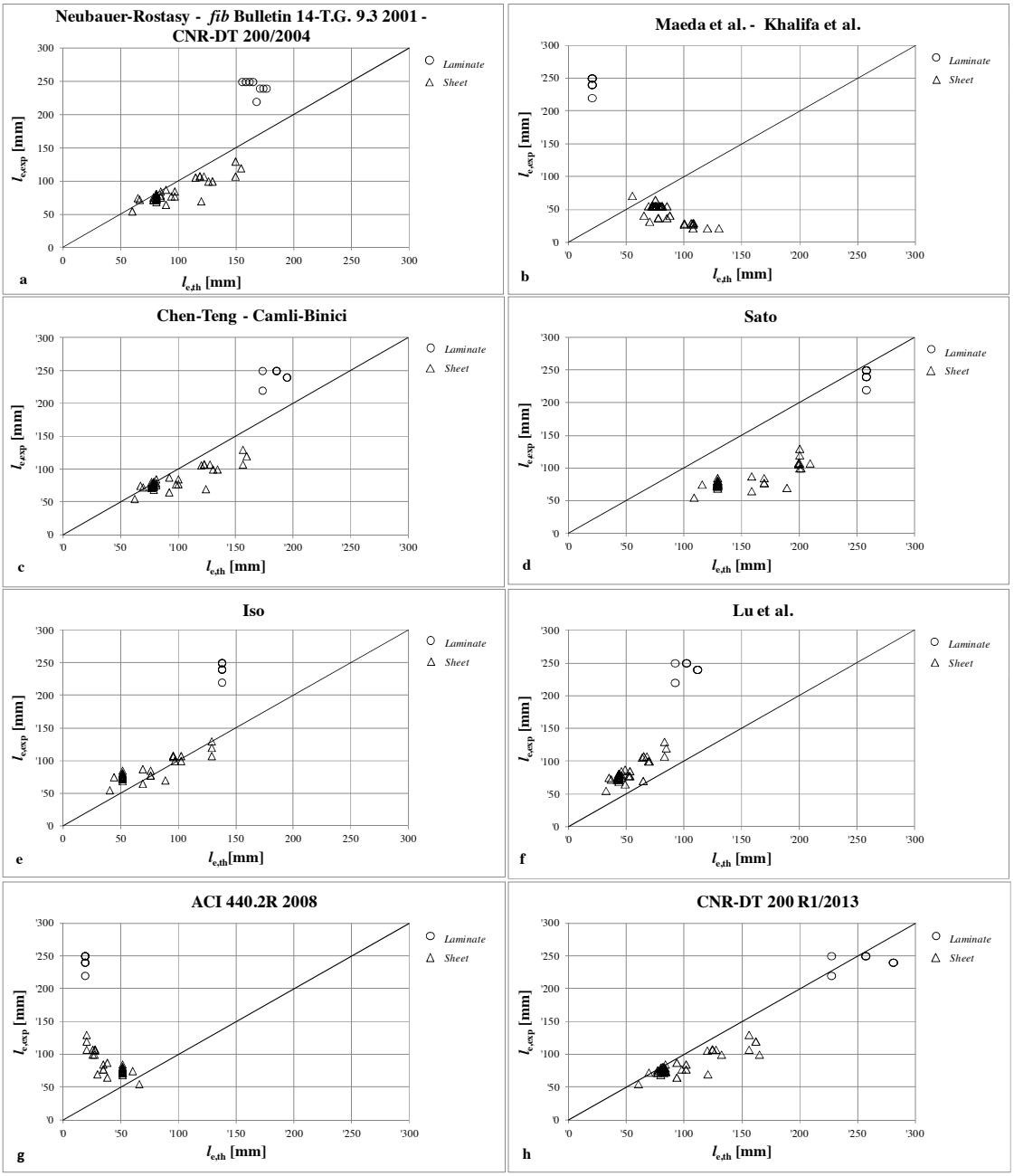

Figure 10. Comparison between experimental and analytical effective bond length values for different material used (*Laminate*, *Sheet*).

Table 2. Results of the statistical analysis to assess the FRP effective bond length analytical models.

Analytical model	CoV_e	StD_e	Avg_e	Overestimated [%]
CNR-DT 200/2004 [36]				
fib Bulletin 14-T.G. 9.3 2001 [48]	0.17	0.17	0.97	73
Neubauer and Rostasy [76]				
Chen and Teng [32]	0.19	0.19	0.98	67
Camli and Binici [22]				
Sato [64]	0.41	0.16	0.62	100
Iso [64]	0.48	0.28	1.39	10
Lu et al. [70]	0.85	0.32	1.79	0
Maeda et al. [32]	4.74	3.90	3.75	2
Khalifa et al. [66]				
ACI 440.2R 2008 [6]	5.18	4.22	4.06	2
CNR-DT 200 R1/2013 [35]	0.15	0.11	0.89	90

2.9 Conclusions

In this chapter a wide experimental database was used to assess the accuracy of twenty analytical models in predicting the FRP-concrete bond strength and twelve analytical models in predicting the FRP effective bond length. In addition, the influence of the test set-up (single-lap direct-shear test, double-lap direct-shear test, and full-scale bending test) and material used (pre-impregnated laminate and post-impregnated sheet) on the FRP-concrete bond strength was analyzed. The results obtained show a clear influence of the test set-up on the accuracy of the analytical models. The majority of the models reported the best accuracy when applied to direct-shear tests and especially when applied to double-lap direct-shear tests. The analytical models considered, except the Italian CNR-DT 200/2004, do not provide a good estimation of the FRP-concrete bond strength when applied to full-scale bending test. The relationship between the debonding mechanism in direct-shear tests and full-scale bending tests is further complicated by the fact that several direct-shear test set-ups are available, and a standardized test is not available.

The analytical models for the estimation of the FRP-concrete effective bond length, except those proposed by Lu et al. [70] and ACI [6], provide good estimation of the experimental results. The model included in the new version of the Italian CNR-DT 200 R1/2013 provides the best results, having a coefficient of variation of 0.15.

3 BOND BEHAVIOR OF PBO FRCM-CONCRETE JOINTS: A FRACTURE MECHANICS APPROACH

3.1 Abstract

The results of single-lap direct-shear tests, conducted on specimens with fiber reinforced cementitious matrix (FRCM) composite strips bonded to concrete blocks, are presented in this chapter. The FRCM composite was comprised of a polyparaphenylene benzobisoxazole (PBO) fiber net embedded within two layers of polymer-modified cement-based mortar. The effects of different bonded lengths and bonded widths were investigated. Axial strain profiles were recorded by means of strain gauges applied onto the fiber. The fracture mechanics approach employed for FRP-concrete joints was applied to FRCM-concrete joints to investigate the stress-transfer mechanism at the matrix-fiber interface.

3.2 Introduction

Strengthening and rehabilitation of reinforced concrete (RC) structures with externally-bonded composite materials represent a valid alternative to new construction because they allow for an extension of the original service life and therefore prevent demolition of existing structures. In the last two decades fiber reinforced polymer (FRP) composites have been the most common type of composites used for structural applications, and several studies were carried out to investigate their behavior. FRP composites are comprised of high strength fibers applied to the structural elements through thermosetting organic matrices, usually epoxy resins. It has been observed that the use of organic resins, though effective, may represent an issue for the durability of the intervention. Indeed, organic matrices degrade when exposed to UV radiation and loose most of their mechanical properties when subjected to temperatures close (or higher) to their glass transition temperature (typically around 70°C) [8].

Promising newly-developed types of matrix that potentially represent a valid alternative to organic resins are the so-called inorganic matrices. Within the broad category of inorganic matrices, polymer-modified cement-based mortars have raised some interest in recent years. Composite materials that employ modified cement-based mortars are usually referred to as fiber-reinforced cementitious matrix (FRCM) composites. Alternative names have been proposed in the literature [79] that refer to different types of matrix or application. In FRCM composites, fibers are typically bundled, and the

fiber pattern can be modified from unidirectional to bidirectional textile weaves or fabrics in an attempt to improve the bond characteristics. Although several works about FRP strengthening are available in the literature and important guidelines have been published [6, 35, 36, 48], very few studies can be found regarding FRCM composites. The limited available literature reports that FRCM composites can be used effectively for strengthening and rehabilitation of RC structures. FRCM composites were successfully employed for flexural strengthening [79, 40, 58, 102, 106], shear strengthening [19, 20, 80], and for confinement of RC members mostly subjected to compressive load [21, 78, 81, 109]. As in case of FRP-concrete joints, debonding failure is the most important issue concerning FRCM strengthening application. However, the weakness of FRCM-concrete joints appears to be at the matrix-fiber interface [16, 39, 42, 56, 57, 65, 114] rather than within the concrete substrate or at the matrix-concrete interface, as is typically observed with FRP composites [4, 25, 28, 29, 32, 47, 51, 88, 89, 95, 98, 99, 111, 117, 118]. The FRCM debonding is reported to be a progressive process resulting in larger deformations at the matrix-fiber interface. Further, the debonding process is complicated by the *telescopic* behavior observed among the fiber filaments of a fiber bundle where the core filaments have a different mechanism of stress transfer with respect to the outer filaments, mainly due to the different impregnation of the fibers by the matrix [16, 57]. FRCM composites are still in their infancy, and a complete understanding of the interfacial stress-transfer mechanism is not available yet, although researchers have attempted a fracture mechanics approach to describe the behavior of the different filaments within the fiber bundle [16, 39, 57].

In FRP-concrete joints, it is well-understood that interfacial crack propagation typically occurs within a thin layer of the substrate very close to the FRP composite (§27), and therefore the concrete mechanical and fracture properties and the support surface treatment play a fundamental role in the evaluation of the strengthening performance. If the present and future investigations on FRCM-concrete joints confirm that interfacial debonding occurs within the composite, the substrate on which the composite is applied may not play a key role in the design of the strengthening system.

This chapter presents an extensive experimental study on FRCM composites comprised of polyparaphenylene benzobisoxazole (PBO) fiber net embedded within a polymer-modified cementitious matrix. Single-lap direct-shear tests were conducted to investigate the behavior of the composites. The interfacial debonding of the FRCM-concrete systems was investigated within the framework of fracture mechanics. As a first attempt to study the stress-transfer mechanism that characterizes FRCM composites, the macro-scale fracture mechanics approach used for FRP-concrete interfaces is extended to the matrix-fiber interface of FRCM composites.

3.3 Experimental campaign: test set-up and specimen preparation

The bond behavior of FRCM composite applied to a concrete substrate was studied by

means of an extensive experimental campaign conducted on FRCM-concrete joint specimens tested using the single-lap direct-shear test set-up. FRCM composite strips were externally bonded to concrete blocks (prisms). The classical push-pull configuration was adopted where the fibers were pulled while the concrete prism was restrained [25, 98, 99]. Two different concrete prisms were used, both of which had the same cross section (125 mm width × 125 mm depth), but different lengths (L=375 mm or L=510 mm). The faces of the concrete blocks were sandblasted prior to applying the first (internal) layer of matrix. Only three faces of each block were used, corresponding to the three formed faces. The fourth face of the block, which was troweled smooth after casting, was disregarded. The composite material was comprised of bidirectional polyparaphenylene benzobisoxazole (PBO) fiber net and cementitious matrix. The PBO fiber net was made of bidirectional rovings spaced at 10 mm and 20 mm on center in the two directions (Figure 12b and Figure 13a). The total weight of fibers in the net was 88.0 g/m^2, with 70.2 g/m^2 in the longitudinal and 17.8 g/m^2 in the transversal directions, respectively. The nominal width b^* and average thickness t^* of one longitudinal fiber bundle were 5 mm and 0.092 mm, respectively. All transversal bundles were on one side of the longitudinal bundles, and the net was held together with glass fiber filaments. The matrix was applied only in the bonded area to embed the fibers and bond the composite to the concrete substrate (Figure 11). The matrix was applied from the edge of the external longitudinal bundle on one side of the fiber strip to the edge of external longitudinal bundle on the other side of the fiber strip. Therefore, the width of the composite b_1 was equal to the width of the fiber net b_2 (Figure 13a).

Fibers were bare outside the bonded area. A 4 mm layer of matrix (internal layer) was applied using molds to control the composite width and thickness. A single layer of PBO fiber net was applied onto the matrix, and the fibers were pressed delicately onto the matrix to assure proper impregnation. As discussed in §3.5, the longitudinal fiber bundle side of the net was placed against the internal layer of matrix for some specimens, while the transversal fiber bundle side was placed against the internal layer of matrix for others. Fiber net orientation of each specimen was recorded. A second (external) 4 mm layer of matrix was applied over the PBO fiber net. Thickness of the matrix layers was in accordance with the manufacturer's recommendations [93]. The bonded width (b_1) and length (ℓ) of the composite were varied. Two aluminum plates (Figure 11) were attached with a thermosetting epoxy resin to the end of the fiber strip to improve gripping during testing. For composite strips wider than 43 mm, the aluminum plates were also bolted together with four through-bolts at the plate corners to assure a uniform pressure on the gripped fibers and to prevent slippage of the fibers within the plates.

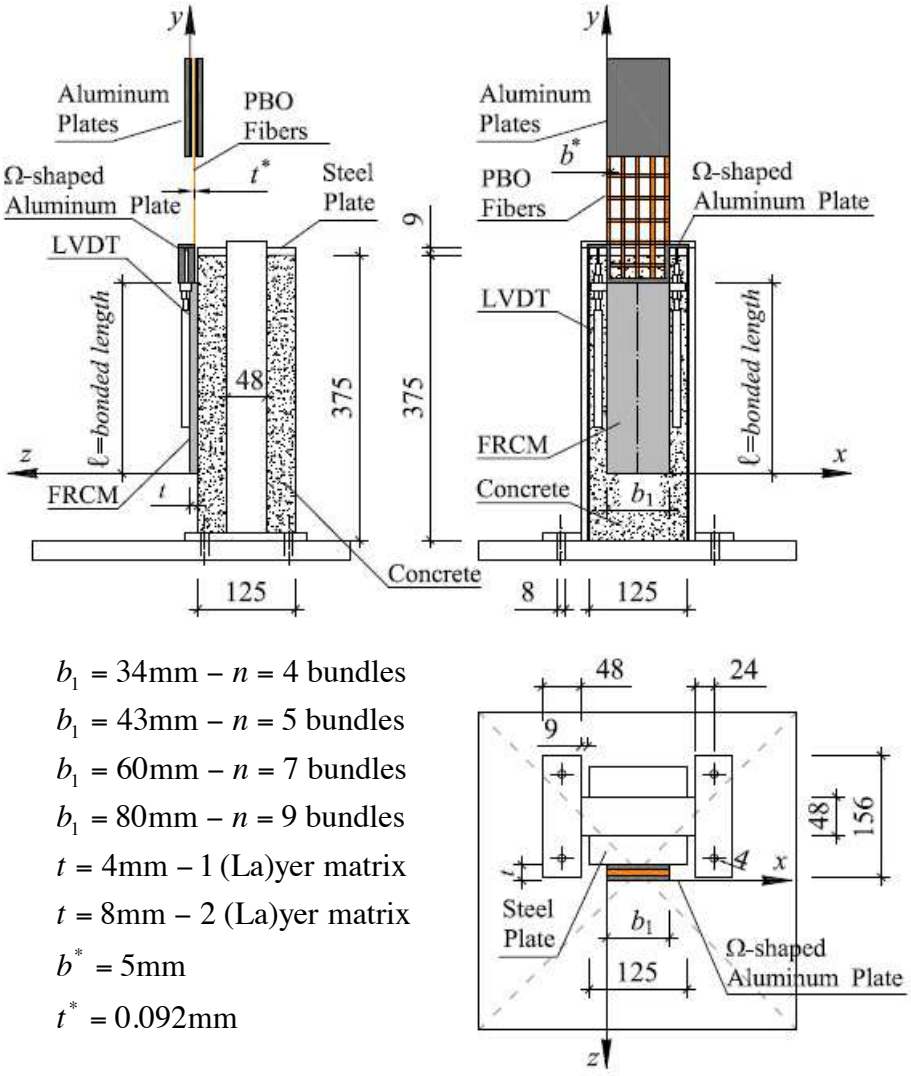

Figure 11. Single-lap direct-shear test set-up.

The concrete prism was restrained against movement by a steel frame bolted to the testing machine base. A steel plate was inserted between the steel frame and the top of the prism to distribute the pressure provided by the frame restraint. The direct-shear tests were conducted under displacement control using a close-loop servo-hydraulic universal testing machine. Two linear variable displacement transducers (LVDTs) were mounted on the concrete surface close to the edge of the composite bonded region. The LVDTs reacted off of a thin aluminum Ω-shaped bent plate that was attached to the PBO transversal fiber bundle surface adjacent to the beginning of the bonded area as shown in Figure 11. The average of the two LVDT measurements, defined as the global slip g, was used to control the test. Based on previous single-lap tests conducted on FRP-concrete joints [25, 98, 99], the global slip was increased at a constant rate of 0.00084 mm/s for all tests. The applied load is termed P (Figure 12a).

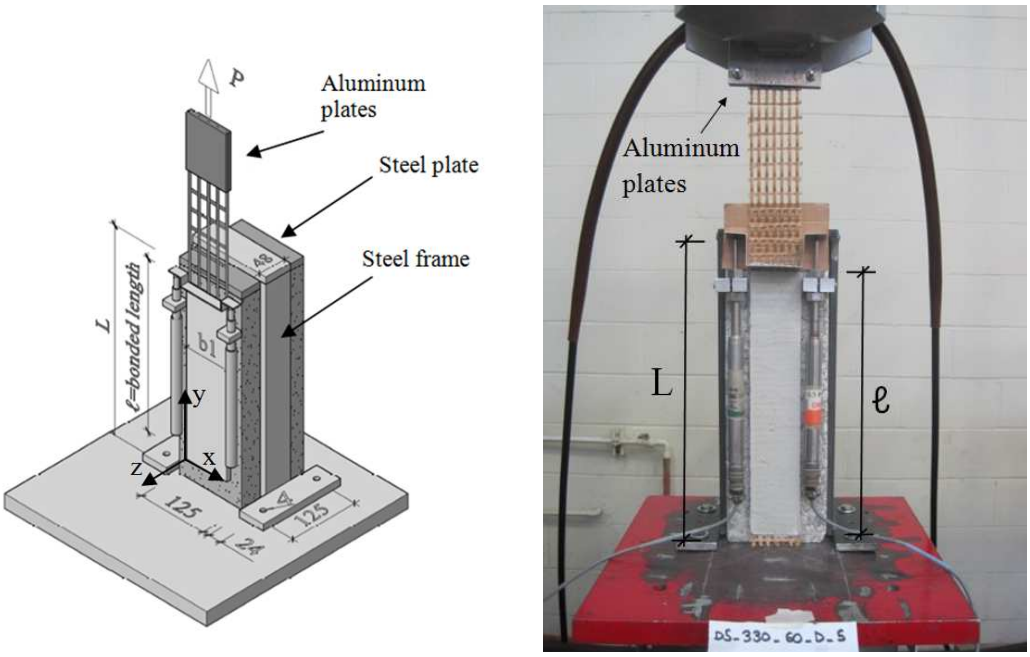

a. b.

Figure 12. a) 3D representation of the single-lap direct-shear test set-up. b) Photo of specimen DS-330_60_D-5

3.4 Material properties

The concrete prisms were constructed with normalweight concrete with portland cement (Type 1) without admixtures. The maximum size of the aggregate was 9.5 mm. Twelve (6+6) 100 mm × 200 mm concrete cylinders were cast from the two batches of concrete used to construct the shorter (L=375 mm) and longer (L=510 mm) concrete blocks. The average compressive strength [13] and splitting tensile strength [14] were 42.5 MPa (CoV=0.013) and 3.4 MPa (CoV=0.113) for the shorter blocks, and 33.5 MPa (CoV=0.085) and 3.0 MPa (CoV=0.042) for the longer blocks. At least two 50 mm × 100 mm cylinders were cast from each batch of matrix used to cast the FRCM composite. The average compressive [13] and splitting tensile [14] strengths of the matrix were 28.4 MPa (CoV=0.092) and 3.5 MPa (CoV=0.231), respectively. The values determined from each batch were consistent, which indicates that the matrix was cast consistently throughout the batches. The compressive strength of the mortar is in good agreement with values provided in [79, 93].

Seventeen tensile tests of the PBO fiber net were carried out to verify the efficacy of the gripping system prior to conducting the shear tests (Figure 13a) and determine the mechanical properties of the fiber net. It should be pointed out that the testing procedure described in [42] was used even though the fibers were not impregnated with epoxy resin or other types of matrix. Two aluminum plates were attached to each end of the fiber net in the same manner as described for the direct shear tests. The tensile tests were performed on fiber nets of various widths (b_2) to determine if the gripping system

or the fiber net itself may have an influence on the mechanical response of specimens with different widths.

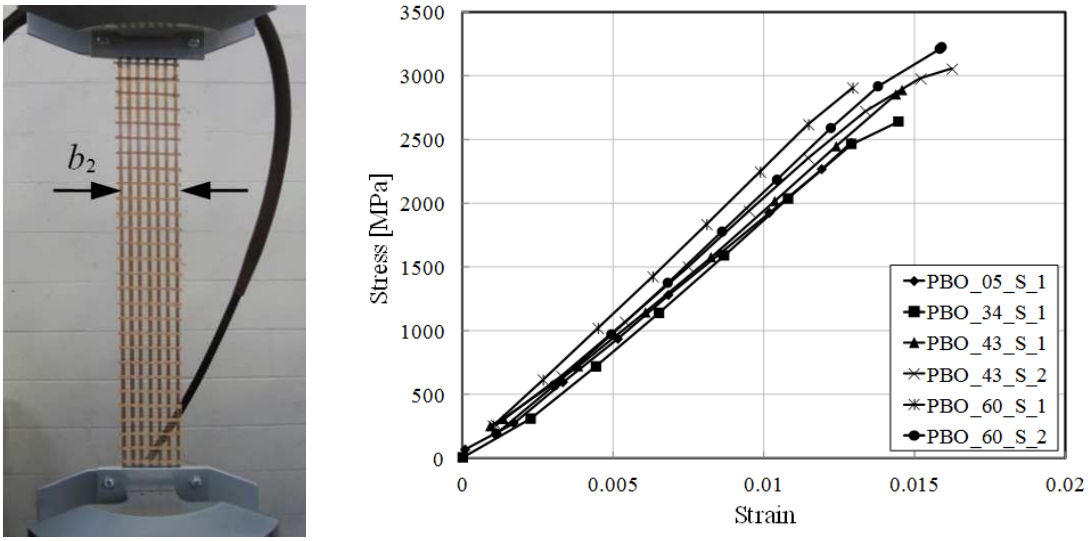

a. b.

Figure 13. a) Photo of tensile test (specimen PBO_60_1). b) Stress-strain relation of PBO fiber net specimens used to determine the ultimate strain and the elastic modulus.

Strain gauges were mounted on the central fiber bundles of eight specimens of various widths. Tensile specimens were named following the notation PBO_X_S_Z, where X=width b_2 of the fiber strip in mm, S (if present) indicates that strain gauges were mounted on the specimen, and Z=specimen number. The nominal stress σ was computed as the applied load P divided by the cross-sectional area of the longitudinal fiber bundles nb^*t^*, where n is the number of longitudinal bundles (Eq. (89)). The ultimate (or peak) stress σ^* is defined by Eq. (90).

$$\sigma = \frac{P}{nb^*t^*} \quad \text{[MPa]} \tag{89}$$

$$\sigma^* = \frac{P^*}{nb^*t^*} \quad \text{[MPa]} \tag{90}$$

The number of longitudinal bundles n across the width of the fiber net, the overall width b_2 of the net, the peak load P^* at failure, the ultimate stress σ^*, and its average σ^*_{avg} for each group with the same width are provided in Table 3.

Table 3. Results of the tensile tests on the fiber net.

Name	b_2 [mm]	P^* [kN]	N [-]	σ^* [MPa]	σ^*_{avg} [MPa] (CoV)
PBO_5_S_1	5	1.39	1	3020	2940 (0.065)
PBO_5_S_2	5	1.41	1	3070	
PBO_5_S_3	5	1.25	1	2720	
PBO_34_1	34	5.52	4	3000	3010 (0.024)
PBO_34_2	34	5.67	4	3080	
PBO_34_3	34	5.41	4	2940	
PBO_34_S_1	34	4.70	4	2550	2550
PBO_43_1	43	6.82	5	2970	2940 (0.010)
PBO_43_2	43	6.72	5	2920	
PBO_43_S_1	43	7.35	5	3200	3140 (0.025)
PBO_43_S_2	43	7.09	5	3080	
PBO_60_1	60	10.64	7	3300	3300
PBO_60_S_1	60	9.85	7	3060	3180 (0.055)
PBO_60_S_2	60	10.65	7	3310	
PBO_80_1	80	13.28	9	3210	3010 (0.087)
PBO_80_2	80	11.23	9	5210	
PBO_80_3	80	12.82	9	3010	

The stress-strain curves obtained from those specimens with strain gauges are plotted in Figure 13b. It should be noted that specimens PBO_5_S_2 and PBO_5_S_3 are not included in Figure 13b since the strain gauges were found to be improperly glued to the fiber bundle and did not provide reliable data. The average measured tensile strength, ultimate strain, and elastic modulus E were 3014 MPa (CoV = 0.068), 0.0145 (CoV = 0.104), and 206 GPa (CoV = 0.065), respectively. The results of the tensile tests indicated that no width effect occurred among fiber nets of different widths. Thus, it was decided that the gripping system was effective and could be used for the direct shear tests. The results of the fiber net tensile tests will be plotted §3.9 in an attempt to compare them with the direct shear test results. The ultimate strength, ultimate strain, and elastic modulus of the PBO fibers provided by the composite manufacturer were 5800 MPa, 0.025, and 270 GPa, respectively [93]. The tensile strength obtained from the tensile tests, although consistent, was substantially lower than the value reported by the manufacturer. The fiber manufacturer was contacted to gain information about the methodology used to conduct the tensile tests. Single yarns (bundles) were tested by the fiber manufacturer, and fibers were twisted to an optimized twist level prior to testing [108]. Given the different testing protocol used in this experimental campaign, a comparison between the results of the tensile tests performed on the fiber net and the values provided by the manufacturer was not attempted.

3.5 General response of the single-lap direct-shear specimens

In this section the experimental results of seventy-eight direct shear tests performed to study the bond characteristics and stress-transfer mechanism of the FRCM composite are presented. The parameter considered in this study were the bonded length and bonded width. In addition, uniaxial electrical resistance gauges were mounted on thirteen specimens with different characteristics to determine the strain profile along the bonded length and validate or modify the applicability of a fracture mechanics approach previously used to describe the FRP-concrete interface [25, 51, 89].

Specimens were named following the notation DS_X_Y_S_D_Z^T, where X=bonded length (ℓ) in mm, Y=bonded width (b_1) in mm, S (if present) indicates strain gauges were mounted on the specimen, D (if present) denotes that the specimen was tested until a constant load at the end of the test was measured, and Z=specimen number. A superscript T after Z indicates that the fiber net was oriented with the transversal fiber bundles directly against the matrix internal layer.

For most of the direct-shear tests herein presented, failure was characterized by considerable slippage between the fibers and matrix. In general, no damage was observed at the matrix-concrete interface, and debonding occurred at the matrix-fiber interface except for specimens DS_100_34_1^T and DS_100_34_2^T. The authors postulate that a fracture mechanics Mode-I condition prevailed in these two tests due to the short bonded length adopted [118].

After the maximum load was reached, longitudinal fiber bundles were observed to gradually pull out of the composite at the loaded end of the bonded area, and longitudinal fibers beyond the unloaded end of the bonded area advanced slowly into the matrix (position y=0 in Figure 11 and Figure 12a). The slippage of the longitudinal bundles relative to the transversal bundles was visibly apparent after the external layer of matrix was removed after completion of testing. No movement was observed of the transversal bundles embedded in the matrix, which suggests that the stress transfer occurs primarily between the longitudinal fiber bundles and the matrix.

As friction among fiber filaments and between fibers and matrix has been reported in the literature for similar composites [16, 56], specimens denoted with a "D" were tested until the entire softening branch of the load response was obtained in order to investigate the residual capacity of the interface related to friction. Specimens tested for this purpose had a relatively long bonded length, ℓ=330 mm or 450 mm, with respect to the entire set of tests. Specimens denoted with D were only a small fraction of the entire set of tests due to the duration of the tests. The remaining specimens, unless they failed prematurely, were tested to a prescribed value of the global slip $\overline{g}$ (when $\ell \le 330\,\text{mm}$ typically $\overline{g} = 5$ mm) corresponding to the descending branch of the load response.

The bonded width b_1, number of longitudinal fiber bundles n across the width, bonded length ℓ, number of layers La, overall thickness of the composite t, peak load P^* and corresponding peak stress σ^* (Eq. (90)) are indicated in Table 4 for each specimen.

It should be pointed out that for seven specimens tested, not included in Table 4, the fibers outside the bonded region reached the tensile strength in one or more bundles as a consequence of the non-uniform distribution of the force across the bundles. This phenomenon will be discussed in Section 3.9 and Section 4.10, and was observed in specimens DS_200_60_1, DS_330_34_3-6, DS_330_43_S_4, and DS_330_43_4.

Tensile failure of the longitudinal fiber bundles was characterized by a rapid stretching of the bare fibers with no increase in applied force. This failure mode occurred suddenly because the direct shear tests were conducted by controlling the slip between the fibers and the concrete substrate. When fiber failure initiated, displacement of the overall system localized at the fiber failure location, which resulted in an unstable loading condition. Similar to the tensile tests, global fracture of the fiber net was not observed.

3.6 Preexisting cracks

Some specimens had preexisting shrinkage cracks on the external surface of the composite (Figure 14). These cracks were typically characterized by a transversal pattern along the bonded length of the composite. These transverse cracks did not appear to extend across the entire width of the composite strip in all cases. The cracks opened with increasing slip and eventually penetrated the thickness of the composite, as could be seen from the side of the specimens. The presence of through-thickness cracks resulted in a discontinuity in the stress transfer between fibers and matrix with consequent localized deformation at the crack locations along the composite bonded length. The presence of shrinkage cracks is strictly dependent on the matrix application. In this study, each matrix batch was mixed under the same external conditions following the same procedure, although not all specimens presented shrinkage cracks. This suggests that the matrix utilized is sensitive to mixing, handling, and/or curing procedures.

Figure 14. Shrinkage cracks on surface of specimen DS_330_43_2.

Table 4. Single-lap direct-shear specimens.

Name	b_1 [mm]	n [-]	ℓ [mm]	La [-]	t [mm]	P^* [kN]	σ^* [MPa]
DS_100_34_1^T	34	4	100	2	8	1.92	1040
DS_100_34_2^T	34	4	100	2	8	0.97	530
DS_100_34_3^T	34	4	100	2	8	1.62	880
DS_100_60_1	60	7	100	2	8	3.69	1150
DS_100_60_2	60	7	100	2	8	3.83	1190
DS_100_60_3	60	7	100	2	8	3.77	1170
DS_150_34_1^T	34	4	150	2	8	2.22	1210
DS_150_34_2^T	34	4	150	2	8	1.55	840
DS_150_34_3^T	34	4	150	2	8	2.87	1560
DS_150_34_4^T	34	4	150	2	8	2.34	1270
DS_150_60_1	60	7	150	2	8	5.25	1630
DS_150_60_2	60	7	150	2	8	5.04	1570
DS_150_60_3	60	7	150	2	8	3.05	950
DS_200_34_1	34	4	200	2	8	3.05	1660
DS_200_34_2	34	4	200	2	8	2.52	1370
DS_200_34_3	34	4	200	2	8	3.44	1870
DS_200_60_2	60	7	200	2	8	5.66	1760
DS_200_60_3	60	7	200	2	8	5.44	1690
DS_200_60_4	60	7	200	2	8	6.58	2040
DS_250_34_1^T	34	4	250	2	8	2.61	1420
DS_250_34_2^T	34	4	250	2	8	2.11	1150
DS_250_34_3^T	34	4	250	2	8	2.82	1530
DS_250_34_4	34	4	250	2	8	3.21	1740
DS_250_34_5	34	4	250	2	8	2.89	1570
DS_250_34_6	34	4	250	2	8	3.61	1960
DS_330_34_1^T	34	4	330	2	8	3.00	1630
DS_330_34_2^T	34	4	330	2	8	3.51	1910
DS_330_34_7	34	4	330	2	8	4.07	2210
DS_330_34_8	34	4	330	2	8	4.02	2180
DS_330_34_9	34	4	330	2	8	3.44	1870
DS_330_43_1^T	43	5	330	2	8	4.43	1930
DS_330_43_2^T	43	5	330	2	8	5.25	2280
DS_330_43_3	43	5	330	2	8	5.27	2290
DS_330_43_5	43	5	330	2	8	4.79	2080
DS_330_43_6	43	5	330	2	8	5.09	2210
DS_330_43_S_1^T	43	5	330	2	8	4.48	1950
DS_330_43_S_2^T	43	5	330	2	8	5.12	2230
DS_330_43_S_3^T	43	5	330	2	8	3.03	1320
DS_330_43_S_5	43	5	330	2	8	4.03	1750

Name	b_l [mm]	n [-]	ℓ [mm]	La [-]	t [mm]	P^* [kN]	σ^* [MPa]
DS_330_60_1^T	60	7	330	2	8	7.05	2190
DS_330_60_2^T	60	7	330	2	8	6.56	2040
DS_330_60_3^T	60	7	330	2	8	6.06	1880
DS_330_60_4^T	60	7	330	2	8	6.50	2020
DS_330_60_5^T	60	7	330	2	8	6.28	1950
DS_330_60_6	60	7	330	2	8	7.01	2180
DS_330_60_D_1	60	7	330	2	8	8.29	2570
DS_330_60_D_2	60	7	330	2	8	7.12	2210
DS_330_60_D_3	60	7	330	2	8	6.56	2040
DS_330_60_D_4	60	7	330	2	8	5.24	1630
DS_330_60_D_5	60	7	330	2	8	6.69	2080
DS_330_60_S_1	60	7	330	2	8	6.30	1960
DS_330_60_S_2	60	7	330	2	8	7.31	2270
DS_330_60_S_3	60	7	330	2	8	6.55	2030
DS_330_80_D_1	80	9	450	2	8	8.90	2150
DS_330_80_D_2	80	9	450	2	8	8.68	2100
DS_330_80_D_3	80	9	450	2	8	8.90	2150
DS_330_80_D_4	80	9	450	2	8	8.42	2030
DS_330_80_D_5	80	9	450	2	8	8.58	2070
DS_450_34_1	34	4	450	2	8	3.77	2050
DS_450_34_2	34	4	450	2	8	3.85	2090
DS_450_34_3	34	4	450	2	8	3.97	2160
DS_450_60_1	60	7	450	2	8	6.40	1990
DS_450_60_2	60	7	450	2	8	6.34	1970
DS_450_60_3	60	7	450	2	8	6.44	2000
DS_450_60_4	60	7	450	2	8	5.77	1790
DS_450_60_5	60	7	450	2	8	6.51	2020
DS_450_60_6	60	7	450	2	8	6.79	2110
DS_450_60_7	60	7	450	2	8	6.65	2060
DS_450_60_D_1	60	7	330	2	8	7.01	2180
DS_450_60_D_2	60	7	330	2	8	6.67	2070
DS_450_60_D_3	60	7	330	2	8	7.33	2270
DS_450_60_S_1	60	7	450	2	8	6.63	2060
DS_450_60_S_2	60	7	450	2	8	8.86	2130
DS_450_80_1	80	9	450	2	8	8.62	2080
DS_450_80_2	80	9	450	2	8	9.07	2190
DS_450_80_3	80	9	450	2	8	9.32	2250
DS_450_80_4	80	9	450	2	8	8.86	2140
DS_450_80_5	80	9	450	2	8	10.04	2420

3.7 Experimental applied load – global slip response

Applied load – global slip responses of representative specimens of different composite bonded widths and the same bonded length (ℓ = 330 mm) are shown in Figure 15a. In general, a linear response is followed by a non-linear response up to the maximum (peak) load P^*. In the pre-peak non-linear response, several phenomena occur at the matrix-fiber interface. A detailed description of the interfacial stress-transfer mechanism that takes place in the non-linear pre-peak part of the load response will be presented in the next sections. It should be noted, however, that microdamage of the matrix-fiber interface, near the loaded end, characterizes the onset of the non-linear part. Once coalescence of the microcracks occurs, debonding initiates. As debonding progresses, the load increases due to the presence of friction that has been observed between fibers filaments and between fibers and matrix [16] in the debonded area, which contributes to the interfacial shear and thus the applied load. The descending post-peak response has a variable gradient and indicates that the stress transfer is no longer fully established. The friction contribution alone is clearly identified in the load responses of specimens DS_330_60_D_3 and DS_330_60_D_5, reported in Figure 15a, which become constant for global slip values greater than approximately 9 mm.

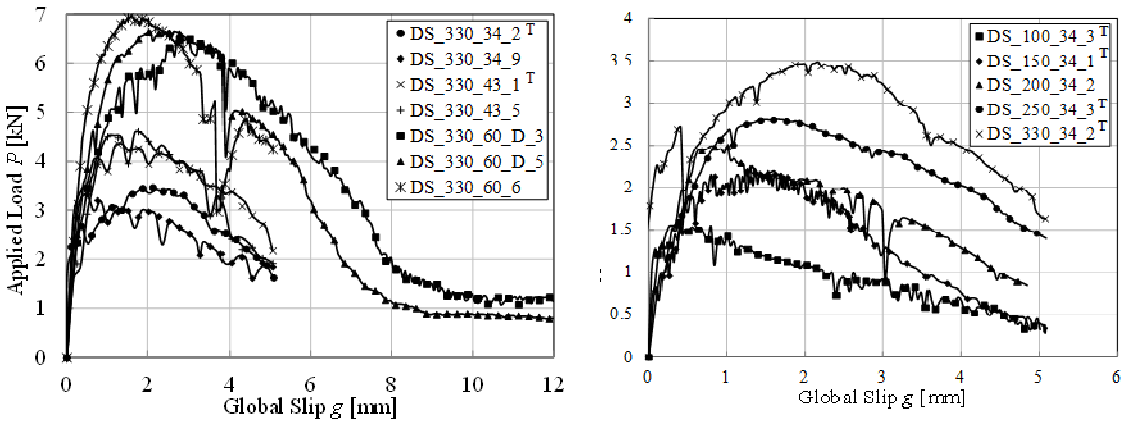

a. b.

Figure 15. Applied load-global slip response of representative specimens. a) Representative DS_330 Series specimens. b) Representative DS_XXX_34 Series.

For those specimens with preexisting shrinkage cracks, sudden drops in the load responses were observed as the cracks started to propagate towards the longitudinal edges of the composite. Comparing the results of specimens with and without preexisting shrinkage cracks, it was determined that the overall behavior of the specimens appeared to be generally unaffected by the presence of preexisting shrinkage cracks.

The load responses of representative specimens in the DS_XXX_34 series with different bonded lengths and the same bonded width (b_1 = 34 mm) are plotted in Figure

15b. Figure 15b shows initial overlap in the linear pre-peak responses, and specimens with longer bonded lengths continuing up to higher peak load levels. Comparing the overlapping response of specimens shown in Figure 15b suggests that for low load levels, the shear stress transfer and the debonding develop close to the loaded end of the composite; then with increasing applied load, they progress from the loaded end to the free end.

The load responses of representative specimens DS_330_60_D_5, DS_330_80_D_1, and DS_450_60_D_1 are plotted in Figure 16a. The same load responses are also plotted in Figure 16b in terms of the nominal stress σ defined in Eq. (89). Eq. (89) is used to normalize the applied load in order to compare the results of specimens with different bonded widths. The cross-sectional area of the fibers in the longitudinal direction nb^*t^* was used to normalize the applied load P because in the direct-shear tests carried out the load is transferred from the fibers to the matrix. Figure 16a and Figure 16b are representative of the majority of the tests presented in this study in which debonding occurred at the matrix-fiber interface.

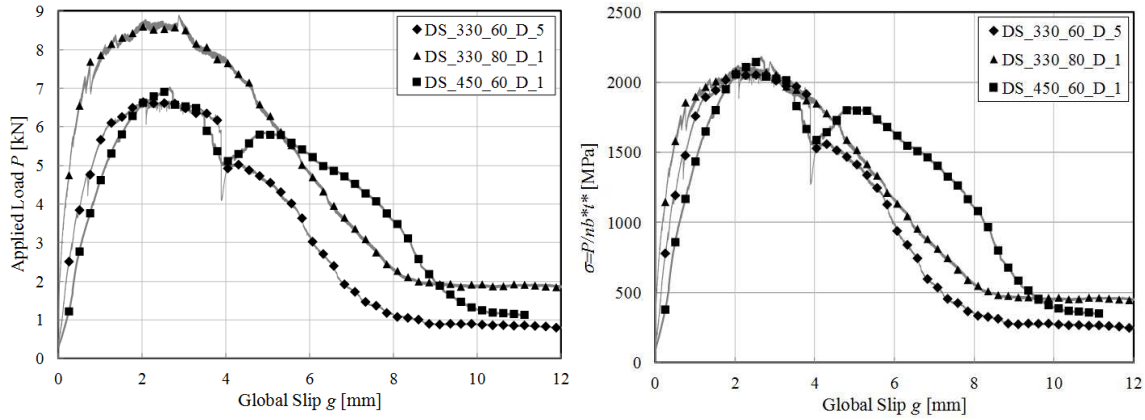

a. b.

Figure 16. a) Applied load P vs. global slip g plot for specimens DS_330_60_D_5, DS_330_80_D_1, and DS_450_60_D_1. b) Normal stress σ vs. global slip g plot for specimens DS_330_60_D_5, DS_330_80_D_1, and DS_450_60_D_1.

It should be noted that for the case of FRP-concrete joints with a bonded length greater than a certain critical length (termed the effective bond length), a region of constant applied load with increasing slip is observed when the applied load reaches the so-called debonding load (see Figure 3), and debonding propagates along the bonded length towards the free end [98, 99]. A constant applied load region is not observed for the FRCM specimens (see Figure 16 and Figure 17) because friction between the debonded fibers and matrix should alter the load response as discussed previously. Additional discussion is provided in the next sections regarding the effective bond length.

3.8 Idealized applied load – global slip response

Figure 17a shows an idealized applied load – global slip response put forward by combining the information inferred from the load responses of the specimens herein presented and the experimental and analytical evidence available in the literature [16, 39, 56]. A Mode-II interfacial crack propagation is assumed to occur at the matrix-fiber interface. The first part of the idealized $P-g$ response is represented by a linear branch (OA) associated with elastic behavior of the bond between the fibers and the matrix. After point A (Figure 17a), the response starts to be nonlinear; the interface between the fibers and the matrix experiences some micro-damage, and the value of the applied load P increases until the onset of debonding at the matrix-fiber interface, which corresponds to point B in Figure 17a. After point B, if the idealized $P-g$ curve referred to FRP-concrete joints, a self-similar stress-transfer mechanism [25, 98, 99] would shift along the bonded length, and the load would remain constant while the slip increases. Such behavior would be represented by the dashed dashed line in Figure 17a. In FRCM composites friction between single fiber filaments and between fibers and matrix [16, 56] occurs in that portion of the composite where the fibers have debonded. Consequently, an increase in the applied load after the debonding initiates (point B) is observed until point C. The applied load at point B is also referred to as the debonding load, P_{deb}, or the load-carrying capacity of the matrix-fiber interface. If it is assumed that friction depends only on the material characteristics and the contact area between the debonded fibers and the matrix, and it does not decrease with increasing slip, its contribution can be assumed to result in a linear increase in P with the increase of the debonded length. An effective bond length l_{eff}, i.e. the minimum length needed to develop the load-carrying capacity of the interface P_{deb} [32, 99], if it exists, can be determined from the strain distribution along the longitudinal fibers for points of the load response between points B and C, provided that the contribution of friction is clearly identified. Further discussion on the effective bond length will be provided in the next sections, where the stress-transfer mechanism will be investigated.

The different stages of the stress-transfer mechanism for the various points of the load response depicted in Figure 17a are shown in Figure 17b. The residual bonded length l_r is defined as the actual length of the bonded area, i.e. $l_r = \ell$ between points O and B. Between points B and C the applied load increases due to friction until the debonding process reaches the end of the bonded area. At point C, the applied load reaches the maximum (or peak) load P^*, and the residual bonded length is equal to the effective bond length ($l_r = l_{eff}$) (Figure 17b). After point C, the applied load starts to decrease because the bond mechanism is no longer fully established ($l_r < l_{eff}$). After point D, the curve's concavity changes, and the applied load reduces at increasing rate. At this stage the residual bonded length l_r is considerably reduced. It should be noted that in FRP-

concrete joints, mixed–mode fracture propagation occurs at the free end of the composite when $l_r < l_{eff}$ [28]. This aspect was not investigated in this work, and no measurements were attempted at the free end of the FRCM strip. At point E, the fibers are completely debonded from the matrix ($l_r = 0$), and the only residual contribution to the applied load is provided by friction. Thus, the load response becomes constant after point E with an applied load P_f, which is associated with friction. It should be noted that two different friction contributions can be distinguished: friction between fiber filaments, caused by the mutual contact of single filaments within the fiber bundle, and friction between fibers and matrix, caused by the slippage of the fibers within the matrix. The former is always present due to the different impregnation of the filaments within the fiber bundles, whereas the latter provides its contribution after the onset of debonding.

The shear stress τ_f associated with friction can be determined from the applied load at point E:

$$\tau_f = \frac{P_f}{2nb^*\ell} \tag{91}$$

where $nb^*\ell$ is the nominal bonded area of one matrix-longitudinal fiber interface. The coefficient 2 takes into account that the contact area between fibers and matrix is twice the bonded area of one matrix-longitudinal fiber interface ($nb^*\ell$) because the fibers slip with respect to both layers of matrix (see also Figure 27). Eq. (91) does not take into account the thickness t^* of the longitudinal fiber bundles in evaluating the contact area because the thickness t^* is much smaller than the width of the bundle, and its contribution to the contact area can be neglected. The average value of τ_f obtained from all specimens denoted with D was 0.06 MPa (CoV=0.245).

The difference between the load at C, which corresponds to the peak load P^*, and the load at B, which corresponds to the debonding load P_{deb}, is related only to friction:

$$P^* - P_{deb} = 2\tau_f nb^*\left(\ell - l_{eff}\right) \tag{92}$$

where $nb^*\left(\ell - l_{eff}\right)$ is the portion of the original bonded area in which the fiber bundles are subject to friction at point C ($l_r = l_{eff}$, see Figure 17b).

It should be pointed out that in the description of the idealized load response of Figure 17a, it was assumed that friction was present only after point B. However, two different friction contributions, namely friction between fiber filaments and friction between fibers and matrix, can be recognized. A refined analysis should be carried out to identify the contribution and nature of friction that potentially occurs between fibers filaments, between the matrix and fibers, and between the longitudinal and transversal fiber bundles. The contribution of friction between fiber filaments and between the

longitudinal and transversal fiber bundles before the onset of debonding is included in the macro-fracture model of the matrix-fiber interface presented in this chapter.

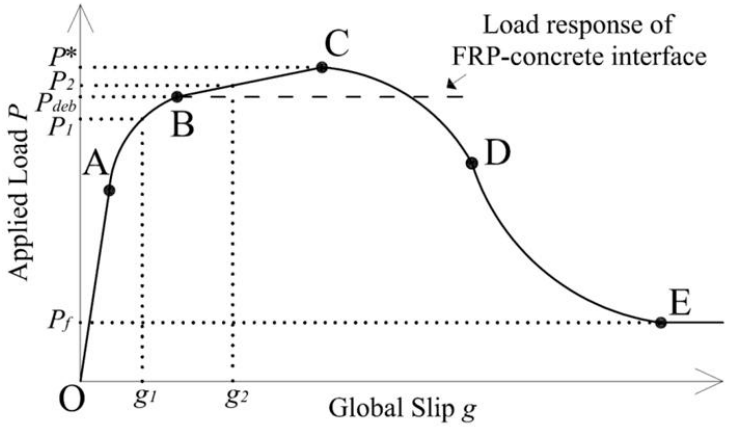

a.

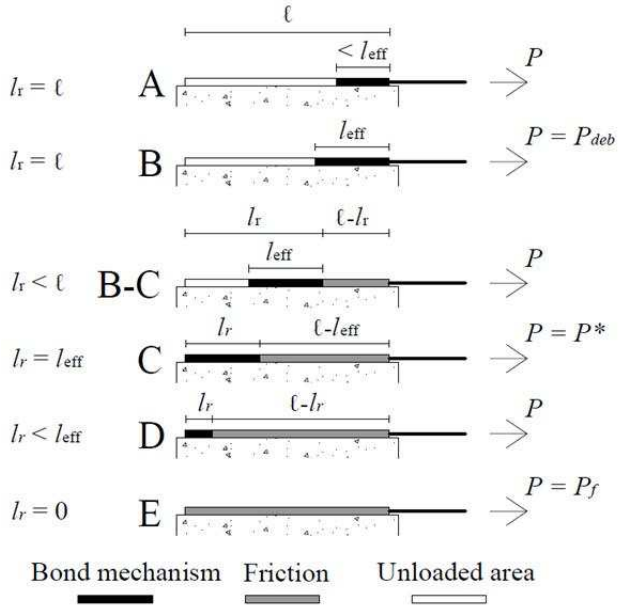

b.

Figure 17. a) Idealized applied load P vs. global slip g response. b) Stress-transfer mechanism stages corresponding to different points of the idealized $P - g$ response.

3.9 Influence of the composite bonded width

Figure 18 shows the results obtained in terms of peak stress σ^* for different composite bonded widths (b_1) for the test specimens with a bonded length ℓ=330 mm (DS_330 Series). Specimens denoted with D and S were included in the plot of Figure 18. The results, in terms of σ^*, of the fiber net tensile tests (PBO Series) are included for comparison. Four different composite bonded widths b_1 are shown (b_1 = 34 mm, 43

mm, 60 mm and 80 mm). For each width of the DS_330 Series and the PBO Series, the average value of the ultimate stress is reported with a black filled marker. The average values of the ultimate stress for all tensile tests and all single-lap shear tests plotted in Figure 18 are reported with dashed lines.

Pull-out tests of a single bundle of fibers indicated that failure of the fiber bundle is governed by the so-called *telescopic* behavior, i.e. the sequential failure of the fibers from the external sleeve to the internal core of the bundle [16]. This behavior is attributed to an uncontrolled variation in matrix impregnation between the fibers directly in contact with the matrix and those inside the bundle. Although it is possible that a width effect exists considering a single bundle of fibers, Figure 18 suggests that a *global* width effect does not exist among multiple bundles and therefore for the entire width of the composite. The absence of a global width effect constitutes a unique characteristic of FRCM composites when compared to FRP composites [25, 98, 99, §1.5].

The ratio between the average of the ultimate stress σ^* of the single-lap direct-shear tests (2044 MPa) and of the fiber tensile tests (3014 MPa) is 0.68. This ratio should not be considered as an indication of the bond performance of the composite with respect to the tensile strength of the fiber net because the ultimate stress obtained from the single-lap direct-shear tests is due not only to the bond but also to the friction between the fibers and between the matrix and the fibers that entails for an increase in the applied load once the debonding has initiated (see Eq. (92)).

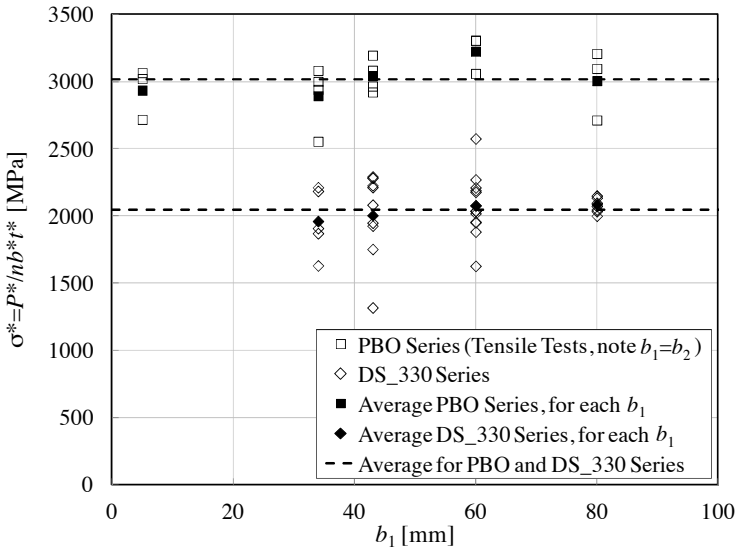

Figure 18. Comparison of the ultimate stress σ^* vs. bonded width b_1 for single-lap direct-shear tests (DS_330 Series) and tensile tests (PBO Series).

The results obtained for bonded widths b_1 = 34 mm and b_1 = 43 mm show a larger scatter with respect to the other widths. This can be explained by the fact that the bundles placed at the edges of the composite are not completely surrounded by the

matrix ($b_1 = b_2$), and therefore they are unable to develop the same bond capacity as the bundles inside the composite strip with matrix on each side. Moreover, the fact that the fibers are woven in discrete bundles can result in some of the bundles debonding before the others, leading to a non-uniform distribution of the load across the bonded width. An indication of the non-uniform distribution of the load among the bundles is provided by the difference between the measurements of the two LVDTs, which is the result of the rotation of the Ω-shaped bent plate attached to the transversal fibers. A more detailed analysis of the non-uniform distribution of the load among bundles will be provided in the next sections.

3.10 Strain analysis

3.10.1 Test set-up of specimens equipped with strain gauges

The results of nine specimens instrumented with strain gauges are presented in this chapter. The parameters varied were the bonded length and bonded width. It should be noted that the results of specimen DS_330_43_S_4, not reported in Table 4, were disregarded because the fibers outside the bonded region reached the tensile strength in one or more bundles.

a. Specimen DS_330:

All DS_330 specimens	DS_330_60_S_2	DS_330_60_S_3
$y_1 = y_2 = y_3 = 490$ mm	$y_2 = 490$ mm	$y_2 = 490$ mm
$y_4 = 330$ mm	$y_4 = 330$ mm	$y_4 = 330$ mm
$y_5 = 290$ mm	$y_5 = 315$mm	$y_5 = 315$mm
$y_6 = 260$ mm	$y_6 = 300$ mm	$y_6 = 295$ mm
$y_7 = 220$ mm	$y_7 = 280$ mm	$y_7 = 280$ mm
$y_8 = 160$ mm	$y_8 = 150$ mm	$y_8 = 225$ mm
$y_9 = 50$ mm	$y_9 = 155$ mm	$y_9 = 175$ mm
		$y_{10} = 70$ mm

b.Specimen DS_450:

$y_2 = 610$ mm
$y_4 = 450$ mm
$y_5 = 430$ mm
$y_6 = 415$ mm
$y_7 = 400$ mm
$y_8 = 380$ mm
$y_9 = 330$ mm
$y_{10} = 275$ mm
$y_{11} = 220$ mm
$y_{12} = 150$ mm

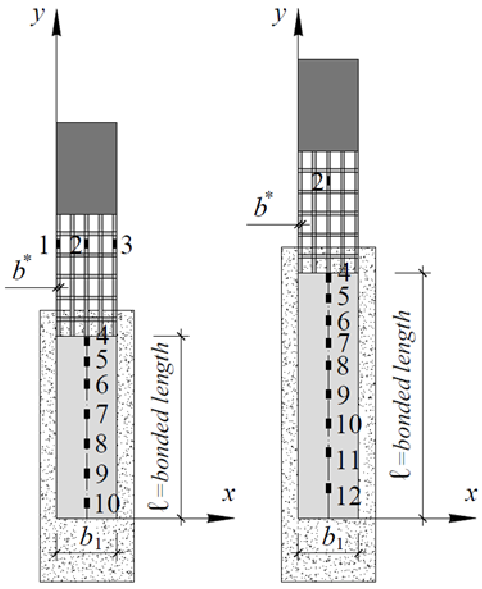

Figure 19. Positions of the strain gauges for specimens in DS_330 Series (a) and DS_450 Series (b).

The axial strain profiles and the interfacial parameters presented in this chapter refer to the Cartesian system shown in Figure 11, Figure 12, and Figure 19. Positions of the strain gauges along the bonded length are illustrated in Figure 19 for specimens in series DS_330 and DS_450. For some specimens the number and position of the strain gauges were varied in order to determine the best configuration to capture the entire strain profile along the composite strip. Two different modalities of applications of the strain gauges were adopted. For specimens DS_330_43_S_1^T and DS_330_43_S_2^T, slots were created during the application of the matrix external layer, and the strain gauges were applied onto the fiber after the composite set (Figure 20a). This procedure was similar to that used by D'Ambrisi et al. [131]. However, some concerns arose regarding possible stress concentration at the edges of the matrix slots. In addition, the complete absence of the external layer of matrix where the strain gauges were applied could potentially entail for a different bond behavior of the fibers. Hence, for the remaining specimens the strain gauges were mounted to the fiber bundles prior to embedding them in the external layer of matrix (Figure 20b).

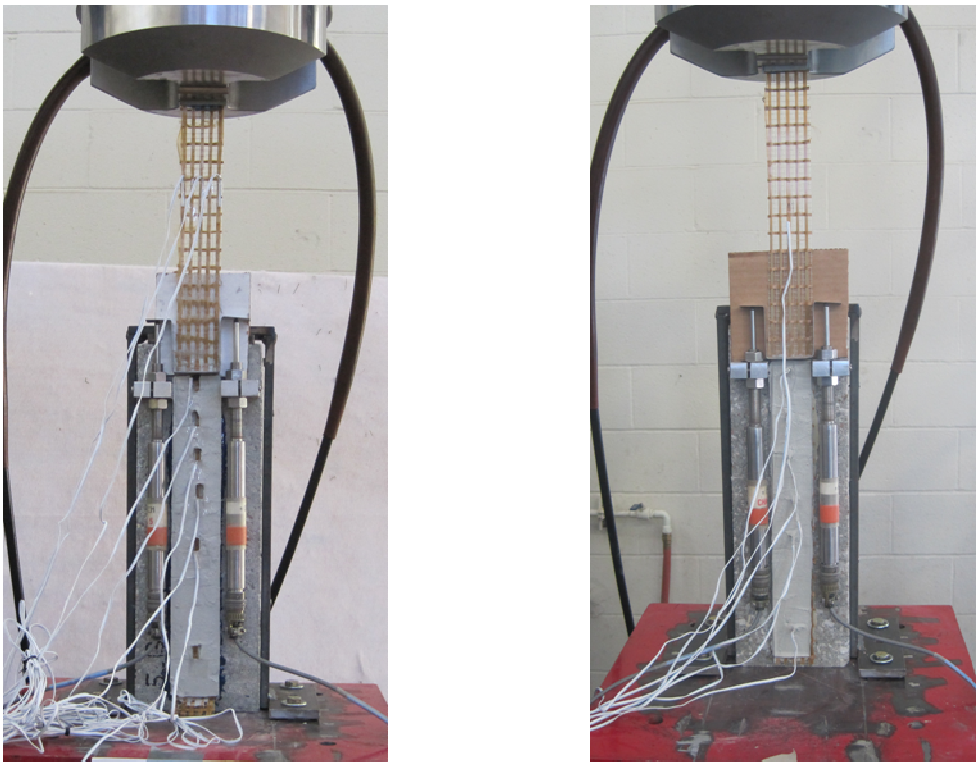

a. b.

Figure 20. a) Photo of specimen DS_330_43_S_2^T. b) Photo of specimen DS_330_43_S_3^T

3.10.2 Applied load – global slip response of specimens equipped with strain gauges

Load responses of specimens with strain gauges in the DS_330_43 series are reported in Figure 21a. Specimens DS_330_43_1^T and DS_330_43_5 are also plotted for comparison. In addition, the applied load – global slip response of specimens in the

DS_330_60 series and in the DS_450_60 series are reported in Figure 21b and Figure 22, respectively. Specimens DS_330_60_D_3 and DS_450_60_D_3 are also reported for comparison in Figure 21b and Figure 22, respectively. In general, the maximum load for specimens with strain gauges is consistent with similar specimens without strain gauges. However, for specimens DS_330_43_S_1^T and DS_330_43_S_2^T, the non-linear pre-peak response appears to be more emphasized. It is possible that the slots used to mount the strain gauges on specimens DS_330_43_S_1^T and DS_330_43_S_2^T induced a stress concentration at the gauge locations or modified the restraining action of the matrix, which highlighted the need to investigate the role of the external layer of the matrix (see §1).

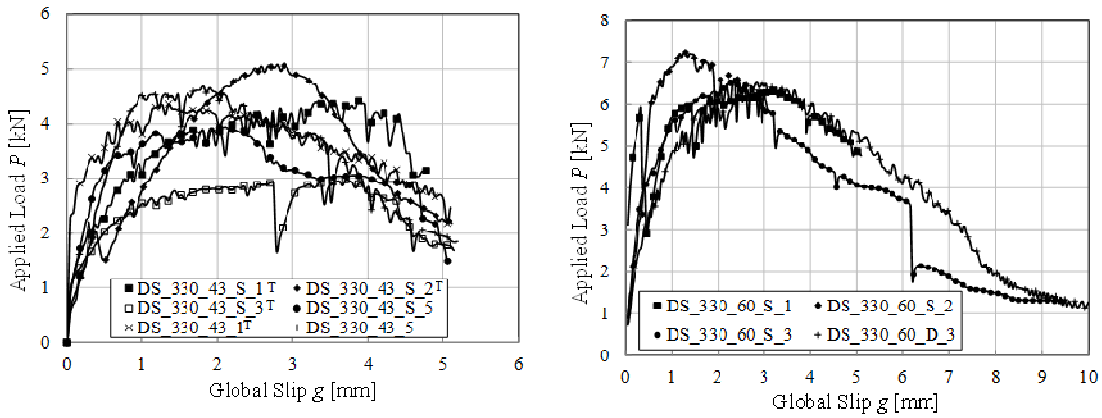

a. b.

Figure 21. a) Specimens in the DS_330_43_S series. **b)** Specimens in the DS_330_60_S series.

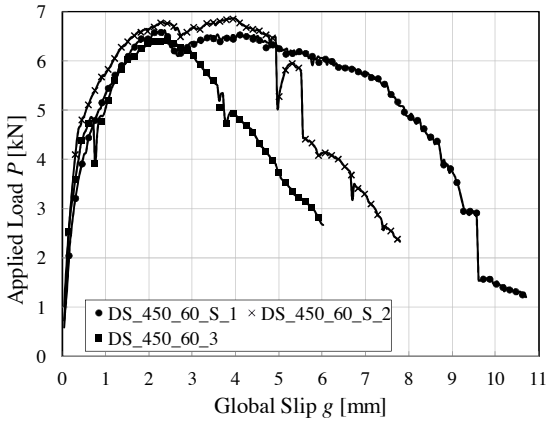

Figure 22. Specimens in the DS_450_60 series.

Specimens DS_330_43_S_3^T and DS_330_43_S_5, with strain gauges embedded in the matrix, show a load response similar to DS_330_43_1^T and DS_330_43_5 without strain gauges. It should be noted that specimens with a bonded with b_1 = 43 mm present show a more scattered behavior with respect to specimens with b_1 = 60 mm, which

confirms that the different impregnation of the bundles placed at the edges and the non-uniform distribution of the load across the width are more emphasized for small bonded widths and become almost negligible as the bonded width increases.

3.10.3 Strain outside the bonded region

To examine the load distribution among the different fiber bundles, the central and edge bundles of specimens DS_330_43_S_1^T and DS_330_43_S_2^T were instrumented with strain gauges in positions 1, 2, and 3 on the bare fibers (Figure 19). Gauges 1 and 3 were omitted for the remaining specimens.

The strains at different percentage of P^* in the central (gauge 2) and edge bundles (gauges 1 and 3), outside the bonded region, of specimens DS_330_43_S_1^T and DS_330_43_S_2^T are reported in Figure 23 and Figure 24, respectively. The average AVG of the strain recorded outside the bonded region is reported in Figure 23 and in Figure 24 with a black filled marker for 10%, 40%, 50%, and 75% of P^*, and is reported with a bold × when the applied load is equal to P^*. The coefficient of variation of each average value is reported between brackets beside the correspondent marker. A non-uniform strain distribution is observed among the three bundles in both specimens, although the scatter observed for specimen DS_330_43_S_2^T (Figure 24) is smaller than that observed for specimens DS_330_43_S_1^T (Figure 23). This phenomenon, which was already observed analyzing the ultimate stress σ^* for different bonded width b_1 (Figure 18), is similar to that observed in FRP strips attached to concrete, and it is partially due to the local variation of the interfacial properties [25]. In the case of discrete bundles this phenomenon appears to be more pronounced.

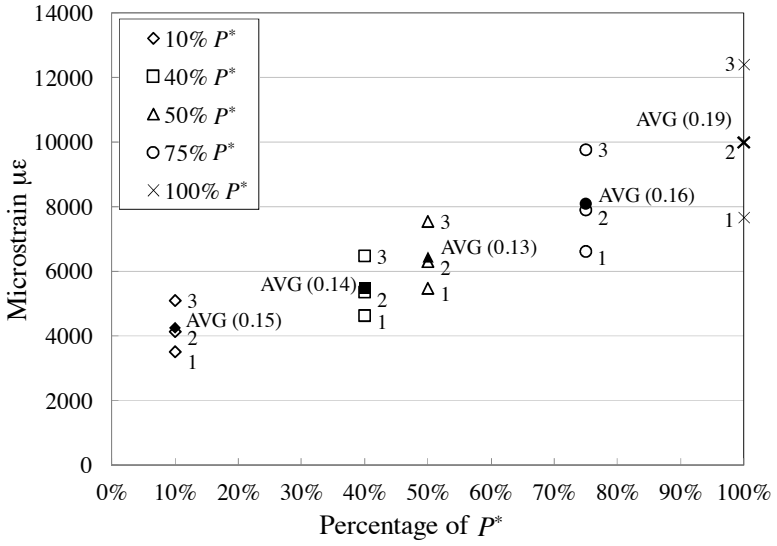

Figure 23. Strain in central and edge bundles of specimens DS_330_43_S_1^T outside the bonded region.

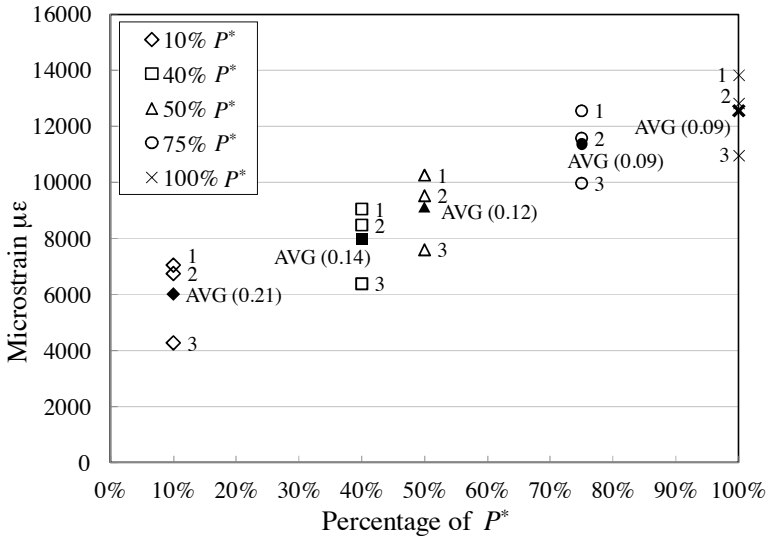

Figure 24. Strain in central and edge bundles of specimens DS_330_43_S_2^{T} outside the bonded region.

Figure 23 and Figure 24 show a linear relationship between the applied load and the strain in the bundles outside the bonded region. If the average stress of the bundles is computed, the results of Figure 23 and Figure 24 can be used to calculate the elastic modulus of the fibers. Values computed confirm the value provided by the manufacturer.

3.10.4 Analysis of the strain profiles within the bonded region

As discussed in §1.5 analysis of the axial strain on the surface of FRP composites bonded to concrete indicates that the zone in which the stress is transferred from the concrete substrate to the composite, the so-called stress transfer zone (STZ), is fully established for bonded lengths greater than the effective bond length when the load attains the value corresponding to debonding initiation. An increase of the global slip after initiation of the debonding process results in a simple translation of the STZ further along the bonded length of the composite while its shape remains constant [25, 98, 99]. Hence, the axial strain distribution along the FRP composite can be evaluated for any point of the load response after the onset of the debonding process. In FRCM composites, conversely, the presence of friction between single filaments and between fibers and matrix modifies the shape of the strain distribution at the loaded end once debonding has initiated. For this reason, the strain profiles of FRCM composites can be examined to determine the unique load value at which the bond mechanism is fully established and friction is not yet present (i.e. point B in Figure 17a). If the strain profiles after point B are used to determine the STZ, the contribution of friction should be clearly identified in order to determine the fracture properties related to bond; otherwise they will be overestimated.

The point at which the stress-transfer mechanism is fully established and debonding starts to propagate (i.e. point B in Figure 17a) is not easily determined from the

experimental results. For this reason, the strain profiles corresponding to four points of the load response located in a small region around the assumed position of point B were considered. The range of load that defines the small region around point B and the corresponding range of g are named $(P_1 - P_2)$ and $(g_1 - g_2)$, respectively, and are illustrated in Figure 17a. The region and the position of point B were identified a posteriori by the change in the slope of the load response, together with a sudden drop in the applied load caused by the formation of the debonding crack. Additionally, the choice of points used to analyze the strain profile is supported by the observation that for values of the global slip g greater than those corresponding to the points used, the strain gauge closest to the loaded end, i.e. gauge number 4 in Figure 19, showed a sudden increase in measured strain to values that were very large and almost constant. This can be interpreted as proof that the debonding process had initiated, since after that the mechanical interlocking provided by the matrix, which induced increasing shear stresses at the fiber-gauge interface, caused the debonding of the gauges from the fibers.

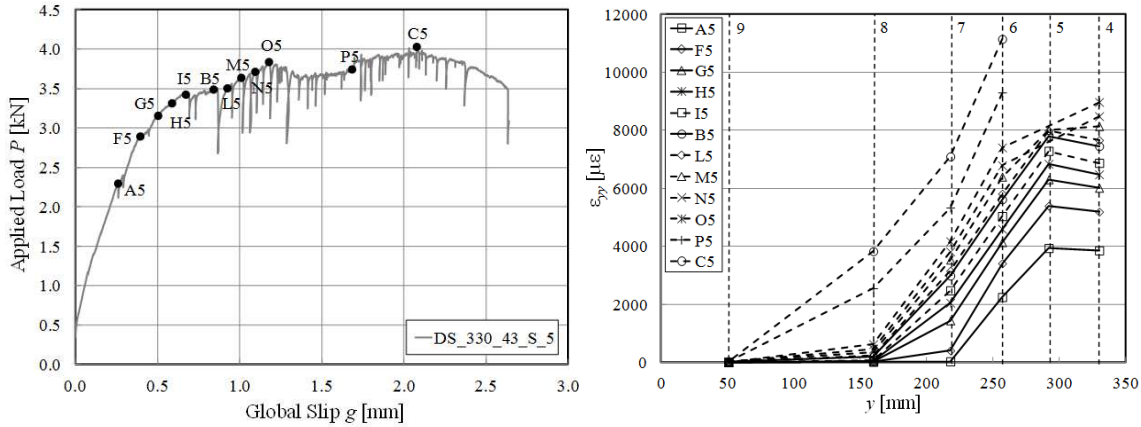

a. b.

Figure 25. a) Applied load P vs. global slip g plot for specimen DS_330_43_S_5. b) Axial strain ε_{yy} profiles along the bonded length for representative points of specimen DS_330_43_S_5.

The load response of specimen DS_330_43_S_5 is shown in Figure 25a. The strain profiles along the bonded length corresponding to the points indicated in Figure 25a are shown in Figure 25b. Points A5, B5, and C5 in Figure 25a correspond to points A, B, and C in Figure 17a, respectively. The vertical dashed lines in Figure 25b are numbered according to the corresponding gauge (Figure 19). Strain values from gauge 4 of specimen DS_330_43_S_5 are not reported in Figure 25b for points P5 and C5, while strain values from gauge number 5 are not reported for points N5, O5, P5, and C5; strains measured in these positions were not consistent with the values recorded by gauges in the same position on other specimens or with values recorded by the closest gauges. This is likely due the onset of debonding which caused the detachment of the

gauges. Interestingly, gauge 5 detached before gauge 4 probably due a different matrix-fiber bond condition along the longitudinal fibers.

The idealized axial strain profiles corresponding to three points of the load response of Figure 17a are illustrated in Figure 26a. The linear part of the strain profile close to the loaded end is related to friction, which causes a linear increase of the strain at the loaded end related to the debonded length $\left(\ell - l_r\right)$ (Figure 17b).

The strain profiles obtained from each specimen equipped with strain gauges were approximated using Eq. (93), which represents a modification of a function used for FRP-concrete joints [25, 98, 99] to take into account friction in the debonded area:

$$\varepsilon_{yy} = \varepsilon_0 + \frac{\alpha + ky}{1 + e^{\frac{y - y_0}{\beta}}} \tag{93}$$

$$k = \frac{2 \cdot \tau_f}{E \cdot t^*} \tag{94}$$

ε_0, α, β, and y_0 were determined using nonlinear regression analysis of the measured strains, whereas τ_f is computed according to Eq. (91).

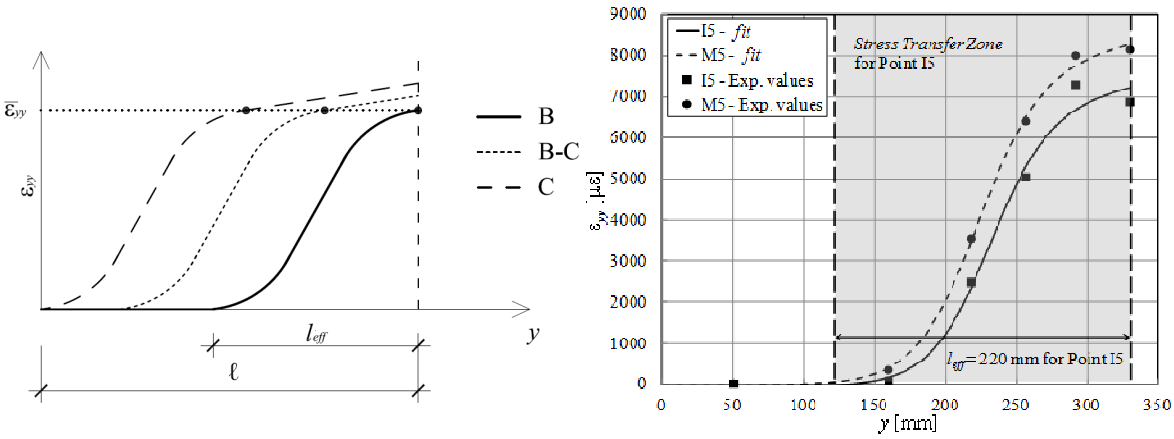

a. b.

Figure 26. a) Idealized axial strain ε_{yy} profiles for points in Figure 17a. b) Fitting of the axial strain ε_{yy} profiles for points I5 and M5 of specimen DS_330_43_S_5 in Figure 25a.

The strain distribution obtained in this manner follows an "S" shape with a value nominally equal to zero toward the free end and a linear increasing value where the fibers debonded from the matrix at the loaded end. The fitting curves (*fit*) obtained from Eq. (93), and corresponding to points I5 and M5 for specimen DS_330_43_S_5, are shown in Figure 26b.

It should be noted that for specimen DS_330_43_S_5 the four points within the small region around point B (Figure 17a) were identified as I5, B5, L5, and M5. Similarly to the FRP-concrete interface discussed in §1.5, the length needed to fully establish the

stress transfer zone (STZ) and the bond mechanism, i.e. the effective bond length l_{eff}, can be defined as the distance between the two points of the strain distribution in which the derivative is equal to zero at the free end and the derivative is constant at the loaded end [134]. The effective bond length for point I5 is shown in Figure 26b. The average value of the effective bond length obtained from the four points within the small region around point B, the load range $(P_1 - P_2)$, and the global slip range $(g_1 - g_2)$for each specimen equipped with strain gauges are reported in Table 5. The average value of l_{eff} for the nine specimens presented in this section is 260 mm (CoV=0.094).

It should be noted that the effective bond length in the case of the PBO FRCM composite is much longer than the effective bond length that typically characterizes the FRP-concrete interface [25, 98, 99]. The reason for this difference can be attributed to the different nature of the debonding mechanism that for the case of FRP composites takes place within the concrete substrate, whereas for PBO FRCM composites mainly develops between the matrix and the embedded fibers. For the FRP-concrete interface, the effective bond length and the fracture process are related to the fracture process zone of the concrete substrate. In FRCM-concrete joints macro-fracture of the matrix and particles of matrix attached on the fibers were not observed, which potentially indicates that, for the tests presented in this study, the interfacial crack propagation does not occur in a thin layer of matrix close to the fibers but rather is associated with the failure of the chemical and mechanical bond between matrix and fibers.

Table 5. Results obtained through the strain analysis and fracture mechanics approach for specimens instrumented with strain gauges.

Name	l_{eff} [mm]	$(g_1 - g_2)$ [mm]	$(P_1 - P_2)$ [kN]	P_{deb}^{exp} [kN]	$\bar{\varepsilon}_{yy}$ [με]	G_F^{dis} [J/m^2]	G_F^{fit} [J/m^2]
DS_330_43_S_1^T	300	(1.7, 2.3)	(3.90, 4.11)	3.96	8760	360	450
DS_330_43_S_2^T	280	(1.5, 1.8)	(3.98, 4.39)	4.17	11020	630	680
DS_330_43_S_3^T	280	(1.2, 1.5)	(2.63, 2.72)	2.71	8200	350	240
DS_330_43_S_5	230	(0.7, 1.0)	(3.42, 3.64)	3.51	7770	270	300
DS_330_60_S_1	260	(0.9, 1.2)	(5.51, 5.91)	5.74	8920	350	360
DS_330_60_S_2	225	(0.7, 0.9)	(6.49, 6.75)	6.65	10420	480	550
DS_330_60_S_3	240	(1.1, 1.4)	(5.63, 5.90)	5.75	10320	480	470
DS_450_60_S_1	255	(1.1, 1.3)	(5.50, 5.91)	5.70	8970	420	540
DS_450_60_S_2	255	(0.9, 1.1)	(5.67, 5.91)	5.77	8320	320	430

3.11 Fracture mechanics approach

The fracture mechanics approach used for FRP-concrete joints [69, §1.6] was extended to the case of FRCM-concrete joints in this study. A Mode-II failure at the fiber-matrix interface was assumed. Since the debonding takes place at the matrix-fiber interfaces,

the displacement of the concrete support is much smaller than the displacement of the FRCM strip and, hence, can be neglected. An infinitesimal segment of a single fiber bundle is illustrated in Figure 27. The slip between the PBO fiber and the matrix interfaces is denoted by s^j, whereas the axial stress in the fibers and the shear stress at the interfaces are denoted by σ_{yy} and τ_{zy}^j, respectively. The superscript *j* is equal to *i* or *e*, in order to indicate the internal or external matrix layer, respectively.

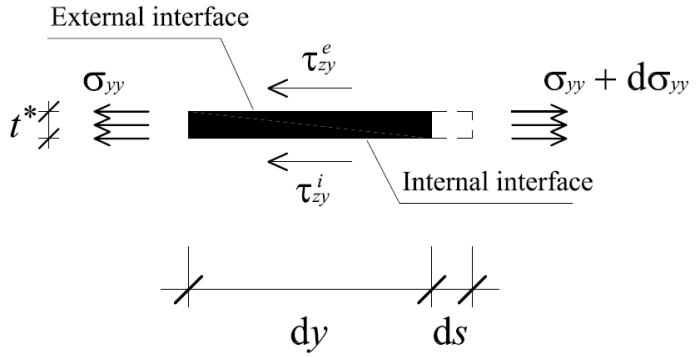

Figure 27. Equilibrium of an infinitesimal segment of fiber embedded into the matrix.

The equilibrium condition can be written as:

$$d\sigma_{yy} \cdot b^* t^* = \left(\tau_{zy}^i + \tau_{zy}^e\right) \cdot b^* dy \tag{95}$$

Considering the fiber segment represented in Figure 27 as a free-body, the work done by the external forces can be written as:

$$dW_{ext} = \left[\left(\sigma_{yy} + d\sigma_{yy}\right) \cdot \left(v + dv\right) - \sigma_{yy} \cdot v\right] \cdot b^* t^* - \left(\tau_{zy}^i \cdot s^i + \tau_{zy}^e \cdot s^e\right) \cdot b^* \cdot dy \tag{96}$$

where v is the axial displacement of the fiber net. If the deformation of the matrix layers and the concrete substrate can be neglected and consequently $s^i = s^e = v = s$, then Eq. (96) can be rewritten as:

$$dW_{ext} = \left[\left(\sigma_{yy} + d\sigma_{yy}\right) \cdot \left(s + ds\right) - \sigma_{yy} \cdot s\right] \cdot b^* t^* - \left(\tau_{zy}^i + \tau_{zy}^e\right) \cdot s \cdot b^* \cdot dy \tag{97}$$

Neglecting the terms of higher order and substituting Eq. (95), Eq. (97) can be written as:

$$dW_{ext} = \sigma_{yy} \cdot b^* t^* ds \tag{98}$$

The integration of Eq. (95) yields:

$$\sigma_{yy} \cdot b^* t^* = \int_0^y \left(\sum_{j=i,e} \tau_{zy}^j \right) \cdot b^* dy \tag{99}$$

Substituting Eq. (99) into Eq. (98):

$$dW_{ext} = \int_{s(0)}^{s(y)} \left(\sum_{j=i,e} \tau_{zy}^{j} \right) \cdot b^{*} dy\, ds \tag{100}$$

$$W_{ext} = \int_{\Pi} \left(\int_{s(0)}^{s(y)} \sum_{j=i,e} \tau_{zy}^{j}\, ds \right) d\Pi \tag{101}$$

where $d\Pi = b^{*} dy$. If $\Psi = b^{*} t^{*} y$ is the volume of the PBO fiber segment from 0 to y, and the fiber behavior can be assumed linear elastic up to failure, the work done by the internal forces can be expressed by Eq. (102):

$$W_{\text{int}} = \int_{\Psi} \left(\int_{0}^{\varepsilon_{yy}} \sigma_{yy} \left(\varepsilon_{yy} \right) d\varepsilon_{yy} \right) d\Psi = \frac{b^{*} t^{*}}{2E} \int_{0}^{y} \sigma_{yy}^{2}\, dy \tag{102}$$

Equating the internal and external work:

$$b^{*} \int_{0}^{y} \left(\int_{s(0)}^{s(y)} \sum_{j=i,e} \tau_{zy}^{j}\, ds \right) dy = \frac{b^{*} t^{*}}{2E} \int_{0}^{y} \sigma_{yy}^{2}\, dy \tag{103}$$

Let:

$$\Phi^{i} = \int_{s(0)}^{s(y)} \tau_{zy}^{i}\, ds \tag{104}$$

$$\Phi^{e} = \int_{s(0)}^{s(y)} \tau_{zy}^{e}\, ds \tag{105}$$

Substituting Eq. (104) and Eq.(105), Eq. (103) can be written as:

$$b^{*} \int_{0}^{y} \left(\Phi^{i} + \Phi^{e} \right) dy = \frac{b^{*} t^{*}}{2E} \int_{0}^{y} \sigma_{yy}^{2}\, dy \tag{106}$$

Since Eq. (106) must be satisfied for each y along the bonded length, the following two relationships can be written:

$$\Phi^{i} + \Phi^{e} - \frac{t^{*}}{2E} \sigma_{yy}^{2} = 0 \tag{107}$$

Assuming that there is no slip at the free end, i.e. $s(0) = 0$, if $y = l_{eff}$ then Eq. (104) and Eq. (105) are integrated from 0 to $s(l_{eff}) = s_{f}$:

$$G_{F}^{i} = \int_{0}^{s_{f}} \tau_{zy}^{i}\, ds \tag{108}$$

$$G_{F}^{e} = \int_{0}^{s_{f}} \tau_{zy}^{e}\, ds \tag{109}$$

Eq. (108) and Eq. (109) represent the fracture energies needed to create and fully break a unit crack of the matrix-fiber internal and matrix-fiber external interfaces, respectively. The slip *s* is computed using Eq. (17):

$$s = \int_0^y \varepsilon_{yy} dy \tag{110}$$

Figure 28 shows the idealized $\tau_{zy}^{j} - s^{j}$ curve that is valid for both the internal and external fiber-matrix interfaces. According to this relationship the shear stress increases until reaching the maximum bond shear stress $\tau_{zy,m}^{j}$ (ascending branch), after which the interface experiences a softening behavior. When the slip reaches the value s_f^j, debonding occurs. As the slip increases beyond s_f^j, friction between single fibers filaments and between matrix and fibers provides a constant value of the shear stress equal to $\tau_{zy,f}^{j}$.

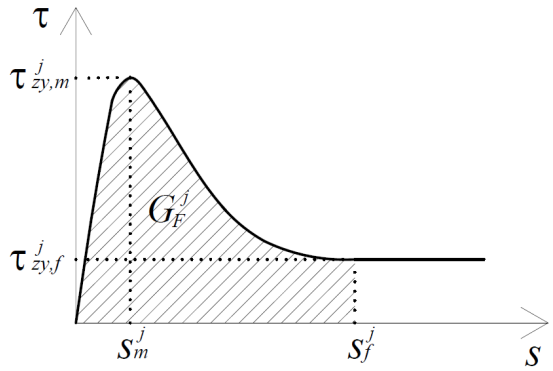

Figure 28. Idealized shear stress - slip curve.

Substituting Eq. (108) and Eq.(109) into Eq. (107), under the hypothesis of $y = l_{eff}$, the debonding load P_{deb} can be derived:

$$P_{deb} = b^* \sqrt{2Et^* \left(G_F^i + G_F^e\right)} \tag{111}$$

Eq. (111) represents the relationship between the debonding load and the fracture energies G_F^i and G_F^e in case of a single fiber bundle. Since there is no width effect related to the entire composite width, the debonding load corresponding to *n* fiber bundles can be obtained by multiplying the debonding load of a single fiber bundle by the number of bundles *n*.

3.12 Results of the fracture mechanics approach

As a first attempt to study the stress-transfer mechanism that characterizes FRCM composites, the macro-scale fracture mechanics approach used for FRP-concrete interfaces was extended to the matrix-fiber interface of FRCM composites. The

cohesive material law was obtained by combining the interfacial shear stress τ_{zy}^{j} with the corresponding slip s^{j} between the fibers and the matrix at the onset of the debonding process, i.e. point B in Figure 17a. The strain profiles of four different points located around point B of Figure 17a were considered, as discussed in §3.10.4. The free body diagram of an infinitesimal element of the fibers is depicted in Figure 27.

As previously stated, since the debonding occurs at the matrix-fiber interface, both the internal and external matrix-fiber interface behavior must be investigated. As a first attempt it will be assumed that the shear stresses at the internal and external interface are equal [39]. Consequently, the equilibrium condition yields:

$$\tau_{zy}^{i} = \tau_{zy}^{e} = \frac{1}{2} E t^{*} \frac{\mathrm{d}\varepsilon_{yy}}{\mathrm{d}y} \tag{112}$$

where E and t^{*} are the elastic modulus and the average thickness of the fibers, respectively. It should be noted that Eq. (112) is valid if: (i) a pure Mode-II loading condition is considered; (ii) the fiber strip is considered homogeneous and linear elastic until failure; and (iii) the thickness and width of the fibers is constant and variation along the length is neglected. If the concrete substrate is considered rigid and the deformation of the matrix layers is neglected, which is equivalaent to considering the matrix layers as rigid, Eq. (110) can be used to compute the slip $s^{i} = s^{e} = s$, between the fibers and the matrix, from the integration of the axial strain ε_{yy} measured along the bonded length. The area under the curves $\tau_{zy}^{i} - s$ and $\tau_{zy}^{e} - s$ provides the value of the fracture energies of matrix-fiber internal interfaces (G_F^{i}) and external interface (G_F^{e}):

$$G_F = G_F^{i} = G_F^{e} = \int_0^{s_f} \tau_{zy}^{i} \mathrm{d}s = \int_0^{s_f} \tau_{zy}^{e} \mathrm{d}s \tag{113}$$

where $s_f = s_f^{i} = s_f^{e}$ is the slip corresponding to the complete debonding of the fibers from the matrix (Figure 28). Eq. (113) implicitly entails that the slip between fibers and the two layers of matrix at the internal and external interfaces is the same, which is consistent with the assumption that the deformation of the matrix layers is negligible. In addition, Eq. (113) entails that failure occurs simultaneously at interfaces *i* and *e*. The fracture energy G_F of Eq. (113) should be interpreted as an *average* energy. In fact, the strain of the fiber filaments varies within the fiber bundle, and strain gauge readings are averaged across the bundle [16, 56]. In addition, the macro-scale approach presented in this section does not capture the complex phenomenon at the matrix-fiber interface where core filaments have a different degree of bond due to the limited impregnation by the matrix [16, 56].

Figure 28 shows the idealized $\tau_{zy}^{j} - s$ relationship which corresponds to the strain profiles of Figure 26a. The fracture energy is the area under the curve in the range $0 < s < s_f$, without including friction [16].

Since the strain was measured at a limited number of points along the central bundle of the fiber strip, the accuracy of the $\tau_{zy}^{j} - s$ relationship and the fracture energy $G_F = G_F^i = G_F^e$ is affected by the procedure chosen to obtain the cohesive material law. In order to obtain a reliable value of the fracture parameters, as previously discussed, four points around point B (Figure 17a) were considered. In addition, two different procedures were utilized to obtain the cohesive material law and the associated fracture energy. The first procedure used the derivation and integration of the fitting function ε_{yy} (see Figure 26b) provided in Eq. (93) to compute the shear stress τ_{zy}^{j} and the slip s. The second procedure consisted of the direct estimation of the derivative and integration of the strain profile in a discrete manner [89]:

$$\tau_{zy}^{j}(y_p) = \frac{1}{4} t^* E\left[\left(\varepsilon_{p-1} - \varepsilon_p\right)/\left(y_{p-1} - y_p\right) + \left(\varepsilon_p - \varepsilon_{p+1}\right)/\left(y_p - y_{p+1}\right)\right] \tag{114}$$

$$s(y_p) = \sum_{q=p}^{N} \frac{1}{2}\left(\varepsilon_q + \varepsilon_{q+1}\right)\left(y_q - y_{q+1}\right) \tag{115}$$

where y_p is the *p*-th strain gauge position, ε_p is the corresponding *p*-th strain gauge measurement, and $N = 9$ for $\ell = 330$ mm, except for specimen DS_330_60_S_3 which has $N = 10$, or $N = 12$ for $\ell = 450$ mm (Figure 19).

Figure 29 shows the corresponding $\tau_{zy}^{j} - s$ curves obtained from the fitting (*fit*) and discrete (*dis*) procedures for points I5 and M5 of the load response of DS_330_43_S_5 depicted in Figure 25a. The discrete $\tau_{zy}^{j} - s$ curves are affected by the limited number of points at which the axial strain was measured, and thus they differ from the fitting curves. The average values of the fracture energies obtained from the fitting (G_F^{fit}) and discrete (G_F^{dis}) procedures are reported in Table 5 for each specimen instrumented with strain gauges. The average values of G_F^{fit} and G_F^{dis} for each test were calculated from the same four points around point B used to determine the effective bond length l_{eff}.

The load-carrying capacity associated with initiation of debonding (point B) is related to the fracture energy according to Eq. (111):

$$\overline{P}_{deb} = nb^* \sqrt{4Et^* G_F} = nb^* \sqrt{4Et^* G_F^i} = nb^* \sqrt{4Et^* G_F^e} \tag{116}$$

Eq. (116) is valid if a pure Mode-II interfacial loading condition occurs across the entire width and if $\tau_{zy}^{i} = \tau_{zy}^{e}$ holds (see Eq. (112)). As discussed in §3.9, although within the single bundle of fibers it is possible to recognize a width effect, a global width effect does not appear to exist for the entire width of the composite (Figure 18). Hence Eq. (116) can be used to compute the load-carrying capacity associated with initiation of debonding [25, 73]. Note that Eq. (116) does not include friction, therefore $\overline{P}_{deb} \neq P^*$.

The values of $\overline{P}_{deb}$ calculated from the fracture energies G_F^{fit} and G_F^{dis} obtained from the two procedures previously described are indicated as $\overline{P}_{deb}^{fit}$ and $\overline{P}_{deb}^{dis}$, respectively.
The average value of the experimental loads corresponding to the four points within the range $(P_1 - P_2)$ used to determine the fracture energies is taken as P_{deb}^{exp}, which is also identified as the applied load at point B in Figure 17a. The values of P_{deb}^{exp} are provided in Table 5.
The load corresponding to the onset of debonding can also be obtained from Eq. (117):

$$\overline{\overline{P}}_{deb} = \overline{\varepsilon}_{yy} n b^* t^* E \tag{117}$$

where $\overline{\varepsilon}_{yy}$, provided in Table 5 for each test, is the average of the strains measured (not fitted) by gauge 4 for the four selected points in the range $(P_1 - P_2)$ around point B (see Figure 17a).

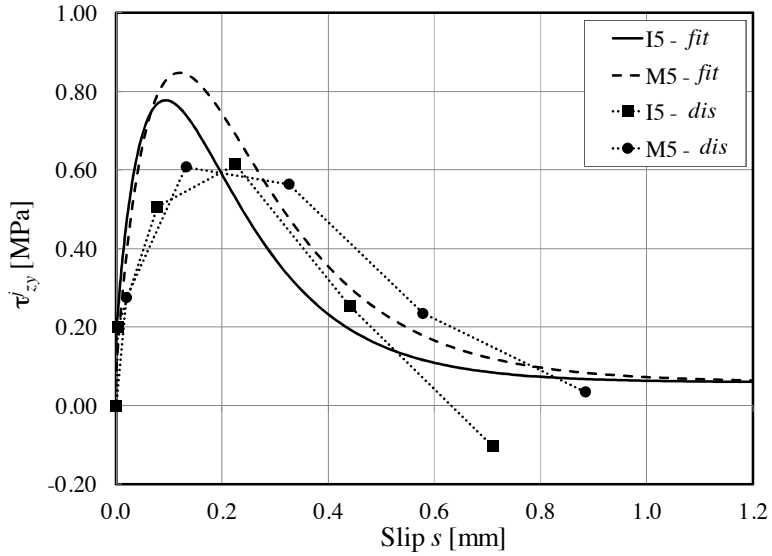

Figure 29. Shear stress τ_{zy}^{j} vs. slip s curves for points I5 and M5 of specimen DS_330_43_S_5.

Figure 30 compares the experimental values of P_{exp}^{deb} with the values of the load $\overline{\overline{P}}_{deb}$, $\overline{P}_{deb}^{fit}$, and $\overline{P}_{deb}^{dis}$, for each specimen instrumented with strain gauges. It should be noted that the values of $\overline{P}_{deb}^{fit}$, and $\overline{P}_{deb}^{dis}$ presented in Figure 30 are determined using the corresponding average value of the fracture energies provided in Table 5. In general, a good agreement between the average measured load (P_{deb}) and the three values obtained from Eqs. (116) and (117) is observed. Nevertheless, the following factors should be taken into account: (i) for FRCM composites due to the discrete pattern of the bundles, there could be a non-uniform load distribution across the width. For this reason the strain measured in the central bundle of the fiber net may not be the strain at

debonding corresponding to the entire applied load, thus leading to a scatter between the load calculated with Eqs. (116) and (117) and the corresponding applied load P_{exp}^{deb}. (ii) The loads P_{exp}^{deb}, $\overline{\overline{P}}_{deb}$, $\overline{P}_{deb}^{fit}$, and $\overline{P}_{deb}^{dis}$ are obtained from points in the load response around the assumed position of point B. However the exact position of point B is unknown.

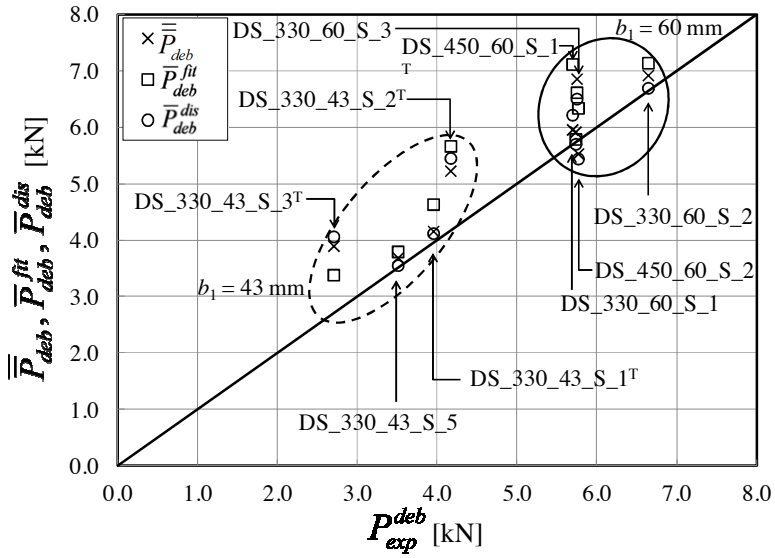

Figure 30. Comparison between the average measured load (P_{exp}^{deb}) and the values obtained from Eqs. (116) and (117).

It should be noted that if $\ell > l_{eff}$ the values of P_{exp}^{deb}, $\overline{\overline{P}}_{deb}$, $\overline{P}_{deb}^{fit}$, and $\overline{P}_{deb}^{dis}$ should vary with the bonded width b_1 but not with the bonded length ℓ because they represent the applied load related to bond and do not include friction. However, the loads in Figure 30 corresponding to specimens with a bonded width equal to 43 mm or 60 mm are quite scattered. The scatter can be justified by the fact that the load at point B is influenced by the bond quality, which is strongly dependent of the matrix impregnation of the fibers and was not controlled.

For FRP-concrete joints, Chen and Teng [32] proposed a design formula to compute the axial strain corresponding to the load-carrying capacity of the interface when debonding occurs:

$$\overline{\varepsilon}_{yy}^{FRP} = 0.427\beta_L\beta_p\sqrt{\frac{\sqrt{f_c'}}{E_f t_f}} \tag{118}$$

where $\beta_L = 1$ if the bonded length of FRP is greater than the effective bond length. β_p takes into account the effect of the width ratio of the bonded strip to the concrete block [32]. t_f is the nominal thickness of one ply of FRP reinforcement in mm, E_f is the

tensile modulus of elasticity in MPa, and f_c' is the specified compressive strength of concrete in MPa. Similar formulas for the FRP-concrete interface were introduced by several research groups and adopted by international guidelines [6, §1]. The strain at debonding computed with Eq. (118) is lower than the values of $\bar{\varepsilon}_{yy}$ provided in Table 5. As the concrete blocks had two different average compressive strengths, for the shorter blocks (L=375 mm) Eq. (118) provides a value of 7920 με, whereas for the longer blocks (L=510 mm) it provides a value of 7460 με. The value of β_p was taken as 1 since a global width effect was not observed, and the value of β_L was taken as 1 since a bonded length greater than 255 mm was considered. It should be noted that Eq. (118) provides a value of the strain at debonding that depends on the compressive strength of concrete. Results presented in this study indicate that Eq. (118) is not applicable to FRCM-concrete joints if debonding occurs at the matrix-fiber interface.

3.13 Effective bond length

Figure 31a shows the idealized $\sigma^* - \ell$ relation for FRCM-concrete joints obtained from the experimental results. The dashed line in Figure 31a shows the $\sigma^* - \ell$ relation for FRP-concrete joints when $\ell > l_{eff}$. The ultimate stress increases linearly for bonded lengths greater than l_{eff} due to the contribution of friction. Figure 31b shows the average of the ultimate stress σ^* for each bonded width tested as a function of the bonded length ℓ for the tests herein presented. Three different bonded widths, namely 34 mm, 60 mm, and 80 mm, corresponding to 4, 7, and 9 bundles, respectively, are considered. The results of the double-lap shear tests published by D'Ambrisi et al. [42] are included for comparison in terms of the average of the ultimate stress σ^* for each bonded width. The results of Figure 31b resemble the idealized curve of Figure 31a and show that the ultimate stress σ^* increases as the bonded length ℓ increases up to a value equal to 450 mm. As such, Figure 31b cannot be used to determine l_{eff} because for $\ell > l_{eff}$, the peak load P^* (and consequently σ^*), as described in Eq. (92), is due to the load associated with both bond and friction. Instead, the effective bond length for FRCM composites should be determined from the strain profiles by considering, for example, points of the load response at the onset of the debonding process as outlined in this paper.

Figure 31b shows that the average ultimate stress σ^* of specimens with a bonded length of 450 mm is slightly larger than the average ultimate stress σ^* of specimens with a bonded length of 330 mm. The corresponding increase in the ultimate stress $\Delta\sigma^*$ can be calculated by considering the increase in the bonded length ($\Delta\ell$) and the consequent increase of the load carried by friction (Figure 31a):

$$\Delta\sigma^* = \frac{2\tau_f \Delta\ell}{t^*} \tag{119}$$

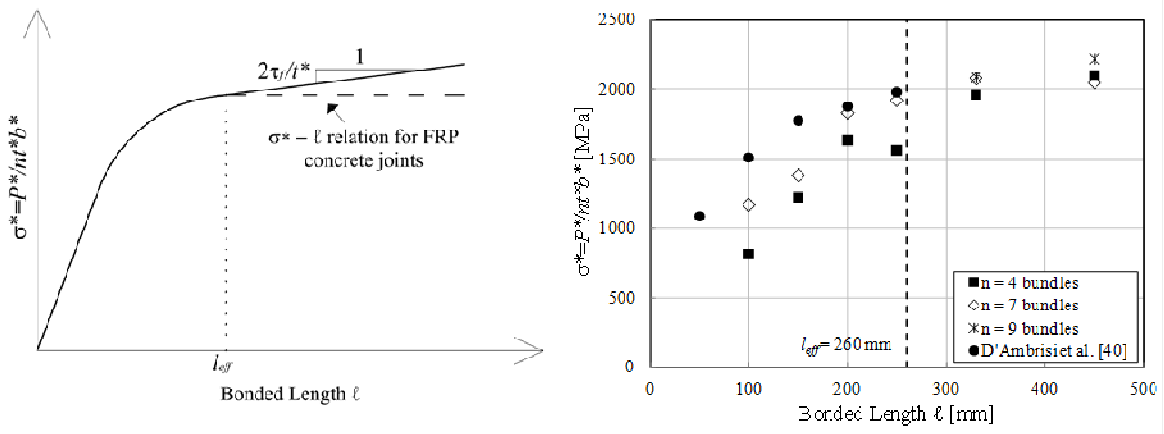

a. b.

Figure 31. a) Idealized ultimate stress σ^* vs. bonded length ℓ curve. b) Variation of the ultimate stress σ^* as a function of the bonded length ℓ.

The value of $\Delta\sigma^*$ obtained from Eq. (119) is independent of the number of bundles n. Comparing specimens with a bonded length of 450 mm and those with a bonded length of 330 mm ($\Delta\ell$ = 120 mm), Eq. (119) provides a value of $\Delta\sigma^*$ that is consistent with the difference in the average values of σ^* reported in Figure 31b for ℓ = 330 mm and ℓ = 450 mm. It should be noted, however, that the average values for specimens with 7 bundles and bonded length ℓ = 330 mm and ℓ = 450 mm were very similar.

The effective bond length for the FRP-concrete interface is calculated by [32]:

$$l_e = \sqrt{\frac{n_f t_f E_f}{\sqrt{f_c'}}} \tag{120}$$

where n_f is the number of plies of FRP reinforcement, t_f is the nominal thickness of one ply of FRP reinforcement in mm, E_f is the tensile modulus of elasticity in MPa, and f_c' is the specified compressive strength of concrete in MPa. Eq. (120) provides a value of the effective bond length of 54 mm for the shorter blocks (L=375 mm) and of 57 mm for the longer blocks (L=510 mm). A formula similar to Eq. (120) was used by Ombres [79] to calculate the effective bond length of the FRCM external reinforcement used to strengthen RC beams. Using this approach, however, the computed effective length in [79] was found to be significantly underestimated. The present study confirms that Eq. (120) should not be used for FRCM composites if the debonding process occurs at the matrix-fiber interface.

It should be noted that the thickness of the fibers used by the authors in Eqs. (118) and

(120) is equal to t^*. However, the equivalent thickness of the fibers (0.046 [79, 93]), obtained by considering the fibers evenly distributed over the width of the composite, could be used.

3.14 Conclusions

This chapter describes the results of experimental research conducted to study the stress-transfer mechanism at the matrix-fiber interface of fiber reinforced cementitious matrix (FRCM) composites externally bonded to a concrete substrate.
Based on the results of this study, the following conclusions can be made:

1. Debonding occurred at the matrix-fiber interface rather than at the matrix-concrete interface. This is a unique aspect of FRCM composite which indicates that the substrate might not play an important role in the debonding mechanism of this composite. As a consequence, existing formulas included in guidelines used to design FRP strengthening systems cannot be used for FRCM composites due to the different failure modes. Additional studies are necessary to understand the role of the concrete surface treatment and its mechanical properties on the debonding mechanism.
2. Unlike with FRP-concrete joints, a *global* width effect was not observed with FRCM-concrete joints in terms of the ultimate stress σ^*. This may be due to the independent action of the longitudinal fiber bundles. However it was recognized that a width effect exists within a single fiber bundle due to the different impregnation of the fibers by the matrix.
3. The load responses showed that after debonding of the fibers from the two layers of matrix occurred, friction contributed to the increase of the applied load. Consequently, the ultimate stress vs. bonded length plot could not be used to determine the effective bond length l_{eff}.
4. Nine specimens, presented in this chapter, were instrumented with strain gauges along the bonded length to study the stress-transfer mechanism and evaluate l_{eff}. It was noticed that the presence of friction altered the strain profile after the onset of debonding. An effective bond length l_{eff} due to bond could be determined from the strain profiles at the onset of debonding. The average l_{eff} was estimated to be 260 mm.

4 BOND BEHAVIOR OF THE INTERNAL AND EXTERNAL MATRIX LAYER IN PBO FRCM-CONCRETE JOINTS

4.1 Abstract

Fiber reinforced cementitious matrix (FRCM) composites represent a newly-developed promising technique for strengthening reinforced concrete (RC) structures. FRCM composites are comprised of high strength fibers applied to the concrete substrate through an inorganic cementitious matrix. A first internal layer of matrix is used to bond the fiber to the concrete substrate whereas a second external layer of matrix is used to protect the fiber and improve the bond between fibers and matrix. The weakness of FRCM-concrete joints has been reported to be at the matrix-fiber interfaces, and the debonding is characterized by large slip of the fibers within the surrounding matrix. In this chapter the experimental tests of FRCM-concrete joints without the external matrix layer will be shown and discussed. Results of specimens with the external matrix layer are compared with the results of specimens without the external matrix layer to analyze the bond behavior of the two matrix-fiber interfaces. The stress-transfer mechanism between the fiber filaments and the matrix layers is studied by means of a fracture mechanics approach. The shear stress-slip relationships that characterize the matrix-fiber interfaces are determined experimentally and used to compute the load corresponding to debonding failure. Furthermore, different simplified shear stress-slip relationships are proposed to describe the bond behavior of the different matrix-fiber interfaces.

4.2 Introduction

Promising newly-developed composite materials to strengthen RC structures are represented by the so-called FRCM (fiber reinforced cementitious matrix) composites. The literature regarding FRCM composites is still very limited, and a comprehensive study of the stress-transfer mechanism in FRCM-concrete joints is not available.
In the previous chapter (§1) the stress-transfer mechanism between the fibers and the surrounding matrix has been studied using a fracture mechanics approach [16, 56] assuming that the shear stress transferred from the embedded fibers to the two matrix-fiber interfaces is approximately equal [39]. The main objective of this paper is to investigate the stress-transfer mechanism at the matrix-fiber interface on either side of the fiber net, and examine the role of each of the two different interfaces. The macro-

scale fracture mechanics approach used to describe the stress-transfer mechanism of FRP-concrete joints (§1.6) is extended to the case of FRCM-concrete joints. Different simplified shear stress-slip relationships are used to describe the bond behavior of the two matrix-fiber interfaces. The analytical models proposed are based on the results obtained from an extensive experimental campaign on FRCM-concrete joints tested using single-lap direct-shear set-up presented herein.
The research described in this chapter sheds light on the interfacial behavior between matrix and fibers in FRCM composites, the study of which is necessary for the development and validation of models to determine the load-carrying capacity of FRCM-concrete joints.

4.3 Approach adopted in this chapter

The overarching goal of this chapter is to study the role of the internal and external layer of matrix in the stress-transfer mechanism. In §4.4 and §4.6 the experimental work carried out is briefly described. In §4.7 the characteristics of the idealized load response for the single-lap direct-shear tests are discussed. In §4.9 the macro-scale fracture mechanics approach used for the FRP-concrete interface (§1.6), applied in the previous chapter on specimens with both the internal and external matrix layer under the hypotheses that the concrete substrate and the mortar layers are rigid (§3.11), is extended to the matrix-fiber interface of FRCM-concrete joints without the external matrix layer. The strain along the fiber bundle is approximated via Eq. (121) and used to obtain the interfacial shear stress and the slip via Eqs. (125) and (126), respectively. The results presented in the previous chapter (§3.12) were based on the fracture mechanics approach presented in §3.11 and under the hypotheses that the matrix-fiber internal layer and matrix-fiber external layer interface have the same behavior. This last assumption will be removed in §4.11 and §4.13. In §4.10 the load distribution among fiber bundles is discussed. Those specimens that experienced a non-uniform distribution of the force among the fiber bundles are disregarded in the following sections in which the fracture mechanics approach is used again without the assumption that the two interfaces have the same behavior. Specimens with a non-uniform load distribution are not considered reliable because the debonding force is not representative of all the bundles. In §4.11 a comparison between specimens with and without the external layer of matrix is carried out in terms of the debonding load for those specimens that did experience a limited load redistribution based on the results of §4.10. The comparison is based on the assumption that the stress transfer between the internal layer of matrix and the fibers is the same independently of the presence of the external layer of matrix. The comparison allows for understanding the role of the matrix layers in the stress transfer. In §4.12 the role of the transversal bundles is discussed in order to understand whether the force transferred between the fiber filaments and the two layers of matrix is related to the position of the transversal bundles, which could interrupt the bond. Finally, in

§4.13 the different role of the matrix layers in the stress transfer is expressed in terms of the two cohesive material laws for the fiber-internal layer and fiber-external layer interface. A simplified cohesive material law is adopted. The results presented in §4.9 are employed in §4.13. The fracture parameters of the fiber-internal layer interface are derived from those specimens without the external layer of matrix. Under the assumption that the internal matrix layer has the same behavior independently of the presence of the external layer of matrix, the results of §4.11 are used to determine the fracture parameters of the fiber-external layer interface. Three different models of cohesive law for the fiber-external layer interface are discussed.

4.4 Experimental tests

The bond behavior of FRCM-concrete joints was studied through an extensive experimental campaign, which was partially reported in the previous chapter (§3.3). Further results are presented in this chapter. The classical push-pull single-lap (direct) shear test set-up [25, 98, 99] was adopted to study the stress-transfer mechanism between the FRCM composite and the concrete substrate (Figure 32). The direct-shear test set-up adopted was described in the previous chapter (§3.3) and is briefly recalled here for the sake of clarity.

The composite material was comprised of one layer of bidirectional polyparaphenylene benzobisoxazole (PBO) fiber net applied to the concrete substrate by means of a 4 mm-thick (internal) layer of a polymer-modified cementitious matrix [93]. Detailed characteristics of the PBO fibers, cementitious matrix, and concrete used are reported in the previous chapter (§3.4). The matrix was applied only in the bonded area to bond the composite to the concrete substrate and to embed the fibers (Figure 32). For some specimens an additional external layer of matrix was applied over the PBO fiber net, while the fibers were left uncovered for others. The bonded width (b_1) and length (ℓ) of the composite were varied. Two linear variable displacement transducers (LVDTs), mounted on the concrete surface close to the lateral edges of the composite at the beginning of the bonded area, reacted off of a thin aluminum Ω-shaped bent plate attached to the PBO transversal fiber bundle (Figure 32). The average of the two LVDT measurements, defined as the global slip g, was used to control the tests which were conducted in displacement control by increasing the global slip g at a rate equal to 0.00084 mm/s. Additional details on the test set-up can be found in the previous chapter (§3.3).

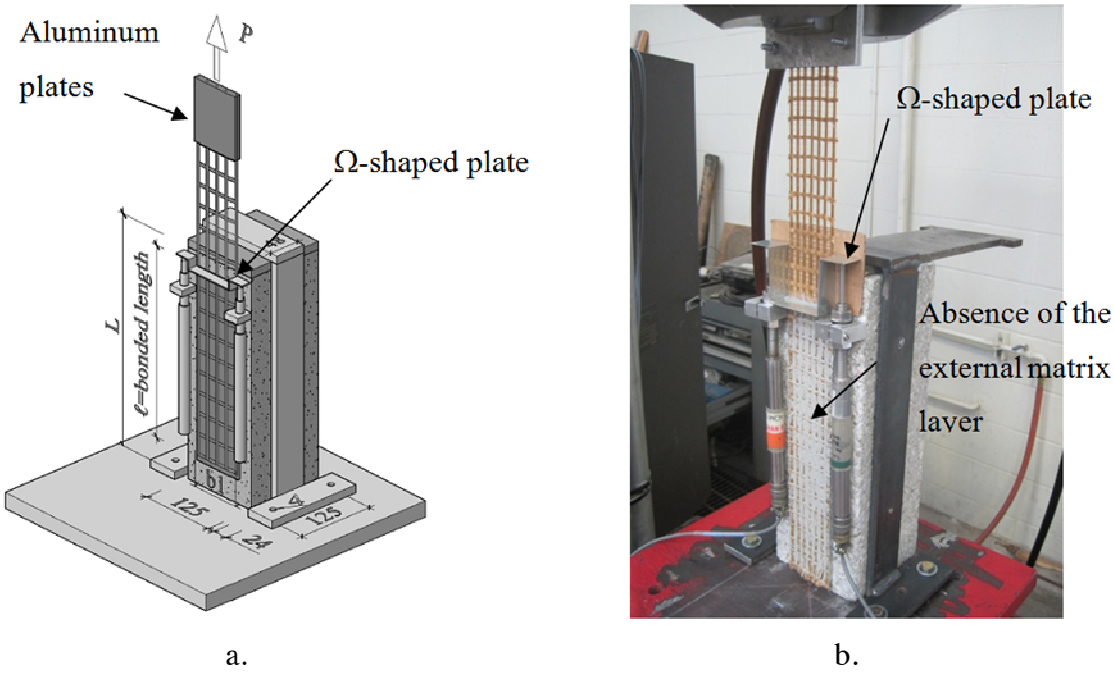

a. b.

Figure 32. a) Single-lap direct-shear test set-up. b) Photo of specimen DS_330_60_L_D_1.

4.5 Note on the notation adopted in this chapter

In this chapter the behavior of FRCM-concrete joints with and without the external layer of the inorganic matrix is investigated. A subscript *L* is added to the variables (such as the applied load, the fracture energy, etc.) that refer to the specimens without the external matrix layer. For specimens with two layers of matrix, the parameters that refer to the internal-layer and external-layer matrix-fiber interfaces are indicated with a superscript *i* and *e*, respectively. It should be remarked that the interface characteristics between the internal layer of matrix and the fibers may vary whether the external layer is present or not. For this reason, the parameters referring to the internal matrix layer are indicated with a subscript *L* when referring to specimens without the external matrix, and are indicated with a superscript *i* when referring to specimens with both the internal and external matrix layers. The global slip *g* was increased at the same constant rate independently of the type of specimen; therefore it is always indicated without the subscript *L*.

4.6 Specimens without the external matrix layer tested

In addition to the specimens reported in §1, twenty-eight single-lap direct-shear tests with different bonded lengths, bonded widths, and without the external layer of matrix were tested. In order to investigate the role of the internal and external layer of matrix,

the results of specimens without the external matrix layer were compared with the results of specimens with the external matrix layer. Table 6 reports the name and corresponding peak load (P^* or P_L^*) for all specimens considered in the analysis presented in this chapter.

Table 6. Single-lap direct-shear specimens with and without the external layer of matrix.

Specimen	P^* or P_L^* [kN]	$\surd = \Delta < \bar{s}_f$ $\times = \Delta \geq \bar{s}_f$	Specimen	P^* or P_L^* [kN]	$\surd = \Delta < \bar{s}_f$ $\times = \Delta \geq \bar{s}_f$
DS_330_43_L_1^T	4.96	×	DS_330_43_S_1^T	4.48	×
DS_330_43_L_2	4.63	√	DS_330_43_S_2^T	5.12	×
DS_330_43_L_3	4.61	√	DS_330_43_S_3^T	3.03	×
DS_330_43_L_4	3.98	√	DS_330_43_S_5	4.03	×
DS_330_43_L_5	3.96	√	DS_330_60_1^T	7.05	×
DS_330_43_L_6	3.82	√	DS_330_60_2^T	6.56	×
DS_330_43_L_7^T	2.67	×	DS_330_60_3^T	6.06	×
DS_330_43_L_8^T	3.67	×	DS_330_60_4^T	6.50	×
DS_330_43_L_9^T	3.09	×	DS_330_60_5^T	6.28	×
DS_330_43_L_10	4.45	×	DS_330_60_6	7.01	×
DS_330_43_L_11	4.72	√	DS_330_60_D_1	8.29	×
DS_330_43_L_S_1^T	3.24	×	DS_330_60_D_2	7.12	√
DS_330_43_L_S_2	4.69	√	DS_330_60_D_3	6.56	√
DS_330_60_L_1	5.80	√	DS_330_60_D_4	5.24	√
DS_330_60_L_2	5.49	√	DS_330_60_D_5	6.69	√
DS_330_60_L_3	6.60	√	DS_330_60_S_1	6.30	×
DS_330_60_L_4	5.46	√	DS_330_60_S_2	7.31	√
DS_330_60_L_5	5.26	√	DS_330_60_S_3	6.55	√
DS_330_60_L_D_1	5.19	√	DS_330_60_T_1	6.62	√
DS_330_60_L_D_2	6.13	√	DS_330_60_T_2	6.27	√
DS_330_60_L_D_3	5.47	√	DS_330_60_T_3	6.59	√
DS_330_60_L_D_4	4.90	√	DS_450_60_1	6.40	√
DS_330_60_L_S_1	5.97	√	DS_450_60_2	6.34	√
DS_450_60_L_1	6.90	√	DS_450_60_3	6.44	×
DS_450_60_L_2	5.96	×	DS_450_60_4	5.77	√
DS_450_60_L_3	6.43	×	DS_450_60_5	6.51	√
DS_450_60_L_4	6.23	×	DS_450_60_6	6.79	√
DS_450_60_L_5	6.91	√	DS_450_60_7	6.65	√
DS_330_43_1	4.43	×	DS_450_60_D_1	7.01	√
DS_330_43_2	5.25	√	DS_450_60_D_2	6.67	√
DS_330_43_3	5.27	√	DS_450_60_D_3	7.33	√
DS_330_43_5	4.79	×	DS_450_60_S_1	6.63	√
DS_330_43_6	5.09	√	DS_450_60_S_2	6.86	√

The notation adopted for the specimen names is analogous to the notation adopted in the previous chapter (§3.5) and is recalled here for the sake of clarity. The direct shear test specimens were named following the notation DS_X_Y_L_S_D_T_Z^T, where X=bonded length (ℓ) in mm, Y=bonded width (b_1) in mm, L (if present) indicates the absence of the external matrix layer, S (if present) indicates the presence of strain gauges mounted on the fiber net, D (if present) denotes that the specimen was tested until a constant load at the end of the test was measured, T (if present) indicates that the transversal bundles were removed before applying the matrix, and Z=specimen number. A superscript T after Z (if present) indicates that the fiber net was oriented with the transversal fiber bundles directly against the matrix internal layer.

4.7 Load response of PBO FRCM-concrete joints

The PBO FRCM-concrete specimens mostly failed due to debonding of the fiber net from the embedding matrix (§3.7). The debonding was characterized by increasing slip at the matrix-fiber interfaces and by the presence of friction for the portion of the bonded length where the fibers were debonded. It should be noted that two different friction contributions can be distinguished, namely friction between fiber filaments and friction between fibers and matrix (§3.8)

The evidences obtained through the single-lap tests, together with the results present in the literature [3,13], allowed to propose an idealized applied load – global slip curve (§3.8), which is reported in Figure 17a. The idealized applied load – global slip curve is representative of specimens with and without the external layer of matrix. For the sake of brevity, the curve is shown in Figure 17a for specimens with the external matrix layer (applied load P), whereas is omitted for specimens withou the external matrix layer (applied load P_L).

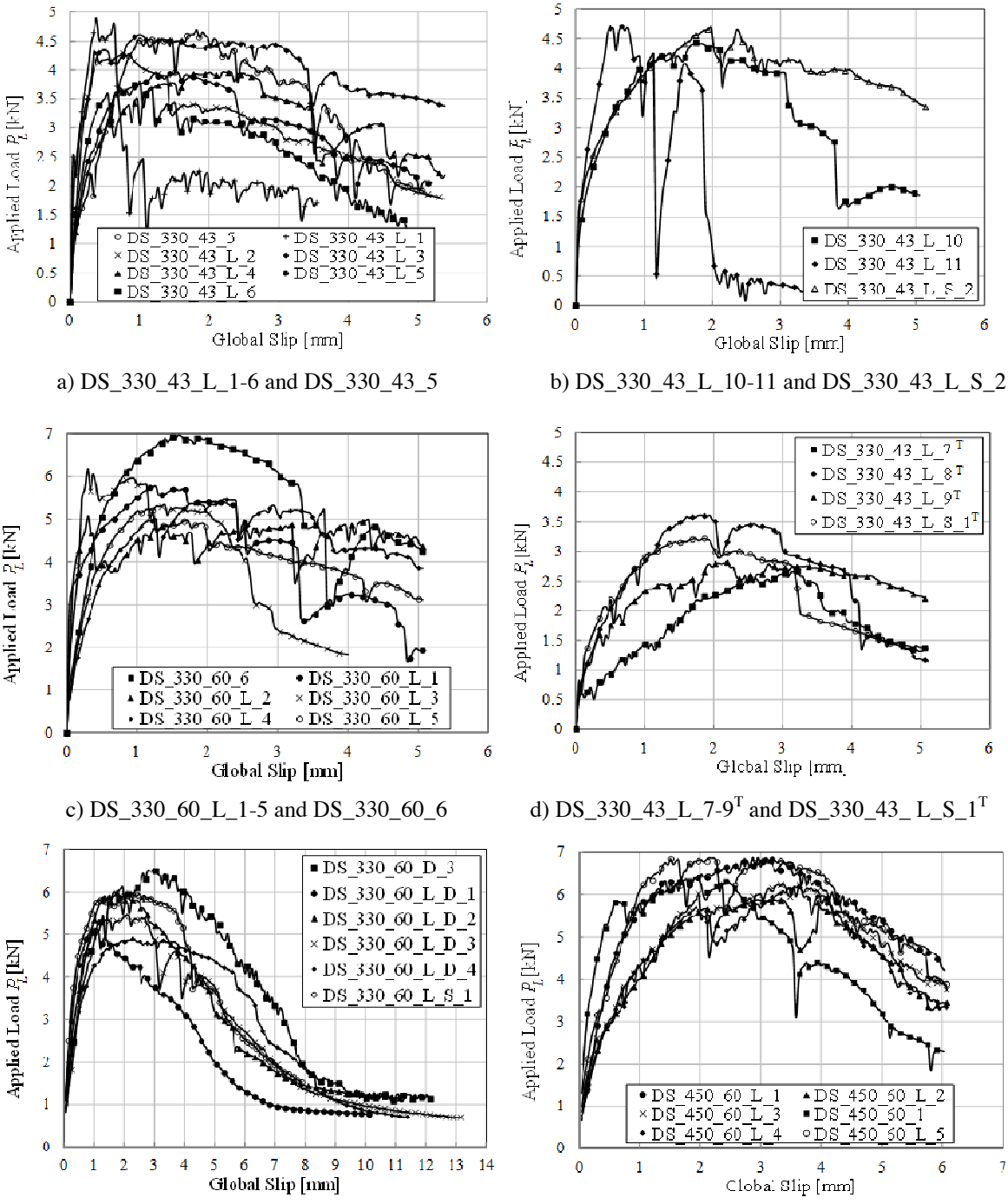

a) DS_330_43_L_1-6 and DS_330_43_5

b) DS_330_43_L_10-11 and DS_330_43_L_S_2

c) DS_330_60_L_1-5 and DS_330_60_6

d) DS_330_43_L_7-9^T and DS_330_43_ L_S_1^T

e) DS_330_60_L_D_1-4, DS_330_60_D_3, and DS_330_60_L_S_1

f) DS_450_60_L_1-5 and DS_450_60_1

Figure 33. $P_L - g$ responses for specimens without the external layer of matrix.

The load responses of specimens without the external layer of matrix are plotted in Figure 33. Figure 33a and Figure 33b show the response of the specimens with bonded width b_1 = 43 mm with the fiber net oriented with the longitudinal bundles cast against

the internal layer of matrix. Figure 33a**,** which also includes the response of specimen DS_330_43_5 for comparison, shows that the shape of the applied load – global slip relation does not appear to be affected by the absence of the external matrix layer. Likewise Figure 33c shows that the response of the specimens with a bonded width b_1 = 60 mm and without the external layer of matrix is similar to that of specimen DS_330_60_6 with the external layer, also shown in the figure for comparison. This suggests that the nature of the stress-transfer mechanism is preserved. Figure 33d shows the response of specimens with bonded width b_1 = 43 mm, without the external layer of matrix, and the fiber net oriented with the transversal bundles cast against the internal layer of matrix. Comparison of Figure 33a and Figure 33d indicates that specimens in the DS_330_XX_L series with the fiber net oriented with the transversal bundles cast against the internal layer of matrix have a lower maximum load and stiffness. Figure 33e shows the load responses of specimens with b_1 = 60 mm that were tested until the applied load reached the constant value $P_{f,L}$ corresponding to pure friction. Specimens DS_330_60_L_S_1, which was tested until a global slip of approximately 8 mm was reached, is also included in Figure 33e. Specimen DS_330_60_D_3 and was added to Figure 33e for comparison. For specimens included in the DS_330_60_L_D Series (Figure 33e) the applied load, after reaching the value corresponding to $P_{f,L}$, slowly decreased because the absence of the external matrix layer might have induced a Mode-I component (peeling) that reduced the friction between the fibers and the matrix (see also Figure 40a). The load responses of specimens with a bonded length ℓ = 450 mm, bonded width b_1 = 60 mm, and without the external matrix layer are reported in Figure 33f. Figure 33f, which also includes specimen DS_450_60_1 for comparison, shows that the response of specimens without the external matrix layer is very close to the response of specimens with both the internal and external matrix layer. A detailed investigation of the role of the internal and external matrix layer is provided in the following sections.

4.8 Strain analysis of specimens without the external matrix layer

Strain gauges were applied directly on the fiber bundles to capture the distribution of the axial strain along the direction of the applied load. Three specimens without the external matrix layer were instrumented with strain gauges applied to the central fiber bundle according to the position reported in Figure 34. For specimen DS_330_60_L_S_1 the number and position of the strain gauges were varied to better capture the entire strain profile along the composite strip. The load response of the specimens equipped with strain gauges, namely specimen DS_330_43_L_S_1^T, DS_330_43_L_S_2, and DS_330_60_L_S_1, are depicted in Figure 33d, Figure 33b, and Figure 33e, respectively.

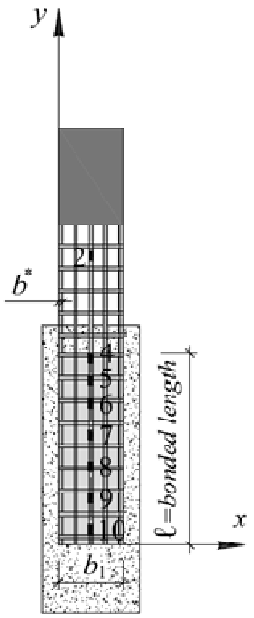

DS_330_43_L_S_1 DS_330_43_L_S_2	DS_330_60_L_S_1
y_2= 490 mm	y_2 = 490 mm
y_4= 330 mm	y_4= 330 mm
y_5= 290 mm	y_5= 315mm
y_6= 260 mm	y_6= 295 mm
y_7= 220 mm	y_7= 280 mm
y_8= 160 mm	y_8= 225 mm
y_9= 50 mm	y_9= 175 mm
	y_{10}= 70 mm

Figure 34. Position of the strain gauges for specimens without the external matrix layer.

As explained in the previous chapter (§3.10.4), the strain profiles corresponding to four points of the load response located in a small region around the assumed position of the onset of debonding (point B in Figure 17a) were considered. The range of load that defines the small region around point B and the corresponding range of slip are named $\left(P_{1,L} - P_{2,L}\right)$ and $\left(g_1 - g_2\right)$, respectively. The strain profiles taken around point B were approximated using Eq. (121), which takes into account both the bonding and friction mechanism. For specimens without the external matrix layer, it holds:

$$\varepsilon_{yy,L} = \varepsilon_0 + \frac{\alpha + k_L y}{1 + e^{\frac{y - y_0}{\beta}}} \tag{121}$$

$$k_L = \frac{\tau_{f,L}}{E \cdot t^*} \tag{122}$$

ε_0, α, β, and y_0 were determined using nonlinear regression analysis of the measured strains. $\tau_{f,L}$ represents the shear stress associated with friction for specimens without the external layer of matrix and can be evaluated from the load response after point E (Figure 17a):

$$\tau_{f,L} = \frac{P_{f,L}}{nb^*\ell} \tag{123}$$

where $nb^*\ell$ is the nominal bonded area of one matrix-longitudinal fiber interface, while $P_{f,L}$ is the load value associated with friction between fibers and matrix.

The load response of specimen DS_330_43_L_S_2 is shown in Figure 35a. The strain profiles along the bonded length corresponding to the points indicated in Figure 35a are shown in Figure 35b. Points A2, B2, and C2 in Figure 35a correspond to points A, B, and C in Figure 17a, respectively. The vertical dashed lines in Figure 35b are numbered according to the corresponding gauges (Figure 19). Strain values from gauge 5 of specimen DS_330_43_L_S_2 are not reported in Figure 35b because after a thorough inspection the gauge 5 was found to be improperly glued to the fiber bundle.

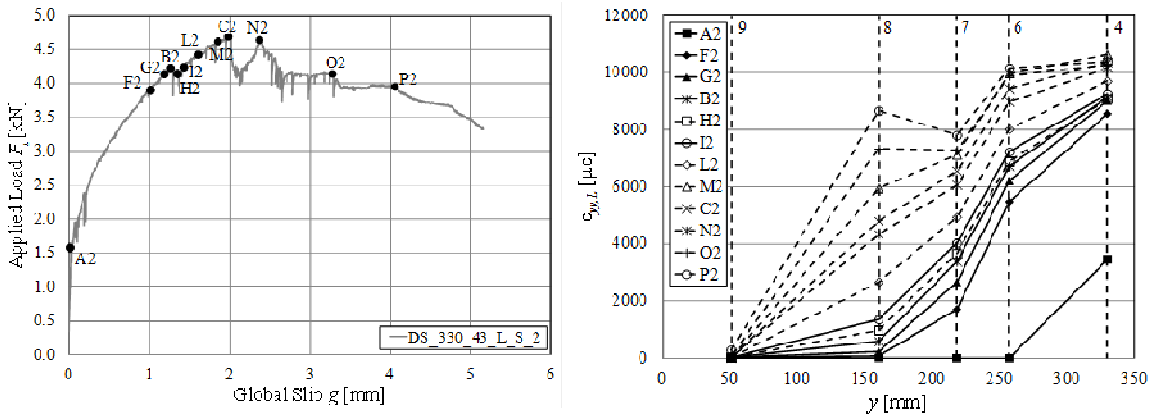

a. b.

Figure 35. a) Applied load P vs. global slip g plot for specimen DS_330_43_L_S_2. b) Axial strain $\varepsilon_{yy,L}$ profiles along the bonded length for representative points of specimen DS_330_43_L_S_2.

The strain distribution obtained by Eq. (121) follows an "S" shape with a value nominally equal to zero toward the free end and a linear increasing value where the fibers debonded from the matrix at the loaded end. The fitting curves (*fit*) obtained from Eq. (121), and corresponding to points H2 and I2 for specimen DS_330_43_L_S_2, are shown in Figure 36.

The effective bond length can be evaluated from the strain profiles along the bonded length by measuring the distance between the two points of the strain profiles in which the derivative is equal to zero at the free end and the derivative is constant at the loaded end (onset of the friction contribution). The average value of the effective bond length obtained from the four points within the small region around point B, the load range $\left(P_{1,L}, P_{2,L}\right)$, and the global slip range $\left(g_1, g_2\right)$ for each specimen equipped with strain gauges are reported in Table 7. The average value of the effective bond length $l_{eff,L}$ for the three specimens presented is 225 mm (CoV = 0.130). The value of the effective bond length $l_{eff,L}$ is affected by the limited number of specimens without the external matrix layer and equipped with strain gauges tested. It should be noted that the effective bond length $l_{eff,L} = 190$ mm of specimen DS_330_43_L_S_1^{T} is significantly shorter than the effective bond length of the other specimens equipped with strain gauges. This scatter between the values of $l_{eff,L}$ is attributed to the fact that the transversal fiber

bundles were placed against the internal matrix layer for specimen DS_330_43_L_S_1^{T}, whereas the longitudinal fiber bundles were placed against the internal matrix layer for specimens DS_330_43_L_S_2 and DS_330_60_L_S_1. Further analysis of the effect of the transversal bundles is reported in §4.12.

Table 7. Results obtained through the strain analysis and fracture mechanics approach for specimens without the external matrix layer instrumented with strain gauges.

Name	$l_{eff,L}$ [mm]	$(g_1 - g_2)$ [mm]	$(P_{1,L} - P_{2,L})$ [kN]	$P_{deb,L}^{exp}$ [kN]	$\bar{\varepsilon}_{yy,L}$ [με]	$G_{F,L}^{dis}$ [J/m^2]	$G_{F,L}^{fit}$ [J/m^2]
DS_330_43_L_S_1^{T}	190	(0.9, 1.0)	(2.75, 2.99)	2.86	5220	250	540
DS_330_43_L_S_2	250	(1.2, 1.4)	(4.13, 4.23)	4.18	9130	850	770
DS_330_60_L_S_1	230	(1.0, 1.4)	(5.67, 5.91)	5.80	10480	1000	960

The average value of the effective bond length obtained from specimens with and without the external matrix layer is $\bar{l}_{eff} = 250$ mm (CoV = 0.113). This result is confirmed by the analysis of the peak stress – bonded length relation $\sigma^* - \ell$ for FRCM-concrete joints obtained through the direct-shear tests of specimens with the external matrix layer and with different bonded lengths (Figure 31).

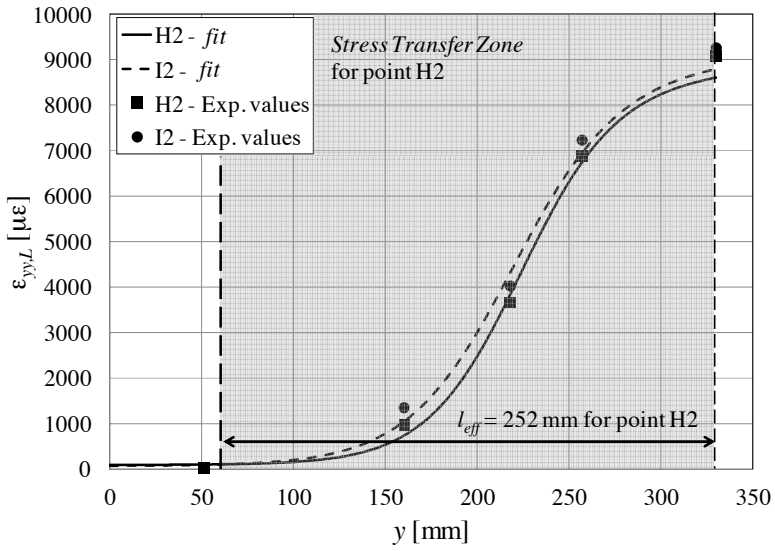

Figure 36. Fitting of the axial strain $\varepsilon_{yy,L}$ profiles for points H2 and I2 of specimen DS_330_43_L_S_2 (Figure 35a).

4.9 Fracture mechanics approach on specimens without the external layer of matrix

The fracture mechanics approach adopted for FRP-concrete joints [25, 69, §1.6] was employed in the previous chapter for the case of FRCM-concrete joints with both the internal and external layer of matrix (§3.11) assuming that the shear stress transferred from the embedded fibers to the two matrix-fiber interfaces is approximately equal [39]. The same fracture mechanics approach is extended in this chapter to FRCM-concrete specimens without the external matrix layer.

As a first attempt to apply a fracture mechanics approach to FRCM-concrete joints, the deformation of the matrix layers was neglected, and Eq. (124) was used to compute the debonding load:

$$P_{deb,L} = b^* \sqrt{2Et^* G_{F,L}} \tag{124}$$

For specimens without the external matrix layer, the $\tau_{zy,L} - s_L$ curve was obtained directly from the strain fitting (Eq. (121)) procedure applied to those specimens equipped with strain gauges and without the external layer of matrix, as per Eq. (125) and Eq. (126):

$$\tau_{zy,L} = Et^* \frac{\mathrm{d}\varepsilon_{yy,L}}{\mathrm{d}y} \tag{125}$$

$$s_L = \int_0^y \varepsilon_{yy,L}\, \mathrm{d}y \tag{126}$$

The fracture energy $G_{F,L}$ was then calculated by the integration of the $\tau_{zy,L} - s_L$ curve. The load-carrying capacity associated with initiation of debonding, $\overline{P}_{deb,L}^{fit}$, computed through the strain fitting of Eq. (121), is related to the fracture energy according to Eq. (124), which, for specimens without the external matrix layer, gives:

$$\overline{P}_{deb,L}^{fit} = nb^* \sqrt{2Et^* G_{F,L}} \tag{127}$$

Since a global width effect does not appear to exist for the entire width of the composite (§3.9), Eq. (127) can be used to compute the load-carrying capacity associated with initiation of debonding [25, 95].

As in case of specimens with the external layer of matrix (§3.12), two different procedures were used to obtain the cohesive material law and the associated fracture energy for specimens without the external layer of matrix. The first procedure used the derivation and integration of the fitting function $\varepsilon_{yy,L}$ provided in Eq. (121) to compute the shear stress $\tau_{zy,L}$ and the slip s_L. The second procedure consisted of the direct estimation of the derivative and integration of the strain profile in a discrete manner [89], as per Eq. (128) and Eq. (129):

$$\tau_{zy,L}(y_p) = \frac{1}{4} t^* E\left[\left(\varepsilon_{p-1} - \varepsilon_p\right)/\left(y_{p-1} - y_p\right) + \left(\varepsilon_p - \varepsilon_{p+1}\right)/\left(y_p - y_{p+1}\right)\right] \tag{128}$$

$$s_L(y_p) = \sum_{q=p}^{N} \frac{1}{2}\left(\varepsilon_q + \varepsilon_{q+1}\right)\left(y_q - y_{q+1}\right) \tag{129}$$

where $N = 9$ for specimen DS_330_43_L_S_1 and DS_330_43_L_S_2, and $N = 10$ for specimen DS_330_60_L_S_1 (Figure 34).

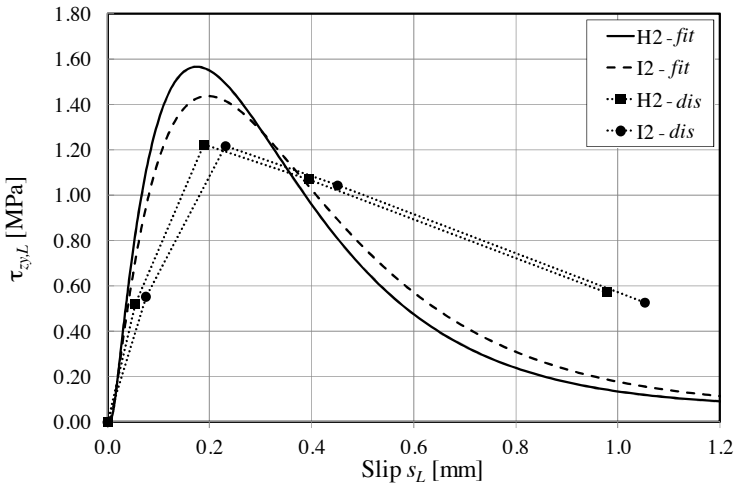

Figure 37. Shear stress $\tau_{zy,L}$ vs. slip s_L curves for points H2 and I2 of specimen DS_330_43_L_S_2.

Figure 37 shows the $\tau_{zy,L} - s_L$ curves obtained from the fitting (*fit*) and discrete (*dis*) procedures for points H2 and I2 of the load response of DS_330_43_L_S_2 depicted in Figure 35a. The discrete $\tau_{zy,L} - s_L$ curves differ from the fitting curves because they are affected by the limited number of points at which the axial strain was measured and by the absence of gauge 5, which was not properly glued to the fiber.

The average values of the fracture energies obtained from the fitting ($G_{F,L}^{fit}$) and discrete ($G_{F,L}^{dis}$) procedures are reported in Table 7 for each specimen without the external matrix layer and instrumented with strain gauges. The average values of $G_{F,L}^{fit}$ and $G_{F,L}^{dis}$ for each test were calculated from the same four points around point B used to determine the effective bond length $l_{eff,L}$, which is reported in Table 7 for each specimen without the external matrix layer.

The average value of the experimental loads corresponding to the four points within the range $\left(P_{1,L} - P_{2,L}\right)$ used to determine the fracture energies is taken as $P_{deb,L}^{exp}$, which is also identified as the applied load at point B in Figure 17a. The values of $P_{deb,L}^{exp}$ are provided in Table 7.

The load corresponding to the onset of debonding can also be obtained from Eq. (130):

$$\overline{\overline{P}}_{deb,L} = \overline{\varepsilon}_{yy,L} n b^* t^* E \tag{130}$$

where $\overline{\varepsilon}_{yy,L}$, provided in Table 7 for each test, is the average of the strains measured (not fitted) by gauge 4 for the four selected points in the range $\left(P_{1,L} - P_{2,L}\right)$ around point B (see Figure 17a).

Figure 38 compares the experimental values of $P_{deb,L}^{exp}$ with the values of the load $\overline{\overline{P}}_{deb,L}$, $\overline{P}_{deb,L}^{fit}$, and $\overline{P}_{deb,L}^{dis}$, for each specimen without the external matrix layer and instrumented with strain gauges. As for specimens with both the internal and external layer of matrix (§3.12), the values of $\overline{P}_{deb,L}^{fit}$, and $\overline{P}_{deb,L}^{dis}$ presented in Figure 38 are determined using the corresponding average value of the fracture energies provided in Table 7. In general, a good agreement between the average measured debonding load $P_{deb,L}^{exp}$ and the three values obtained from Eqs. (127) and (130) is observed. Nevertheless, as was observed in for specimens with the external matrix layer (§3.12), the results obtained may be affected by the non-uniform load distribution across the width and by the assumed position of point B (Figure 17a).

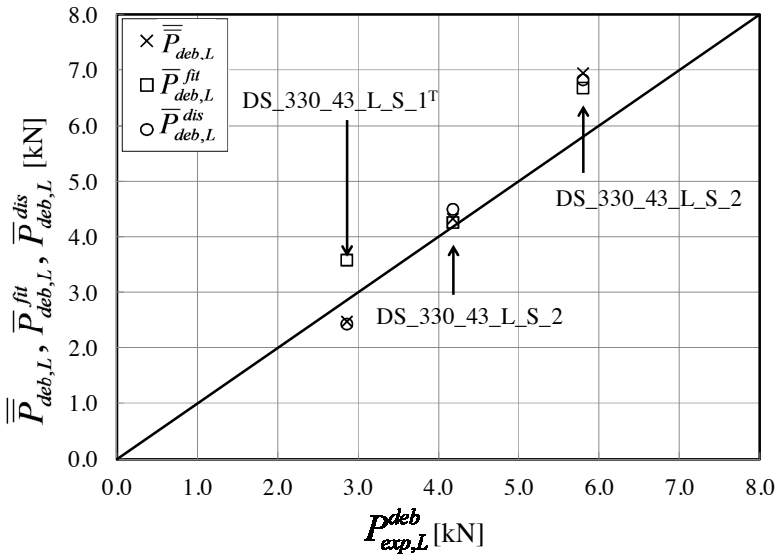

Figure 38. Comparison between the average measured load ($P_{deb,L}^{exp}$) and the values obtained from Eqs. (127) and (130).

4.10 Distribution of load among bundles

Since the fibers used in FRCM composites are usually bundled to improve the bond with the matrix, the experimental applied loads P and P_L were not always evenly distributed among the different bundles (§3.9). Although it was observed that a width

effect does not exist for the entire composite width (§3.9), the different impregnation of the matrix along the fiber bundles and the stochastically distributed properties of the materials involved could cause a different behavior and performance of the fiber bundles. An indication of the non-uniform distribution of the load among the bundles was evidenced by the rigid rotation of the Ω-shaped bent plate as the global slip increased, as well as by the progressive deformation observed in the transversal fiber bundles outside the bonded area, which were orthogonal to the longitudinal fibers at the beginning of the test. Furthermore, for specimens DS_330_43_S_1 and DS_330_43_S_2 (§3.10.3) the strain measured among different fiber bundles for a given applied load value was different, confirming the non-uniform load distribution across the width of the composite [89]. This phenomenon was more pronounced for small bonded widths, whereas it became less important as the bonded width increased. The non-uniform load distribution had a strong influence on the test results and especially on the peak loads P^* and P_L^* (§3.5). Although the load redistribution could occur in real applications, the aim of this chapter is to study the bond behavior of FRCM-concrete joints and investigate the different role of the two layers of matrix. Therefore, the specimens that presented a highly non-uniform load distribution were not considered during the following analysis.

The load redistribution among bundles was studied by comparing the displacements, g_a and g_b, measured by the two LVDTs used to control the test. The points of the Ω-shaped plate off of which the LVDT's tips react are not aligned with the edges of the composite strip (Figure 39). Simple geometrical relations were used to compute the displacement corresponding to the edge of the composite strip, termed g_a^L and g_b^L. Figure 39 shows the displacements measured by the LVDTs and the corresponding displacement aligned with the composite edges.

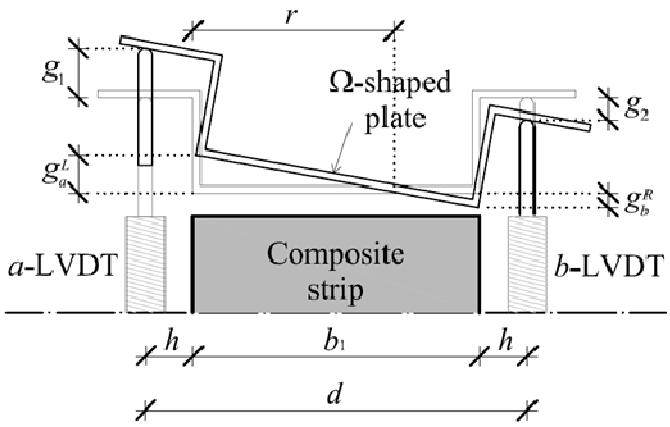

If $g_a^L \cdot g_b^R < 0$

$$g_a^L = g_a \cdot \frac{r+h}{r}$$

$$g_b^R = g_b \cdot \frac{d-h+r}{d+r}$$

If $g_a^L \cdot g_b^R > 0$

$$g_a^L = g_a \cdot \frac{r-h}{r}$$

$$g_b^R = g_b \cdot \frac{d-h-r}{d-r}$$

Figure 39. Position of the LVDTs.

The $P - g_a$, $P - g_b$, $P_L - g_a$, and $P_L - g_b$ curves obtained from the two LVDTs were plotted to compare their behavior. In addition, the difference between the displacements at the two edges $\Delta = \left| g_a^L - g_b^R \right|$ was computed. In order to define a limit beyond which the non-uniform load distribution compromises the reliability of results, the $\tau_{zy}^j - s$ and $\tau_{zy,L} - s_L$ curves obtained from the strain analysis described in §3.12 and §4.9 were employed. Values of the $\tau_{zy,L} - s_L$ curves were compared with values of the $\tau_{zy}^j - s$, assuming that the response of the internal matrix layer is not influenced by the presence of the external matrix layer. The values of the slip corresponding to the peak shear stress, $s_m = s_m^e = s_m^i = s_{m,L}^i$, and to the complete debonding of the fiber, $s_f = s_f^e = s_f^i = s_{f,L}$, were collected from the tests reported in Table 5 and Table 7. The average values are $\bar{s}_m = 0.18$ mm and $\bar{s}_f = 1.51$ mm. The results of the specimens for which Δ was less than $\bar{s}_f$ for values of $P < P^*$ and $P_L < P_L^*$, were considered reliable and used for the following analysis, whereas the others were disregarded. The criterion adopted in this chapter is not unique and further results are necessary to evaluate if other criteria can be used. This criterion was adopted to ensure that at the peak load (P^* or P_L^*) if the residual bonded length was equal to l_{eff} for the bundle on one edge of the composite, the bundle on the other edge was still bonded for a length greater than l_{eff}, which in turn entails that all the bundles effectively contributed to the stress transfer at

the peak load. Specimens for which $\Delta < \bar{s}_f$ for values of $P < P^*$ and $P_L < P_L^*$ are marked with $\surd$, whereas specimens for which $\Delta \geq \bar{s}_f$ for values of $P < P^*$ and $P_L < P_L^*$ are marked with $\times$ (Table 6). It can be observed that forty-two specimens were considered reliable (64% of the all specimens reported in Table 6), whereas twenty-four specimens were disregarded (36% of the all specimens reported in Table 6). Only ten specimens (15% of the all specimens reported in Table 6) reported a Δ less than $\bar{s}_m$ for values of $P < P^*$ and $P_L < P_L^*$, confirming that the applied load is almost always non-uniformly distributed among the different bundles.

Figure 40 shows, as an example, the applied load vs. the two LVDT readings compared with the applied load – global slip curves for two reliable specimens (DS_330_60_L_D_4 and DS_450_60_D_1), and for two specimens disregarded (DS_450_60_L_4 and DS_450_60_3). The applied load – global slip curve is plotted with a light-grey line. When Δ is less than $\bar{s}_f$ for values of $P < P^*$ and $P_L < P_L^*$ the $P - g_a$, $P - g_b$, $P_L - g_a$, and $P_L - g_b$ curves are plotted with a black line, whereas when $\Delta \geq \bar{s}_f$ for values of $P < P^*$ and $P_L < P_L^*$ they are depicted with a dark-grey line. A black dot marks the points for which $\Delta^* = \bar{s}_f$, where Δ^* is the value of Δ corresponding to the peak loads P^* or P_L^*. Figure 40a and Figure 40b show two of the specimens that were tested until complete debonding of the fiber net from the matrix. It can be observed that for specimen DS_450_60_D_1 (Figure 40b) the applied load reached the constant value corresponding to P_f, as reported in the idealized applied load – global slip curve (Figure 17a). For specimen DS_330_60_L_D_4 (Figure 40a) the applied load, after reaching the value corresponding to $P_{f,L}$, slowly decreased because the absence of the external matrix layer might have induced a Mode-I component (peeling) that reduced friction between the fibers and the matrix.

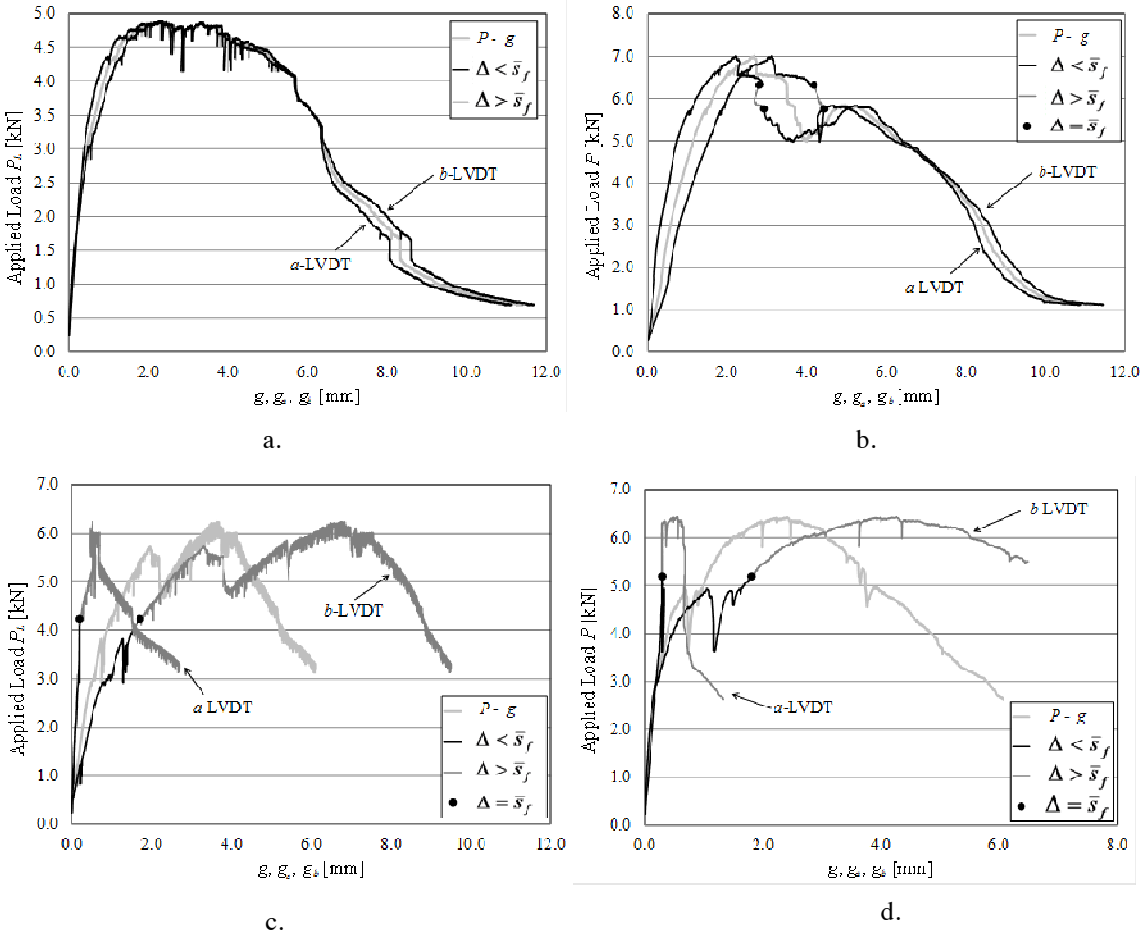

Figure 40. Applied load P vs. LVDTs readings responses for specimen (a) DS_330_60_L_D_4, (b) DS_450_60_D_1, (c) DS_450_60_L_4, and (d) DS_450_60_3.

4.11 Relationship between the internal and external matrix layer

In §4.7 the load responses of specimens without the internal matrix layer are compared with specimens with the external matrix layer. It was observed that the applied load – global slip response does not appear to be affected by the absence of the external matrix layer, which entails for a different bond behavior of the external and internal layer of matrix. In order to obtain a reliable ratio between P^* and P_L^* the distribution of the load among bundles is taken into account; only the specimens with $\Delta < \bar{s}_f$ for values of $P < P^*$ and $P_L < P_L^*$ were used to compare the bond behavior of the two layers of matrix in the stress-transfer mechanism. The ratio between the applied loads of specimens with or without the external layer of matrix is introduced:

$$\eta = P_L / P \tag{131}$$

It should be noted that the ratio provided in Eq. (131) varies with the variation of the

global slip g and should be computed for each point of the $P - g$ and $P_L - g$ curves. Provided that the contributions of friction P_f and $P_{f,L}$ are clearly identified and assuming that the effective bond length l_{eff} does not depend on the matrix layer considered, the debonding load can be obtained using Eq. (132) and Eq. (133):

$$P_{deb} = P^* - P_f \tag{132}$$

$$P_{deb,L} = P_L^* - P_{f,L} \tag{133}$$

Eq. (131) can be re-written in the case of the debonding loads in terms of the normal stress:

$$\eta_{deb} = \sigma_{deb,L} / \sigma_{deb} \tag{134}$$

where $\sigma_{deb,L} = P_{deb,L} / \left(nb^* t^* \right)$ and $\sigma_{deb} = P_{deb} / \left(2nb^* t^* \right)$.

If Eq. (111) and (124) are employed and it is assumed that $G_F^i = G_{F,L}$, which entails that the interfacial behavior between the fibers and the internal layer of matrix is not influenced by the presence of the external layer of matrix:

$$\frac{G_F^i}{G_F^e} = \frac{\eta_{deb}^{\ 2}}{\left(1 - \eta_{deb}^{\ 2}\right)} \tag{135}$$

Considering the results of the reliable specimens tested (Table 6), Eq. (135) provided a value of $\eta_{deb} = 0.85$, which entails for a ratio between the internal- and external-layer fracture energy of $G_F^i / G_F^e = 2.60$. It should be noted that Eq. (135) can be applied only if the deformation of the matrix layer is neglected, i.e. if the slip corresponding to the internal and external matrix-fiber interfaces are equal. Furthermore, since the fracture energy is independent of the shape of the shear stress – slip function, Eq. (135) does not provide information on the $\tau_{zy}^j - s^j$ curves.

4.12 Effects of the transversal fiber bundles

The experimental results obtained through direct-shear tests on specimens with and without the external layer of matrix clearly show that the internal and external-matrix layer provide different contributions to the total strength of FRCM-concrete joints. As mentioned in §3.3, the transversal fiber bundles are all placed on one side of the fiber net, i.e. the longitudinal and transversal bundles are not woven but held together through glass-fiber filaments. Thirteen of the 66 specimens presented in this work were cast with the transversal fiber bundles directly against the external matrix layer. Fifty of the 53 remaining specimens had the longitudinal fiber bundles directly against the internal layer of matrix (specimens denoted with a superscript T after the sequential

number in Table 6), whereas for the remaining three specimens the transversal bundles were removed before applying the matrix layers (specimens denoted with a T before the sequential number in Table 6). This expedient allowed for studying the effect of the transversal bundles, which affect the stress-transfer mechanism between the matrix and the fiber by interrupting the bond between the longitudinal fiber bundles and the matrix. Whether the transversal bundles are placed against the internal or external layer of matrix, the area of contact between the transversal bundles and the longitudinal bundles (see also Figure 48) is characterized by friction between filaments rather than stress transfer due to bond. This entails that either at the interface with the internal or external layer of matrix, the presence of the transversal bundles might influence the stress-transfer mechanism.

Since the presence of the transversal bundles reduces the contact area between the longitudinal bundles and the matrix, it could be stated that the external matrix layer has a minor contribution with respect to the internal matrix layer because of the reduced bonded area of the longitudinal bundles in contact with the external matrix layer. In order to investigate the influence of the transversal bundles on the matrix external layer behavior, three specimens were constructed with the longitudinal fibers embedded between the internal and external layer of matrix after removing the transversal bundles (Figure 41).

Figure 41. PBO fiber net after removing the transversal bundles.

The specimens with the external matrix layer and without the transversal fiber bundles, DS_330_60_T_1, DS_330_60_T_2, and DS_330_60_T_3, presented the same behavior as the specimens with the external matrix layer and with the transversal fiber bundles placed directly against the matrix external layer. Furthermore, all specimens without the transversal bundles resulted in $\Delta < \bar{s}_f$ for values of $P < P^*$ and $P_L < P_L^*$ (i.e. $\surd$ in Table 6), which indicated the almost-even distribution of the load among the different longitudinal bundles. The load responses of these specimens are of particular importance because they confirm that the matrix external layer provides a different contribution with respect to the matrix internal layer even when the bond between the longitudinal fiber bundles and the matrix is not interrupted by the transversal fiber bundles. Figure 42a reports the load responses of the specimens without the transversal fiber bundles and of the specimen DS_330_60_2 for comparison. The $P - g_a$ and

$P - g_b$ responses of specimen DS_330_60_T_3 are reported in Figure 42b with the corresponding $P - g$ plot for comparison.

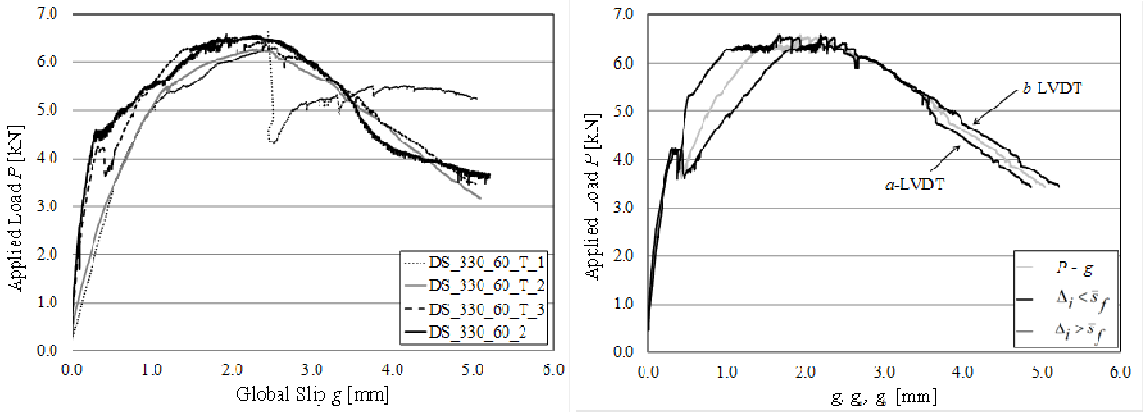

a. b.

Figure 42. a) $P - g$ response of specimens without the transversal bundles and DS_330_60_2 for comparison. b) Applied load P vs. LVDTs readings curves for specimen DS_330_60_T_3.

A comparison in terms of the peak load for reliable specimens with two layers of matrix and the transversal bundles placed against either the internal or the external layer indicates that, when both layers of matrix are present, the peak load is not influenced by the position of the transversal bundles. Specimens with the same bonded width and length were compared. Further, the results obtained considering only the reliable specimens (specimens marked with √ in Table 6) show that for specimens with two layers of matrix the presence of the transversal bundles seems to have a slight influence with respect to the specimens without the transversal bundles (7% of difference in terms of peak stress σ^*). These results can be in part related to the role of the external layer of matrix. In fact, it was observed that specimens with one layer of matrix showed a debonding load equal to 85% of the debonding load of reliable specimens with two layers. This suggests that the stress transfer occurs mainly at the fiber-internal layer interface. However, it is interesting to notice that when the fiber bundles are placed against the internal layer and both layers are present the peak load is not significantly affected. Analyzing the specimens without the external matrix layer and the transversal bundles placed against the internal matrix layer, it can be noted that the distribution of the load among bundles is particularly uneven, and none of the specimens can be considered reliable. For this reason a comparison in terms of peak load cannot be carried out for specimens without the matrix external layer and with different positions of the transversal bundles. It should be noted that the external matrix layer may play an important role in the distribution of load among the longitudinal bundles when the transversal bundles are placed against the internal matrix layer.

4.13 Theoretical bond-slip relationships

In §3.12 and §4.9, a fracture mechanics approach was attempted considering the contribution of the internal and external matrix layer as equal. Although the results were in good agreement with experimental values, such approach, though effective in case of a single layer of fibers, may not be able to provide reliable results in case of multi-layer strengthening applications because it may overestimate the total fracture energy.

In an attempt to investigate the different contribution of the internal and external layers of matrix, the ratio between the internal and external fracture energies, G_F^i and G_F^e, was introduced through Eq. (134) and Eq. (135). The ratio was obtained under the assumption that $G_F^i = G_{F,L}$. In this section the same assumption is adopted to further study the role of the internal and external matrix layers and to identify the fracture parameters needed to describe the $\tau_{zy}^j - s^j$ curves. Hence, Eq. (132) and Eq. (133) were applied to compute the debonding loads of specimens with and without the external matrix layer, P_{deb} and $P_{deb,L}$, which were used to calculate the corresponding debonding stress σ_{deb} and $\sigma_{deb,L}$, respectively. The results obtained were compared using Eq. (134) providing the ratio between the fracture energies corresponding to the internal and external matrix layer (Eq. (135)).

Since the fracture energy G_F^j does not depend on the shape of the corresponding $\tau_{zy}^j - s^j$ curve, the experimental shear stress-slip curves for specimens with and without the external layer of matrix were simplified into three-branch linear relationships with the same fracture energy, i.e. $G_F^j = G_F^{sim}$ (Figure 28). The maximum shear stress $\tau_{zy,m}^j$, the frictional stress $\tau_{zy,f}^j$, and the slope of the linear ascending part of the $\tau_{zy}^j - s^j$ curve were kept as fixed quantity. Once these parameters are determined, the simplified $\tau_{zy}^j - s^j$ relationship is uniquely defined.

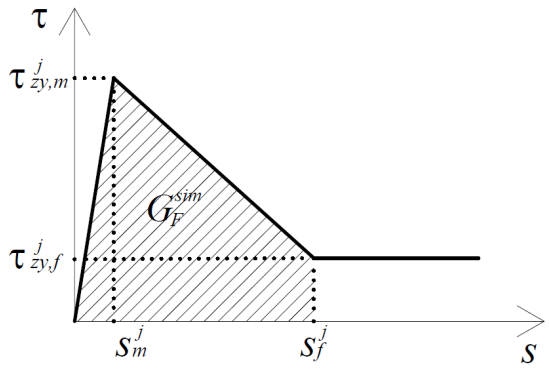

Figure 43. Simplified shear stress τ_{zy}^j vs. slip s^{sim} curve.

Since Eq. (135) must be satisfied for each $\tau_{zy}^j - s^j$ curve, provided that the $\tau_{zy,L}^i - s_L^i$ is

obtained from the procedure described in §4.8 for specimens without the external matrix layer, Eq. (135) can be used to identify the shear stress vs. slip behavior of the external-matrix layer. Three different theoretical models of the $\tau_{zy}^{e} - s^{e}$ are herein proposed.

4.13.1 Model a.

Hypothesis: the linear ascending branch of the $\tau_{zy}^{j} - s^{j}$ curves has the same slope both in case of internal and external-matrix layer; the slip corresponding to the onset of friction between fiber filaments and between matrix and fiber is equal both in case of internal and external-matrix layer, i.e.:

$$\frac{\tau_{zy,m}^{i}}{s_{m}^{i}} = \frac{\tau_{zy,m}^{e}}{s_{m}^{e}} \tag{136}$$

$$s_{f}^{i} = s_{f}^{e} = s_{f} \tag{137}$$

Figure 44 shows the $\tau_{zy}^{j} - s^{j}$ curves which satisfy Eq. (135), (136) and (137).

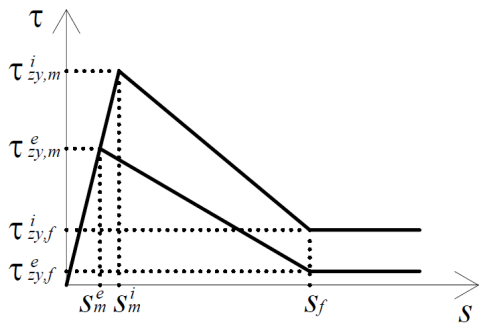

Figure 44. Theoretical shear stress vs. slip curves according to *Model a*.

4.13.2 Model b.

Hypothesis: the slip corresponding to the maximum value of the shear stress, $\tau_{zy,m}^{j}$, and to the onset of friction between fiber filaments and between matrix and fiber is equal both in case of internal and external-matrix layer. This assumption provides the following equation in addition to Eq. (137):

$$s_{m}^{i} = s_{m}^{e} = s_{m} \tag{138}$$

Figure 45 shows the $\tau_{zy}^{j} - s^{j}$ curves which satisfy Eq. (135), (137) and (138).

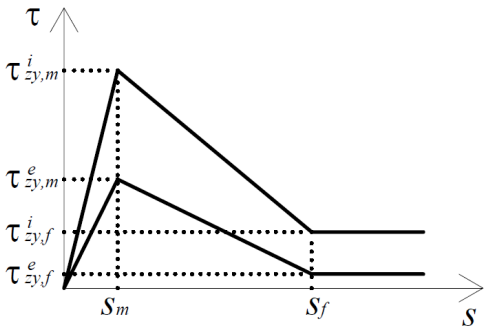

Figure 45. Theoretical shear stress vs. slip curves according to *Model b*.

4.13.3 Model c.

Hypothesis: the slip corresponding to the maximum value of the shear stress, $\tau^{j}_{zy,m}$, and to the slope of the linear ascending branch of the $\tau^{j}_{zy} - s^{j}$ curves are equal both in case of internal and external-matrix layer, which is expressed by Eq. (136) and (138). Figure 46 shows the $\tau^{j}_{zy} - s^{j}$ curves which satisfy Eq. (135), (136) and (138).

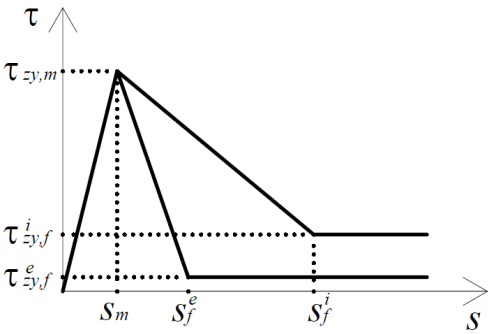

Figure 46. Theoretical shear stress vs. slip curves according to *Model c*.

4.14 Experimental bond-slip relationships

Assuming that the presence of the external matrix layer does not influence the behavior of the internal matrix layer, the experimental results of the specimens without the external matrix layer were employed to determine the simplified shear stress-slip relationship between the internal matrix layer and the fiber net. Only those specimens that report a $\Delta < \bar{s}_f$ for values of $P < P^*$ and $P_L < P^*_L$ were considered (Table 7). The strain analysis of specimens DS_330_43_L_S_1[T], DS_330_43_L_S_2, and DS_330_60_L_S_1 provided the average values of the maximum shear stress $\tau^{i}_{zy,m}$ and the corresponding average slip s^{i}_{m} of the internal matrix-fiber interface. Eq. (123) was

used to compute the average of the shear stress $\tau^{i}_{zy,f}$ obtained from each specimens without the external matrix layer (i.e., $\tau^{i}_{zy,f} = \tau_{f,L}$). The corresponding slip s^{i}_{f} was obtained from the $\tau^{i}_{zy} - s^{i}$ curves provided by the strain analysis of the specimens without the external matrix layer equipped with strain gauges. The curves obtained are depicted in Figure 47a, Figure 47b, and Figure 47c for *Model a*., *Model b*., and *Model c*. respectively. The parameters corresponding to Figure 47 are listed in Table 8. The values of the shear stress and corresponding slip listed in Table 8 can be used to investigate the bond behavior of the internal and external matrix layer through the use of numerical simulations (see §1).

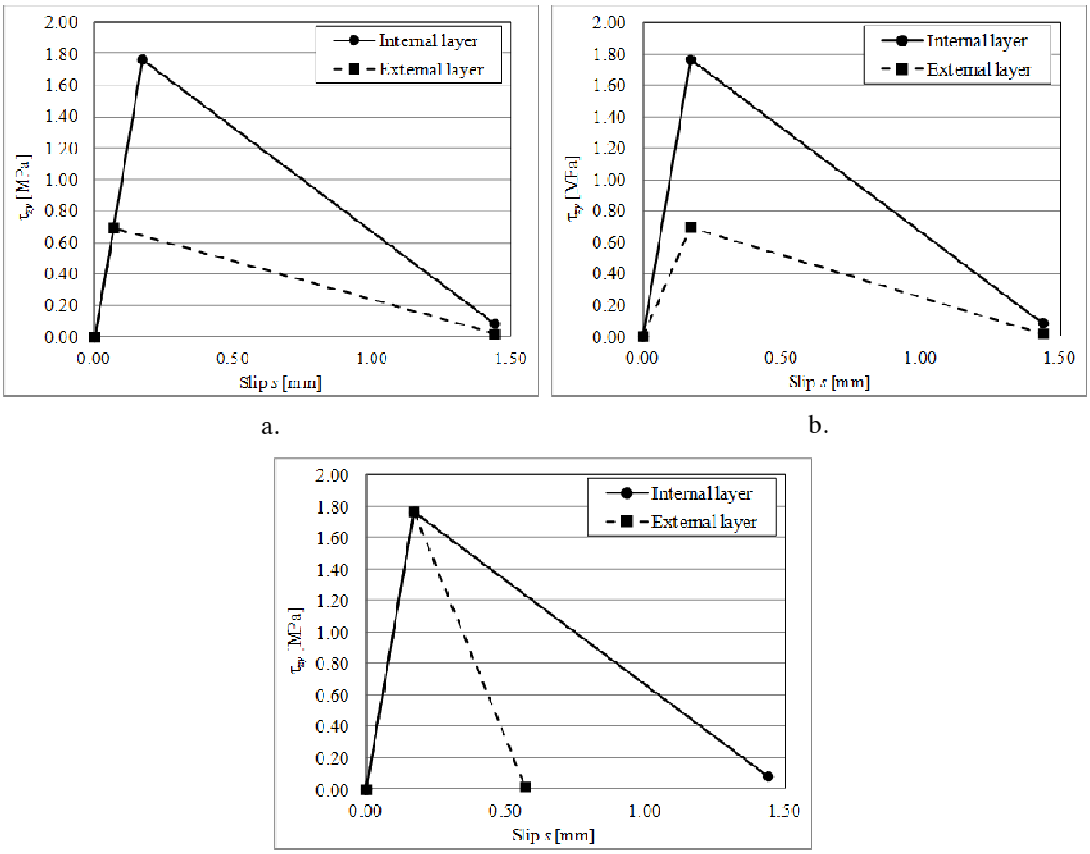

a. b.

c.

Figure 47. Shear stress vs. slip relationships for *Model a*. (a.), *Model b*. (b.), and *Model c*. (c.).

Table 8. Internal and external shear stress and corresponding slip in case of different bond-slip relationship**.**

Model	$\tau^{i}_{zy,m}$ [MPa]	s^{i}_{m} [mm]	$\tau^{e}_{zy,m}$ [MPa]	s^{e}_{m} [mm]	$\tau^{i}_{zy,f}$ [MPa]	s^{i}_{f} [mm]	$\tau^{e}_{zy,f}$ [MPa]	s^{e}_{f} [mm]
a.	1.764	0.17	0.690	0.067	0.083	1.44	0.016	1.44
b.	1.764	0.17	0.692	0.17	0.083	1.44	0.016	1.44
c.	1.764	0.17	1.764	0.17	0.083	1.44	0.016	0.57

4.15 Conclusions

The experimental and analytical investifigation of PBO FRCM-concrete joints tested using the single-lap direct-shear set-up is presented in this chapter. The specimens tested were comprised of a PBO fiber net bonded to the concrete substrate by means of a cementitious matrix (internal) layer. The stress-transfer mechanism between the PBO fiber and the cementititous matrix was investigated through the application of a fracture mechanics approach. The results obtained were compared with the results of PBO FRCM-concrete joints that included an additional (external) matrix layer applied over the fiber in order to investigate the bond behavior of the internal and external matrix layers. Based on experimental observations, two simplified shear stress-slip relationships were proposed to describe the bond behavior of the internal and external layer of matrix. Finally, the paramaters obtained from the fracture mechanics approach and the experimental results were employed to compute the shear stress and corresponding slip of the simplified shear stress-slip relationships proposed. Based on the evidences and discussion presented, the following conclusions can be drawn:

1. The idealized applied load-global slip behavior put forward for FRCM-concrete specimens with both the internal and external layers of matrix is valid also for specimens without the external layer of matrix. As for specimens with the external layer of matrix, the load response of specimens without the external layer of matrix is characterized by increasing slip at the matrix-fiber interface and by the presence of friction between single filaments and between fibers and matrix. Friction between single filaments within the fiber bundle is always present during the load application, whereas friction between fibers and matrix provides its contribution after the onset of debonding.
2. Assuming that the axial deformation of the matrix layers can be neglected, the fracture mechanics approach used for FRP-concrete joints was applied to FRCM-concrete joints without the external layer of matrix. The results obtained in terms of debonding load are in good agreement with the experimental results.
3. The transversal fiber bundles, which are all placed on one side of the fiber net, can be oriented against the internal or external matrix layer. The load response of specimens with both the internal and external matrix layer is not affected by the orientation of the transversal fiber bundle. However, for specimens without the external matrix layer the presence of the transversal bundles against the internal matrix layer reduced the value of the peak load.
4. Assuming that the presence of the external matrix layer does not influence the behavior of the internal matrix layer, the results of the fracture mechanics approach applied to specimens with and without the external matrix layer allowed for comparing the fracture energy corresponding to the different matrix layers. The ratio of the fracture energies associated with the internal and external matrix layers is equal to 2.60. Based on this observation, further investigation is needed to study the behavior of the different matrix layers for FRCM

composites that include more than two layers of matrix (i.e., PBO FRCM composites with more than one layer of fibers).

5. The simplified shear stress-slip relationships proposed to describe the behavior of the internal and external layers of matrix can be used to investigate the stress-transfer mechanism at the different matrix-fiber interfaces. The values of the shear stress and slip computed can be used in numerical simulations to study the behavior of the matrix layers.

5 NUMERICAL ANALYSIS OF PBO FRCM-CONCRETE JOINTS

5.1 Abstract

The bond behavior of fiber reinforced cementitious matrix (FRCM) composites applied to concrete elements is investigated in this chapter by means of a three-dimensional numerical analysis. The FRCM-concrete joints studied are part of an extensive experimental campaign conducted using the single-lap direct-shear test set-up (§1, §1), and include specimens both with and without the external layer of matrix. The input data of the numerical models are obtained applying a fracture mechanics approach that allowed for studying the shear stress-slip relationship that characterize the matrix-fiber interfaces (§1, §1). The load responses and strain profiles obatined from the numerical models of specimens with and without the external matrix layer are compared with the corresponding load responses and strain profiles observed in the experimental tests. A good agreement between the numerical solutions and the experimental results is obtained.

5.2 Introduction

Among fiber reinforced materials for strengthening reinforced concrete (RC) structures, FRCM composites represent a newly-developed and promising solution for flexural strengthening, shear strengthening, and confinement of structural elements mostly subjected to compressive load [19, 20, 21, 40, 58, 78, 79, 80, 81, 102, 106, 109]. FRCM composites are comprised of high strength fibers embedded within two layers of cementitious matrix. The high strength fibers are subjected to tensile load whereas the matrix layers are responsible for the stress-transfer mechanism between the fibers and the concrete support. For this reason, the investigation of the bond behavior in FRCM-concrete joints is of fundamental importance for the effective application of this strengthening technique.

In this chapter, the stress-transfer mechanism in FRCM-concrete joints is investigated by means of a three-dimensional numerical analysis carried out using the software Abaqus. The experimental results used for the calibration of the numerical models are part of an extensive experimental campaign carried out on PBO FRCM-concrete joints tested using the single-lap direct-shear test set-up (§1, §1). As a first attempt to study the stress-transfer mechanism between the composite and the concrete substrate, a fracture mechanics approach was applied assuming that the internal and external matrix

layers have the same bond behavior (§1). Although this hypothesis provided results in terms of debonding load that are in good agreement with the experimental evidences, the analysis of specimens with and without the external matrix layer showed that the contribution of the different layers to the bond strength is different (§1).
The numerical analysis presented in this chapter is used to study the behavior of the internal and external layers of matrix. The data obtained from the fracture mechanics approach applied to PBO FRCM-concrete joints with and without the external layer of matrix are used to calibrate the numerical models. The numerical load responses, strain profiles along the bonded length, and shear stress-slip relationships of the internal and external matrix-fiber interfaces are compared with the corresponding experimental evidences of specimens with and without the external layer of matrix. The numerical results obtained are in good agreement with the experimental observation and can be used to investigate the complex stress-transfer mechanism between the fiber and the matrix.

5.3 Experimental tests

The numerical models described in this chapter are based on the results of the experimental campaign conducted on FRCM-concrete joints illustrated in §1 and §1, which is herein briefly recalled for the sake of clarity.
The FRCM composite studied is comprised of a PBO fiber net applied to a concrete prism by means of a cementitious matrix. The classical push-pull configuration was adopted where the fibers were pulled while the concrete prism was restrained [25, 98, 99]. The PBO fiber net was applied onto a first (internal) 4 mm thick layer of matrix that is cast on one of the concrete prism surfaces. A second (external) 4 mm thick layer of matrix was then applied over the internal layer of matrix to protect the fibers and improve the bond between the fibers and the matrix. The external layer of matrix was applied for some specimens, whereas it was omitted for others. The parameters varied were the composite bonded width b_1 and bonded length ℓ. Furthermore, some specimens were equipped with strain gauges applied on the fibers to measure the strain along the bonded length.
The concrete blocks used were 375 mm long and had a 125 mm width × 125 mm depth cross section. The surface of the concrete block on which the FRCM composite was applied was sandblasted to improve the bond between the internal layer of matrix and the substrate. The fiber net was comprised of PBO fiber bundles spaced at 10 mm in the longitudinal direction and at 20 mm in the transversal direction. The transversal bundles are not woven to the longitudinal bundles but are placed all on one side of the fiber net. The thickness and width of a single PBO fiber bundle is $t^* = 0.092$ mm and $b^* = 5$ mm, respectively.
The concrete prisms were characterized by means of compressive and tensile tests of six 100 mm × 200 concrete cylinders cast from the same batch used to construct the prisms.

Three cylinders were tested in compression providing an average compressive strength [13] of 42.5 MPa (CoV=0.013). The average splitting tensile strength [14] obtained from the remaining three cylinders was 3.4 MPa (CoV= 0.113). From each batch used to construct the composite specimens, a minimum of two 50 mm × 100 mm cylinders were cast to characterize the matrix. The compressive [13] and splitting tensile [14] strength of the matrix were 28.4 MPa (CoV=0.092) and 3.5 MPa (CoV=0.231), respectively. The mechanical characteristic of the PBO fibers were determined by means of tensile tests of PBO fiber net specimens with different width b_2. The average measured tensile strength σ^* (Eq. (90)), ultimate strain, and elastic modulus E were 3014 MPa (CoV = 0.068), 0.0145 (CoV = 0.104), and 206 GPa (CoV = 0.065), respectively.

The single-lap direct-shear tests were conducted in displacement control. The slip of the PBO fiber net with respect to the concrete prism, termed global slip g, was used to control the tests that were conducted at a constant rate of 0.00084 mm/s [25, 98, 99].

Further details regarding the experimental tests can be found in §1 and §1.

5.4 Experimental tests

The weakness of PBO FRCM-concrete joints is reported to be at the matrix-fiber interface, which leads the composite to fail due to debonding of the fibers from the embedding matrix [42, 79, §1, §1]. Based on the information inferred from the results of the experimental campaign described in §1 and §1 and the experimental and analytical evidence available in the literature [16, 39, 56], the idealized load response of a PBO FRCM-concrete joints shown in Figure 17a was proposed. According to Figure 17a, the applied load P increases until reaching the value P_{deb}, which corresponds to the onset of debonding (point B in Figure 17a). After that, the applied load further increases due to the presence of friction between single fiber filaments and between fibers and matrix. When the residual bonded length l_r is equal to the effective bond length l_{eff}, which is the minimum length needed to fully establish the stress-transfer mechanism [25, 32], the applied load attains the peak load P^* (point C in Figure 17a). With further increasing of the global slip the fibers completely debond from the matrix and the applied load assumes the constant value P_f, which is due to the friction between fiber filaments and between fibers and matrix (point E in Figure 17a). It should be noted that the debonding process is complicated by the telescopic behavior observed among the fiber filaments, which is mainly due to the different impregnation of the fibers by the matrix [16, 57].

The stress transfer mechanism in PBO FRCM-concrete joints was investigated employing the fracture mechanics approach previously used to study FRP-concrete joints (§1). In general, the bond behavior of the internal matrix layer may be different from the bond behavior of the external matrix layer. The stress-transfer mechanism

associated with the internal and external matrix-fiber interfaces can be described by the shear stress τ_{zy}^{j} vs. slip s^{j} relationship, where the superscript j is equal to i or e, to indicate the internal or external matrix layer, respectively. To obtain the $\tau_{zy}^{j} - s^{j}$ curves, the strain profiles of specimens equipped with strain gauges were fitted using a non-linear equation previously used for FRP-concrete joints and modified to take into account the presence of friction (Eq. (93)). The strain profiles computed from this fitting procedure follows an "S" shape with a value nominally equal to zero toward the free end and a linearly increasing value where the fibers debonded from the matrix at the loaded end. The distance between the point where the strain is nominally equal to zero and the point in which the derivative of the strain starts to be constant determines the stress transfer zone (Figure 53b) and represents the effective bond length l_{eff} of the composite (§1). As a first attempt to determine the $\tau_{zy}^{j} - s^{j}$ relationships for specimens with both the internal and external layers of matrix, it was assumed that the bond behavior of the internal and external layers of matrix was equal, i.e. $\tau_{zy}^{i} = \tau_{zy}^{e} = \tau_{zy}$ and $s^{i} = s^{e} = s$ (§3.12). The derivative and integral of the fitting curves are used to determine the corresponding shear stress τ_{zy} and slip s, according to Eq. (112) and Eq. (110), respectively. The integral of the $\tau_{zy} - s$ curves obtained represents the fracture energy G_F associated with each matrix-fiber interface (Eq. (113)).

The same fracture mechanics approach used for specimens with the external matrix layer was applied to specimens without the external matrix layer. The $\tau_{zy,L} - s_L$ relationship, effective length $l_{eff,L}$, and fracture energy $G_{F,L}$, where the subscript L indicates the results obtained from specimens without the external matrix layer, were obtained from specimens equipped with strain gauges and without the external layers of matrix. In order to improve the understanding of the bond behavior of the internal and external matrix layer, the results obtained from the specimens without the external matrix layer were compared with the results of specimens with both the internal and external matrix layers. Assuming that the behavior of the internal matrix layer is not influenced by the presence of the external matrix layer, i.e. $p^{i} = p_L$ for each p parameter considered, the fracture energy corresponding to the internal and external matrix layers was computed (§1). The ratio between the internal and external matrix layers' fracture energy was found to be $G_F^{i} / G_F^{e} = 2.60$ (Eq. (135)).

5.5 Numerical modeling

The FRCM composites analyzed are comprised of a PBO fiber net bonded to the concrete substrate by means of a cementitious matrix. The fiber net was embedded between two layers of matrix for some specimens, whereas it was applied onto a single

matrix layer for others. Since the cementitious matrix is not able to penetrate through the fiber bundles [16, 57], the external layer of matrix, when present, is connected to the internal layer of matrix through the mesh of the fiber net. The contact surface between the external and internal layer of matrix for the case of a specimen with the transversal bundles placed against the external layer of matrix is depicted in dark grey in Figure 48. Since the internal and external matrix layers are not connected along the surface of the longitudinal fiber bundles, a two-dimensional numerical model would not be able to simulate the matrix-fiber interface and reproduce the contact between the internal and external layers of matrix at the same time. For this reason, a three-dimensional numerical model that allows for studying the bond behavior of the matrix-fiber interfaces, providing the connection between the external and internal layer of matrix, was adopted.

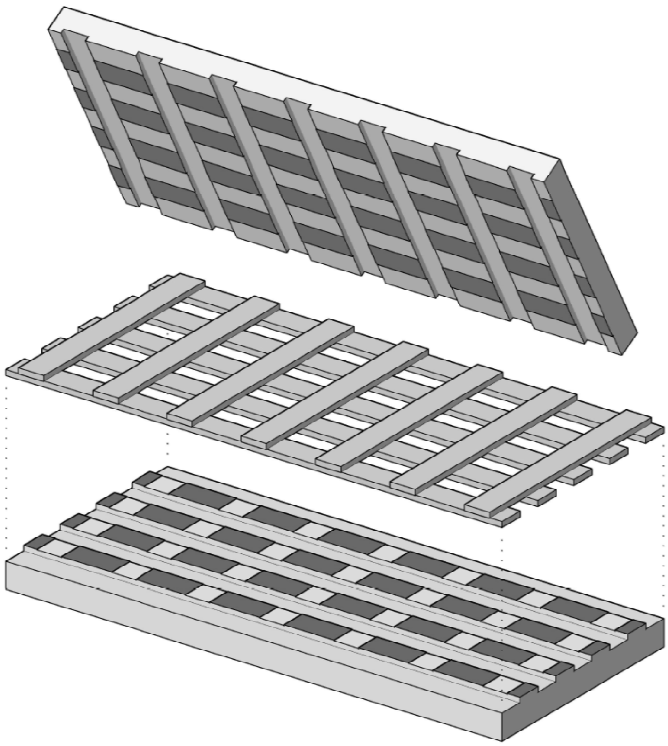

Figure 48. Contact surface of between the internal and external layers of matrix.

The results reported in §3.9 showed that a global width effect does not exist among multiple fiber bundles and therefore for the entire width of the composite. For this reason, the numerical model presented is comprised of a single fiber bundle bonded to one or two matrix layers, and the results obtained are multiplied by the number of bundles present in the corresponding experimental test. It should be noted that the bundles placed at the edges of the composite are not completely surrounded by the matrix (Figure 48), and they may not be able to develop the same bond capacity as the bundles inside the composite strip with matrix on each side. The effect of the different

edge bundles bond capacity, which might affect the results obtained multiplying the response of a single fiber bundle with matrix on each side, will be investigated in §5.8.
As a first attempt to reproduce the real behavior of the FRCM composite, both the PBO fibers and the matrix layers were specified as homogeneous isotropic linear elastic materials. The matrix-fiber interfaces were modeled by means of a master-slave contact interaction that follows a cohesive damage law specified in the software Abaqus. The contact between the matrix and the lateral surfaces of the fiber bundle, which have an area equal to 0.092 mm^2 per unit length, were disregarded. In order to specify the contact law the normal behavior and the shear stress-slip relationship between the master and slave surfaces have to be defined. The normal behavior was specified using a "hard contact" pressure overclosure relationship. According to this relationship, when the surfaces are in contact, i.e. the clearance between them reduces to zero, the contact pressure can be transmitted between them, whereas the contact pressure is zero when the surfaces separate [1].

The $\tau_{zy}^{j} - s^{j}$ curves obtained from the experimental tests (§3.12) were employed to determine the input values for the shear stress-slip relationship between the master and slave surfaces. The linear elastic branch of the $\tau_{zy}^{j} - s^{j}$ relationships was modeled using a surface-based cohesive behavior, whereas the non-linear branch was modeled introducing a damage variable that simulates the interface degradation. The surface-based cohesive behavior is suitable for modeling interfaces for which the thickness is negligibly small, as in case of the FRCM matrix-fiber interface. It is expressed by a linear elastic traction-separation model that relates the normal and shear stresses to the normal and shear separation across the interface by means of an elastic constitutive matrix $\mathbf{K}$ [1]. The cohesive behavior can be expressed by Eq. (139):

$$\mathbf{t} = \begin{Bmatrix} t_n \\ t_s \\ t_t \end{Bmatrix} = \begin{bmatrix} K_{nn} & K_{ns} & K_{nt} \\ K_{sn} & K_{ss} & K_{st} \\ K_{tn} & K_{ts} & K_{tt} \end{bmatrix} \begin{Bmatrix} \delta_n \\ \delta_s \\ \delta_t \end{Bmatrix} = \mathbf{K}\boldsymbol{\delta} \tag{139}$$

where $\mathbf{t}$ is the traction vector of normal component t_n and shear components t_s and t_t, whereas δ_n, δ_s, and δ_t are the corresponding components of the separation vector $\boldsymbol{\delta}$. The cohesive behavior does not interact with the “hard contact” pressure overclosure relationship since the former contributes to the normal behavior only when a slave node is open, i.e. when it is not in contact with the master surface, whereas only the latter acts when a slave node is closed, i.e. when it is in contact with the master surface. In order to model the non-linear branch of the $\tau_{zy}^{j} - s^{j}$ relationships, a damage criterion was introduced into the linear elastic cohesive law, which allows for modeling the degradation and failure of the bond between the master and slave surfaces. The onset of damage was specified defining the limit values t_n^0, t_s^0, and t_t^0 of the traction vector

components beyond which the damage variable d reduces the corresponding stress t_n, t_s, and t_t, respectively, according to Eq. (140):

$$t_i = \begin{cases} (1-d)\cdot \bar{t}_i & \text{if } \bar{t}_i > t_i^0 \\ \bar{t}_i & \text{if } \bar{t}_i \le t_i^0 \end{cases} \tag{140}$$

where t_i is the *i*-th component of the traction vector. The damage evolution law is then specified by defining the values of the damage variable with respect to the non-dimensional plastic displacement $\delta_s = \delta_i^u - \delta_i^0$, which is the difference between the effective separation at complete failure δ_i^u and the effective separation at the onset of damage δ_i^0.

5.6 Numerical results of specimens DS_330_43_S_5

The experimental results of specimen DS_330_43_S_5, presented in §3.12, were employed to specify the numerical model comprised of a single longitudinal bundle of PBO fiber embedded within two layers of matrix, termed DS_330_43_S_5_num. The transversal fiber bundles were not included in the numerical model since the fracture mechanics approach used to define the model parameters was determined without taking into account the presence of the transversal fiber bundles (§3.11). Each matrix layer has length, thickness, and width of 330 mm, 4 mm and 10 mm, respectively, and was implemented in the numerical code as a continuum body with the fiber bundle placed in a through-length hole at the center of the body cross-section (Figure 49). The fiber bundle has the same length as the matrix layers and a 0.092 mm thick × 5 mm wide rectangular cross-section. Since the fracture mechanics approach applied to the experimental results was carried out without considering the matrix deformation (§3.11), the $\tau_{zy}^j - s^j$ curves obtained include the effect of the matrix deformation. For this reason, the matrix layers were specified as quasi-rigid bodies by setting their elastic modulus E_m equal to 1000 GPa. The elastic modulus of the fiber was $E = 206000$ MPa, as per the experimental tensile tests. The value of poisson's ratio of the matrix and the fiber bundle was 0.2 and 0.3, respectively.

The concrete substrate, whose deformation is assumed to be negligible with respect to the matrix and fiber deformation (§3.11), was not modeled. The internal matrix layer surface that should be bonded to the concrete substrate was restrained from any movement (encastre). A displacement $\delta = 4$ mm in the longitudinal (*y*) direction was applied to one end of the fiber bundle (Figure 49).

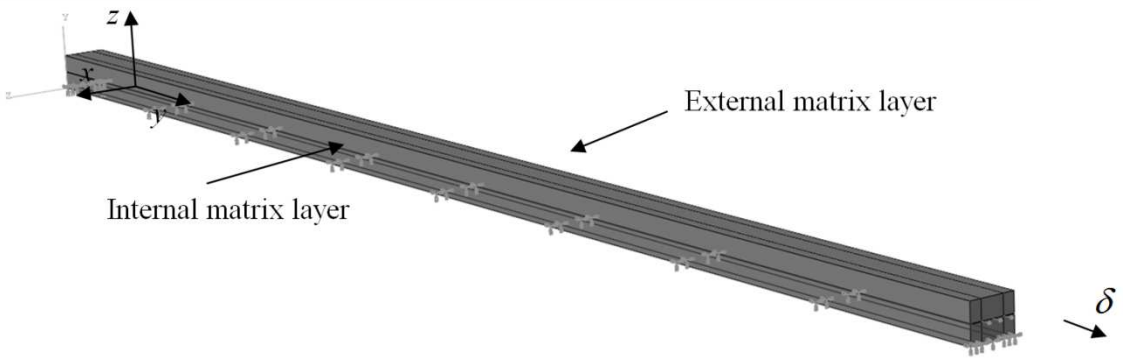

Figure 49. Model DS_330_43_S_5_num

The fiber matrix internal and external interfaces were defined by a master-slave contact, where the matrix represents the master, and the fiber represents the slave. The $\tau_{zy}^{j} - s^{j}$ curves obtained from the fracture mechanics approach applied to specimen DS_330_43_S_5 were used to determine the shear parameters needed to define the damage cohesive contact law that controls the master-slave interaction. The shear stress $\tau_{zy}^{i} = \tau_{zy}^{e} = \tau_{zy}$ versus slip $s^{i} = s^{e} = s$ relationship of point B5 (Figure 25a), obtained assuming that the bond behavior of the internal and external matrix layers is equal (§3.11), was used to determine the damage variable d and the corresponding non-dimensional plastic displacement δ_s. Likewise, the shear stress corresponding to the onset of damage, τ_{zy}^{0}, was defined analyzing the elastic branch of the $\tau_{zy} - s$ curve of point B5 (Figure 25a) and was assumed equal to 0.5 MPa (Figure 50).

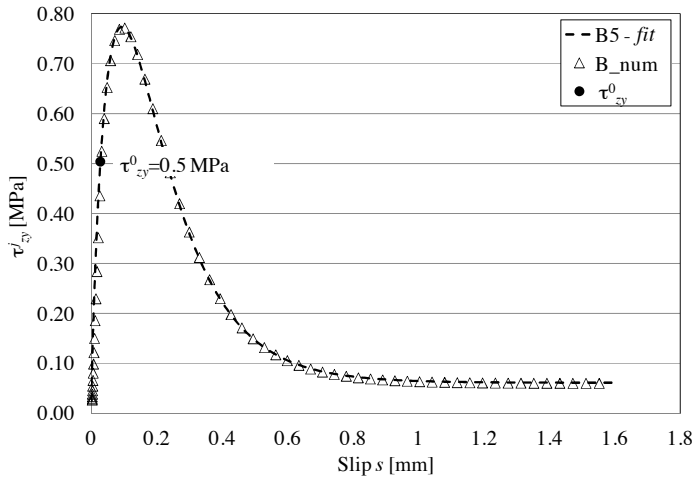

Figure 50. Comparison between the fitted and numerical shear stress vs. slip curve of point B5 (Figure 25a) and B_num, respectively.

Both the fiber bundle and the matrix were modeled using eight-node linear brick elements. Different mesh sizes were employed to verify the influence of the model discretization. The mesh size adopted and herein described was found to be the best

model discretization since it provides precise results with a short solution time. The matrix was discretized into 26424 cube elements with an average edge of 0.4 mm, except for the prismatic elements placed next to fiber bundle lateral surfaces (Figure 51). The fiber bundle was discretized in three brick elements along the bundle thickness with a size of approximately 0.5 × 0.5 × 0.03 mm in x, y, and z directions, respectively. The total number of brick elements in the fiber bundle is 19800 (Figure 51).

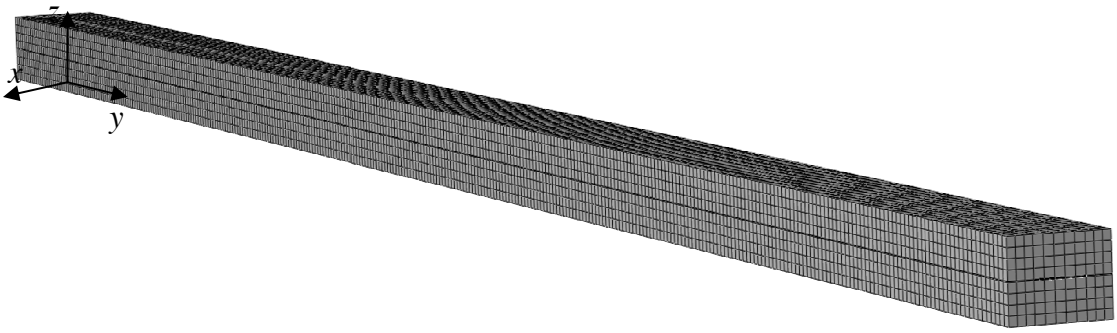

Figure 51. Mesh of model DS_330_43_S_5_num.

The numerical model provided quite accurate results with respect to the experimental observations. Figure 52 shows the comparison between the load response of specimen DS_330_43_S_5 and the load response of the numerical model DS_330_43_S_5_num.

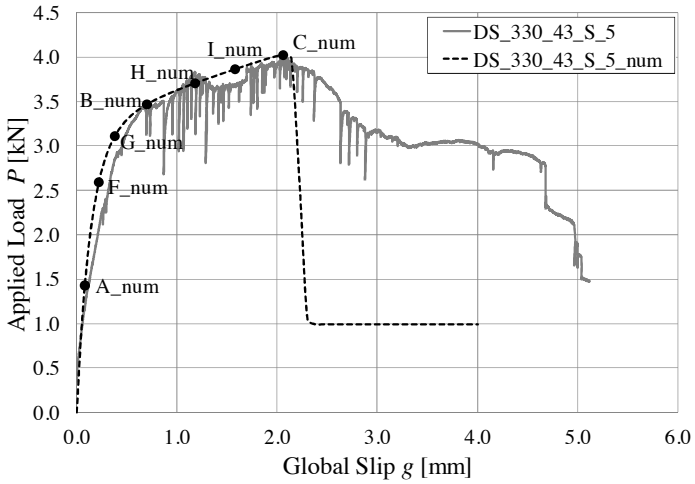

Figure 52. Load responses of specimen DS_330_43_S_5 and model DS_330_43_S_5_num.

Point A_num, B_num, and C_num of the numerical load response depicted in Figure 52 correspond to point A, B, and C, respectively, of the idealized load response of Figure 17a. The numerical load response is linear until point A_num, whereas it becomes non-linear for point between A_num and B_num. After point B_num, which corresponds to the onset of debonding, the applied load increases linearly due to the presence of friction between fiber filaments and between fibers and matrix. It should be noted that the contribution of the friction between fiber filaments is included in the $\tau_{zy} - s$

relationship of the matrix-fiber interfaces. When the residual bonded length l_r is equal to the effective bond length l_{eff} the applied load attains the peak value P^* (Figure 17a), which corresponds to the applied load value of point C_num. After that, the stress-transfer mechanism is no longer fully established, and the applied load decreases until the fiber strip is completely debonded from the matrix (point E_num). The decreasing branch of the load response, which in the experimental tests is characterized by a softening behavior, appears to be brittle in the numerical simulation. This aspect was observed in all numerical models that uses the approach described in this chapter and will be discussed in §5.9.

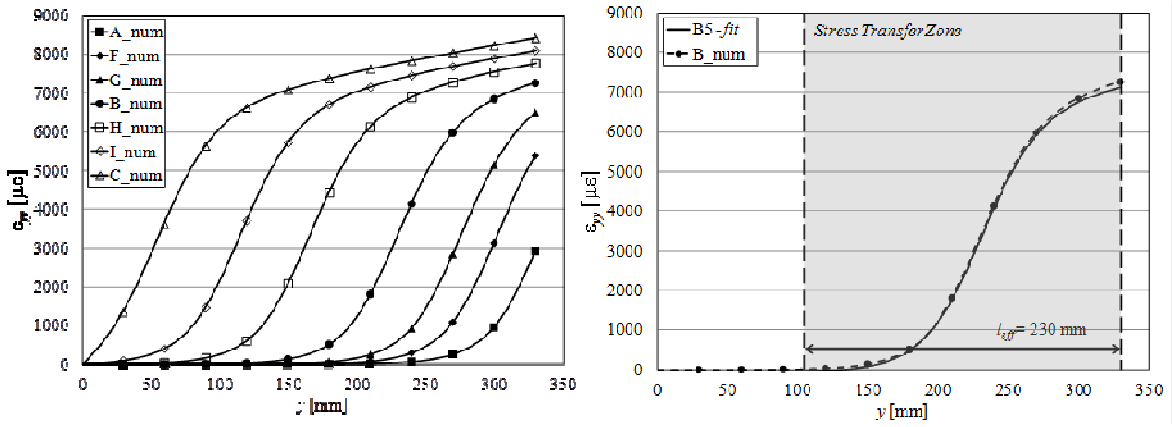

a. b.

Figure 53. a) Strain profiles along the fiber bundle length for points of the load response of Figure 52. b) Comparison between the strain profiles of point B5 (Figure 25a) and B_num (Figure 52).

The strain ε_{yy} profiles along the fiber bundle length, corresponding to points of the numerical load response of Figure 52, are depicted in Figure 53a. Figure 53a confirms the idealized strain profiles depicted in Figure 26a and can be used to compute the effective bond length l_{eff}, which is the distance between the point where the strain is nominally equal to zero and the point in which the derivative of the strain starts to be constant [25, 32]. It should be noted that the effective bond length must be evaluate for point of the load response after the onset of debonding, provided that the contribution of friction is clearly identified. Figure 53b shows the comparison between the numerical strain profile of point B_num and the experimental strain profile of point B5 (Figure 25b). It can be seen that the numerical strain profile is in good agreement with the experimental strain profile ε_{yy}. The effective length l_{eff} computed for point B_num is equal to 230 mm (Figure 53b), which is the same value obtained from the experimental test (Table 5). The propagation of debonding along the matrix-fiber interface can also be observed from the contours of the shear stress τ_{zy}, which are depicted in Figure 54 for different points of the numerical load response.

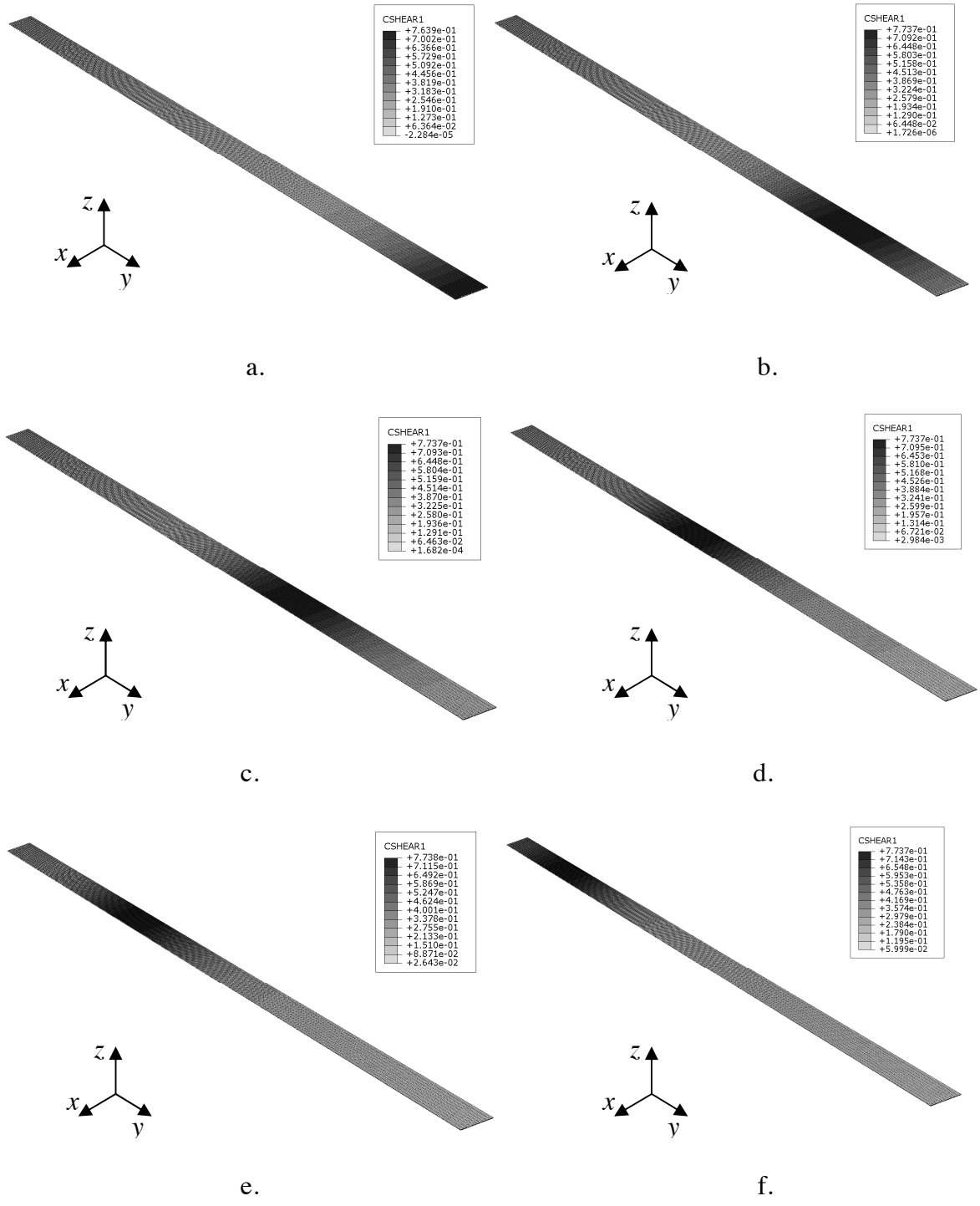

Figure 54. Shear stress contour along the fiber bundle length for points of the numerical load response (Figure 52). a) A_num. b) G_num. c) B_num. d) H_num. e) I_num. f) C_num.

For point A_num (Figure 54a) the stress-transfer mechanism is not fully established, as it can be seen by the fact that the shear stress τ_{zy} has a maximum value of 0.7639 MPa, which is lower than the maximum stress of the experimental $\tau_{zy} - s$, which is equal to

0.7738 MPa (Figure 54b-f). For point G_num (Figure 54b), the shear stress τ_{zy} attains its maximum value and, for point B_num (Figure 54c), decreases until attaining the value corresponding to friction between fiber filaments and between fibers and matrix, which means that the stress-transfer mechanism is fully established. The remaining points of Figure 54 show the debonding propagation and the displacement of the $\tau_{zy} - s$ curve toward the composite free end.

5.7 Numerical results of specimens DS_330_43_L_S_2

The experimental results of specimen DS_330_43_L_S_2 were employed for the implementation of the numerical model of a PBO FRCM-concrete joint without the external layer of matrix, termed DS_330_43_L_S_2_num. The matrix layer has length, thickness, and width of 330 mm, 4 mm, and 10 mm, respectively. The longitudinal fiber bundle is 330 mm long, 0.092 mm thick, and 5 mm wide and is placed at the center of the top longitudinal surface of the matrix layer (Figure 56). The transversal fiber bundles were not included in the model since for specimen DS_330_43_L_S_2 they were not bonded to the matrix, and their contribution to the load response is assumed negligible. The material mechanical parameters, model constraints, and applied displacement δ used are the same employed for model DS_330_43_S_5_num (§5.6).

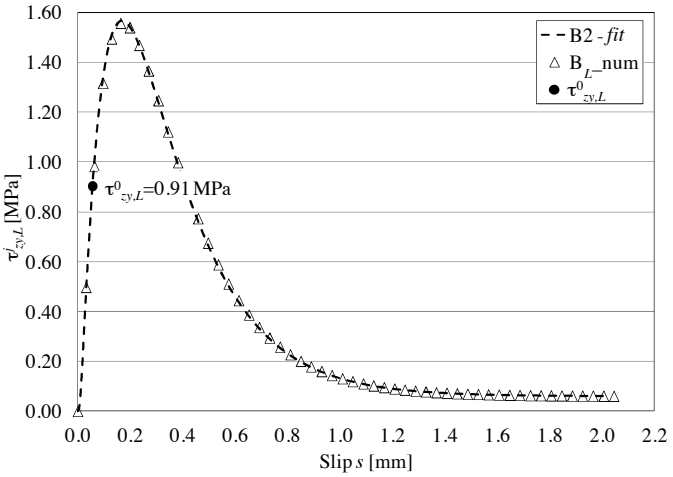

Figure 55. Comparison between the fitted and numerical shear stress vs. slip curve of point B2 (Figure 35a) and B_L_num, respectively.

The fiber matrix interface was defined by a master-slave contact, where the matrix represents the master, and the fiber represents the slave. The $\tau_{zy,L} - s_L$ curves obtained from the fracture mechanics approach applied to specimen DS_330_43_L_S_2 were used to determine the shear parameters needed to define the damage cohesive contact law that controls the master-slave interaction. The procedure used to determine the shear corresponding to the onset of damage $\tau^0_{zy,L}$ (Figure 55), the damage variable d_L,

and the corresponding non-dimensional plastic displacement $\delta_{s,L}$ is the same as that used for model DS_330_43_S_5_num ((§5.6). Both the fiber bundle and the matrix were modeled using eight-node linear brick elements. The same mesh size adopted for specimens DS_330_43_S_5_num (§5.6) was employed, which resulted in 13212 brick elements for the matrix layer and 19800 brick elements for the fiber strip (Figure 56).

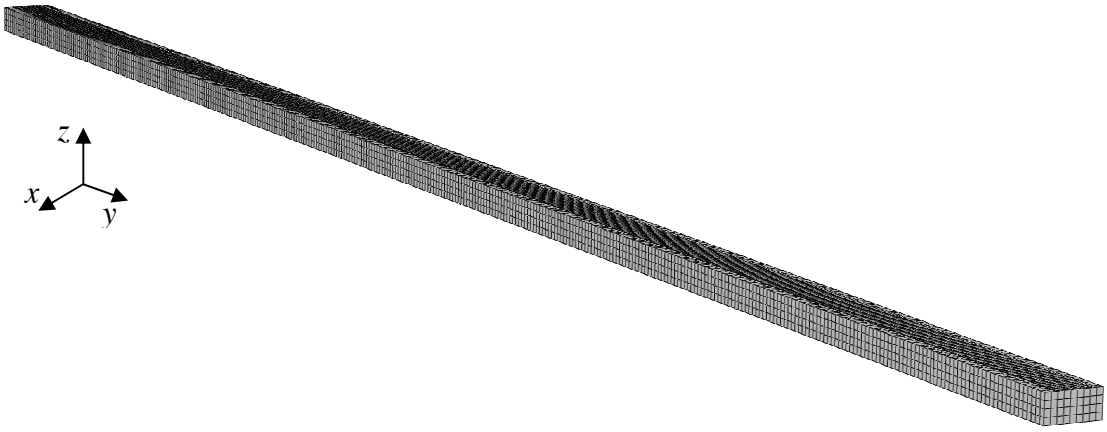

Figure 56. Mesh of model DS_330_43_L_S_2_num.

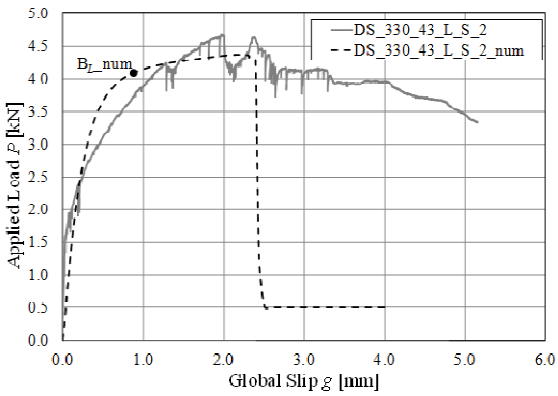

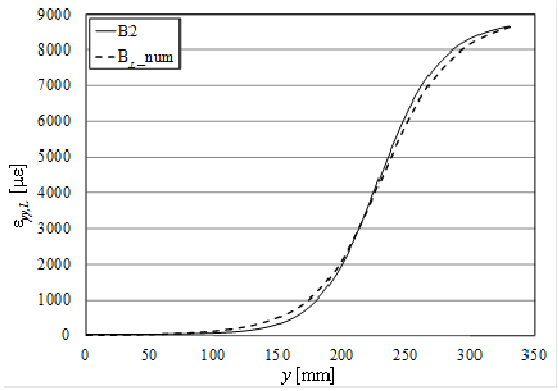

43_L_S_num.

The numerical results obtained are in reasonably good agreement with the experimental observation. Figure 57a shows the applied load – global slip responses of the experimental specimens and numerical model. The strain profiles of point B_L_num of the numerical load response depicted in Figure 57a and of point B2 of the experimental load response (Figure 35a) are shown in Figure 57b. The strain profiles of points of the numerical load response and the corresponding shear stress contour along the fiber length resemble the strain profiles and shear stress contours depicted in Figure 53a and Figure 54, respectively, and are not reported. The numerical strain $\varepsilon_{yy,L}$ profiles corresponding to points of the numerical load response (Figure 57a) is in reasonably

good agreement with the experimental strain profile curves, as shown in Figure 57b for point B_L_num.

5.8 Numerical results of multi-bundle model of specimen DS_330_43_S_5

The FRCM composites were bonded to the concrete substrate applying the internal and external matrix layer, when present, for a width b_1 equal to the width of the fiber net b_2. For this reason, the bundles placed at the edges of the composite are not completely surrounded by the matrix (Figure 48), and may have a reduced bond capacity with respect to the bundles inside the composite strip with matrix on each side. The influence of the different bond capacity of the edge bundles is more pronounced for small bonded width, whereas it becomes almost negligible as the bonded width increases (§3.10.2). In order to verify the reliability of the numerical results obtained by modeling a single fiber bundle, the results of a three-dimensional numerical model including the matrix external layer and the actual number of longitudinal bundles within the composite width, termed DS_330_43_S_5_num5, was implemented. Each matrix layer was 330 mm long, 4 mm thick and 43 mm wide. Five longitudinal fiber bundles with 5 × 0.092 mm rectangular cross-section and 330 mm length were placed between the matrix layers and were spaced at 5 mm (Figure 58). The transversal fiber bundles were not included in model DS_330_43_S_5_num5. The material mechanical parameters, model constraints, applied displacement δ, and $\tau_{zy} - s$ realtionships were the same used for model DS_330_43_S_5_num (§5.6). Both the fibers and the matrix were modeled with eight-node linear brick elements. Since a high precision of the results was not needed, the model was discretized with a coarse mesh of 11880 brick elements for the matrix and 66 brick elements for each fiber bundle (§5.6).

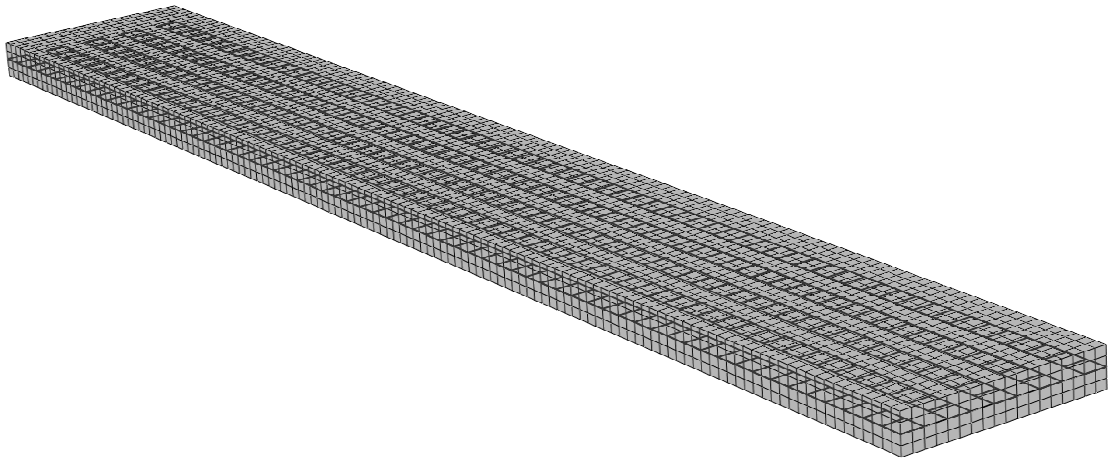

Figure 58. Mesh of model DS_330_43_S_5_num5.

Figure 59 shows the comparison between the load responses of the experimental specimen DS_330_43_S_5 and the numerical models DS_330_43_S_5_num and

DS_330_43_S_5_num5. The results obtained by the single-bundle model overlapped almost perfectly the results obtained by the multi-bundle model both for the load response and strain profiles along the fiber length. Furthermore, the strain along the lateral and central fiber bundle of model DS_330_43_S_5_num5 were equal for the same point of the load reponse (Figure 59). The results obtained with model DS_330_43_S_5_num5 confirms the reliability and precision of the single-bundle model for specimen with five or more bundles.

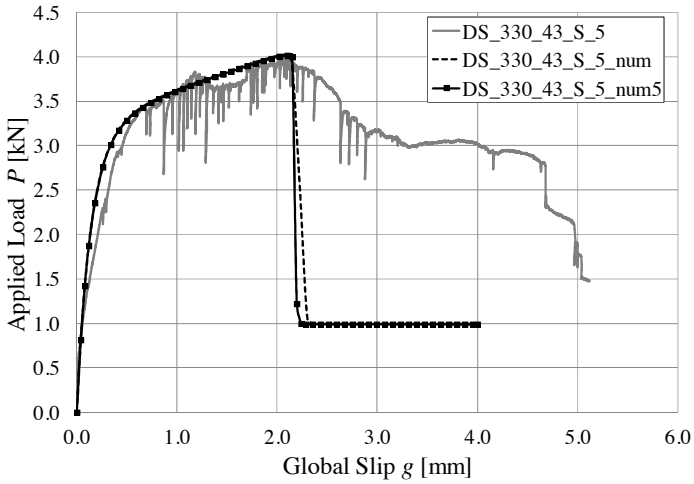

Figure 59. Load responses of specimen DS_330_43_S_5, model DS_330_43_S_5_num, and DS_330_43_S_5_num5.

5.9 Numerical post-peak behavior

After point C of Figure 17a, which corresponds to the peak load P^*, the experimental load responses of PBO FRCM-concrete joints show a gradual (softening) decrease of the applied load until the constant value P_f (point E of Figure 17a), which corresponds to friction between fiber filaments and between fibers and matrix. However, after attaining the peak value P^*, the numerical load responses depicted in Figure 52, Figure 57a, and Figure 59 show a sudden decrease of the applied load until the constant value P_f. This particular behavior of the numerical responses is mainly attributed to the solution method adopted. Indeed, all the analyses were run using a full Newton solution technique, which is not able to describe complex non-linear phenomena, such as the softening behavior that follows the peak load. Furthermore, the analyses were carried out allowing the software to automatically determine the optimum displacement increment to obtain the most rapid convergence, which results in a rapid drop from the peak load to the load associated with pure friction. Further analysis performed using different solution method and by fixing the displacement increment may be able to better reproduce the post-peak softening behavior of FRCM-concrete joints.

5.10 Conclusions

The stress-transfer mechanism of PBO FRCM-concrete joints was studied in this chapter by means of three-dimensional numerical models implemented in the software Abaqus. The results of single-lap direct-shear tests conducted on FRCM-concrete joints comprised of one layer of PBO fiber net and one or two layers of cementitious matrix were simulated. The matrix-fiber interfaces were specified by means of a damage cohesive contact behavior, whose parameters were determined according to the fracture mechanics approach applied to the experimental single-lap direct-shear tests.

The numerical results obtained are in good agreement with the experimental observations. The numerical load response well simulates the initial elastic behavior, followed by the non-linear branch corresponding to microdamaging of the matrix-fiber interfaces. After the onset of debonding the numerical load response increases linearly due to friction between fiber filaments and between fiber and matrix, as observed from the experimental results. The numerical models, however, are not able to simulate the softening behavior of the load response after the peak load since that load branch cannot be described by the Mode II fracture mechanics approach employed to define the input parameters of the models. The numerical strain profiles along the fiber strips well reproduce the strain profiles observed experimentally and can be used to determine the value of the effective bond length of PBO FRCM composites. The use of a reduced numerical model that includes a single fiber bundle and the embedding matrix, the results of which were multiplied by the number of bundles of the corresponding experimental test, was shown to be accurate in simulating the response of specimen with five or more bundles. The numerical modeling presented may be used to study the response of PBO FRCM-concrete joints with more than two layers of matrix.

6 CONCLUSIONS

The bond behavior of fiber reinforced polymer (FRP) composites and fiber reinforced cementitious matrix (FRCM) composites applied to reinforced concrete (RC) structures is investigated in this thesis.

A thorough review of the scientific literature available regarding FRP composites was carried out, and a fracture mechanics approach was employed to investigate the stress-transfer mechanism between the FRP composite and the concrete substrate. The bond behavior of FRP-concrete joints was studied through the analysis of several analytical models for the evaluation of the bond strength available in the literature. The accuracy of each model presented in evaluating the FRP-concrete bond strength was assessed by means of a wide experimental database, which includes specimens comprised of different materials and tested using either a single-lap, double-lap, or flexural beam test set-up. A statistical analysis allowed for computing the coefficient of variation of each model distinguishing between test set-up adopted and composite material used. The results obtained showed that the accuracy of each model is strongly influenced by the test set-up employed. The analytical models are, in general, less accurate when applied to flexural beam tests rather than single- and double-lap tests. It should be noted, however, that the results obtained from flexural beam tests may be affected by several factors, such as the scale effect, that should be taken into account. In addition, the accuracy of the available models for the evaluation of the FRP effective bond length, which is the minimum length needed to fully establish the stress-transfer mechanism, was assessed. In general, the accuracy of the analytical models for the estimation of the effective bond length was good.

In the second part of this thesis, an extensive experimental campaign conducted on FRCM-concrete joints tested using the single-lap direct-shear test set-up was presented. The FRCM composite tested was comprised of one layer of polyparaphenylene benzobisoxazole (PBO) fiber net applied to the concrete substrate by means of a first (internal) layer of cementitious matrix. A second (external) layer of matrix was applied over the fibers for some specimens, whereas the fibers were left uncovered for others. The weakness of PBO FRCM-concrete joints was found to be at the matrix-fiber interface rather than within the concrete substrate, as is the case with FRP-concrete joints. Based on the experimental results, an idealized applied load – global slip response characterized by the presence of friction between fiber filaments and between matrix and fibers was put forward. Specimens with different bonded lengths and bonded widths were tested. The results showed that the width effect observed with FRP composites is not present for the entire width of the FRCM composite. The application of strain gauges on the fibers allowed for studying the strain profiles along the

composite bonded length, which were used to study the fiber-matrix stress-transfer mechanism and to investigate the presence of an effective bond length. It was observed that an effective bond length of approximately 260 mm exists for PBO FRCM composites. The fracture mechanics approach adopted for FRP-concrete joints was extended to FRCM-concrete joints. As a first attempt to study the stress transfer mechanism between the fibers and the matrix, a fracture mechanics approach was carried out assuming that the bond behavior of the external and internal layer of matrix is equal. The bond behavior of the internal and external matrix layers was studied comparing the results of specimens with the external matrix layer with specimens without the external matrix layer. The ratio between the fracture energy corresponding to the internal matrix layer and the fracture energy corresponding to the external matrix layer was found to be 2.60, which means that the internal matrix layer provides a bond strength contribution much higher than the external matrix layer. Finally, the fracture mechanics parameters computed were used to implement several numerical models that confirmed the experimental evidences and may be extended to study the bond behavior of PBO FRCM composites comprised of more than two layers of matrix.

REFERENCES

1. Abaqus 6.10 Extended Functionality Online Documentation (generated September 29, 2010).
2. Abdel Baky H, Ebead UA, Neale KW. Nonlinear micromechanics-based bond-slip model for FRP/concrete interfaces. Eng Struct 2012;39:11-23.
3. Achintha PMM, Burgoyne CJ. Fracture mechanics of plate debonding. J Compos Constr ASCE 2008. 12(4):396-404.
4. Achintha PMM, Burgoyne CJ. Fracture mechanics of plate debonding: validation against experiment. Constr Build Mater 2011. 25(6):2961-71.
5. ACI 318M-05. Building code requirements for structural concrete and commentary. American Concrete Institute, Farmington Hills, Mich., 2005.
6. ACI 440.2R-08. Guide for the design and construction of externally bonded FRP system for strengthening concrete structures. American Concrete Institute, Farmington Hill, Mich., 2008.
7. Adhikary BB, Mutsuyoshi H. Study on the bond between concrete and externally bonded CFRP sheet. In: Proceedings of the 6th international symposium on fiber reinforced polymer reinforcement for concrete structures, FRPRCS-5, Cambridge, UK, 2001;1:371-78.
8. Ahmed A, Kodur VKR. Effect of bond degradation on fire resistance of FRP-strengthened reinforced concrete beams. Compos - Part B: Eng 2011;42:266-37.
9. Ahmed O, Van Gemert D, Vanderwalle L. Improved model for plate end shear of CFRP strengthened RC beams. Cem Concr Compos 2001;23(1):3-19.
10. Alam MS, Kanakubo T, Yasojima A. Shear-peeling bond strength between continuous fiber sheer and concrete. ACI Struct J 2012;109(1):75-82.
11. Ali-Ahmad M, Subramaniam KV, Ghosn M. Analysis of scaling and instability in FRP-concrete shear debonding for beam-strengthening applications. J Eng Mech 2007;133(1):58-67.
12. Ali-Ahmad M, Subramaniam KV, Ghosn M. Experimental investigation and fracture analysis of debonding between concrete and FRP. J Eng Mech 2006;132(9):914-23.
13. ASTM. Standard test method for compressive strength for cylindrical concrete specimens. C39/C39M-12, ASTM International 2011, 7 pages.
14. ASTM. Standard test method for splitting tensile strength of cylindrical concrete specimens. C496/C496M ASTM International 2011, 5 pages.
15. ASTM. Standard test method for tensile properties of polymer matrix composite materials. D3039/D3039M, ASTM International 1996, 6 pages.
16. Banholzer B. Bond behavior of multi-filament yarn embedded in a cementitious matrix, PhD Thesis, RETH Aachen University, Aachen. UK, 2004.
17. Bazant ZP, Planas J. Fracture and size effect in concrete and other quasi brittle materials. Boca Raton, Florida, CRC Press, 1997.

18. Bizindavyi L, Neale KW. Transfer lengths and bond strengths for composites bonded to concrete. J Compos Constr ASCE 1999;3(4):153-60.
19. Blanksvärd T, Täljsten B, Carolin A. Shear strengthening of concrete structures with the use of mineral-based composites. J Compos Constr, ASCE 2009;13(1):25-34.
20. Blanksvärd T. Strengthening of concrete structures by the use of mineral based composites. Licentiate thesis, Luleå Univ. of Technology, Luleå, Sweden; 2007.
21. Bournas DA, Triantafillou TC, Zygouris K, Stavropoulos F. Textile-reinforced mortar versus FRP jacketing in seismic retrofitting of RC columns with continuous or lap-spliced deformed bars. J Compos Constr, ASCE 2009;13(5):360-71.
22. Camli US, Binici B. Strength of carbon fiber reinforced polymers bonded to concrete and masonry. Constr Build Mater 2007;21:1431-46.
23. Carloni C, Subramaniam K. Investigation of sub-critical fatigue crack growth in FRP/concrete cohesive interface using digital image analysis. Compos - Part B: Eng 2013;51:35-43.
24. Carloni C, Subramaniam KV, Savoia M, Mazzotti C. Experimental determination of FRP-concrete cohesive interface properties under fatigue loading. Compos Struct 2012;94:1288-96.
25. Carloni C, Subramaniam KV. Application of fracture mechanics to debonding of FRP from RC members. ACI SP-286, Dallas, TX, 2012:10-1-10-14.
26. Carloni C, Subramaniam KV. Direct determination of cohesive stress transfer during debonding of FRP from concrete. Compos Struct 2010;93(1):184-92.
27. Carloni C. Analysing bond characteristics between composites and quasi-brittle substrates in the repair of bridges and other concrete structures. In: Advanced composites in bridge construction, edited by Kim. Publisher: Woodhead Publishing Ltd, Cambridge, UK.
28. Carrara P, Ferretti D, Freddi F, Rosati G. Shear tests of carbon fiber plates bonded to concrete with control of snap-back. Eng Fract Mech 2011;79:2663-78.
29. Carrara P, Ferretti D. A finite-difference model with mixed interface laws for shear tests of FRP plates bonded to concrete. Compos - Part B: Eng 2013;54:329-42.
30. Ceroni F, Pecce M. Evaluation of bond Strength in concrete element externally reinforced with CFRP sheets and anchoring devices. J compos Constr ASCE 2010;14(5):521-30.
31. Chajes MJ, Finch WW, Januszka TF, Thomson TA. Bond and force transfer of composite material plates bonded to concrete. ACI Struct J 1996;93(2):208-17.
32. Chen JF, Teng JG. Anchorage strength models for FRP and steel plates bonded to concrete. J Struct Eng, ASCE 2001;127(7):784-91.
33. Chen JF, Teng JG. Shear capacity of FRP strengthened RC beams: FRP debonding. Constr Build Mater 2003;17(1):27-41.
34. Chen JF, Yang ZJ, Holt GD. FRP or steel plate-to-concrete bonded joints: effect of test methods on experimental bond strength. Steel Compos Struct 2001;1(2):231–44.

35. CNR-DT 200 R1/2013. Istruzioni per la progettazione, l'esecuzione ed il controllo di interventi di consolidamento statico mediante l'utilizzo di compositi fibrorinforzati. Consiglio Nazionale delle Ricerche, Rome, Italy, 2013.
36. CNR-DT 200/2004. Instructions for design, execution and control of strengthening interventions through fiber-reinforced composites. Consiglio Nazionale delle Ricerche, Rome, Italy, 2004.
37. Cosenza E, Manfredi G, Realfonzo R. Behavior and modeling of bond of FRP rebars to concrete. J Compos Constr, ASCE 1997;1(2):40-51.
38. Czaderski C, Soudki K, Motavalli M. Front and side view image correlation measurements on FRP to concrete pull-off bond tests. J Compos Constr ASCE 2010;14(4):451-63.
39. D'Ambrisi A, Feo L, Focacci F. Bond-slip relations for PBO-FRCM materials externally bonded to concrete. Compos - Part B: Eng 2012;43(8):2938-49.
40. D'Ambrisi A, Focacci F. Flexural strengthening of RC beams with cement based composites. J Compos Constr, ASCE 2009;15(2):707-20.
41. Dai J, Ueda T, Sato Y. Unified analytical approaches for determining shear bond characteristics of FRP-concrete interfaces through pullout test. J Adv Concr Tech 2006;4:133-45.
42. D'Ambrisi A, Feo L, Focacci F. Experimental analysis on bond between PBO-FRCM strengthening materials and concrete. Compos - Part B: Eng 2013;44(1):524-32.
43. Davalos JF, Kodkani SS, Ray I. Fracture mechanics method for Mode-I interface evaluation of FRP bonded to concrete substrates. J Mater Civ Eng 2006;18(5):732-42.
44. De Lorenzis L, Miller B, Nanni A. Bond of fiber-reinforced polymer laminates to concrete. ACI Mater J 2001;98(3):256-64.
45. EN 1992-1-1 2004. Eurocode 2: Design of concrete structures - Part 1-1: general rules and rules for buildings. CEN, Comité Européen de Normalisation, Brussels, Belgium, 2004.
46. Fanning PJ, Kelly O. Ultimate response of RC beams strengthened with CFRP plates. J Compos Constr ASCE 2001;5(2):122-7.
47. Ferracuti B, Savoia M, Mazzotti C. Interface law for FRP-concrete delamination. Compos Struct 2008;80(4):523-31.
48. *fib* Bulletin 14. Externally bonded FRP reinforcement for RC structures. Fédération Internationale du Béton, Lausanne, Switzerland, 2001.
49. Focacci F, Nanni A, Bakis CE. Local bond-slip relationship for FRP reinforcement in concrete. J Compos Constr ASCE 2000;4(1):24-31.
50. Garden HN, Hollaway LC. An experimental study of the influence of plate end anchorage of carbon fibre composite plates used to strengthen reinforced concrete beams. Compos Struct 1998;42:175-88.

51. Grace C, Yang Y, Sneed LH. Fracture mechanics approach to predicting the behavior of reinforced concrete members with externally-bonded fiber reinforced polymer laminates. ACI SP-286, Dallas, TX, 2012:7-1–7-20.
52. Grelle SV, Sneed LH. Review of anchorage systems for externally-bonded FRP laminates. Int J Concr Struct Mater 2013;7(1):17-33.
53. Gunes O, Buyukozturk O, Karaca E. A fracture-based model for FRP debonding in strengthened beams. Eng Fract Mech 2009;76:1897-909.
54. Gunes O. A fracture based approach to understanding debonding in FRP bonded structural members. PhD Thesis, Massachusetts Institute of Technology, Cambridge, MA, 2004.
55. Han M. Fracture mechanics based-model of FRP sheets-concrete interface bond. Phd Thesis, The University of Alabama in Huntsville, Huntsville, AL, 2009.
56. Hartig J, Häußler-Combe U, Schicktanz K. Influence of bond properties on the tensile behaviour of textile reinforced concrete. Cem Concr Comp 2008;30:898-906.
57. Hartig J, Jesse F, Schicktanz K, Häußler-Combe U. Influence of experimental setups on the apparent uniaxial tensile load-bearing capacity of textile reinforcement concrete specimens. Mater Struct, RILEM 2011;45:433-46.
58. Hashemi S, Al-Mahaidi R. Experimental and finite element analysis of flexural behavior of FRP-strengthened RC beams using cement-based adhesives. Constr Build Mater 2012;26:268-73.
59. He R, Grelle S, Sneed LH, Belarbi A. Rapid repair of a severely damaged RC column having fractured bars using externally bonded CFRP. Compos Struct 2013;101:225-42.
60. He R, Sneed LH, Belarbi A. Rapid repair of severely damaged RC columns with different damage conditions – An experimental study. Int J Concr Struct Mater 2013;7(1):35-50.
61. Hearing BF. Delamination of reinforced concrete retrofitted with fiber reinforced plastics. PhD Thesis, Massachusetts Institute of Technology, Cambridge, MA, 2000.
62. Hilleborg A, Modéer M, Peterson PE. Analysis of crack formation and crack growth in concrete by means of fracture mechanics and finite elements. Cem Concr Res 1976;6:773-82.
63. Hiroyuki Y, Wu Z. Analysis of debonding fracture properties of CFS strengthened member subject to tension. In: Proceedings of 3rd international symposium on non-metallic (FRP) reinforcement for concrete structures 1997;1:284-94.
64. Japan Concrete Institute (JCI). Technical report of technical committee on retrofit technology. In: Proceedings of the international symposium on latest achievement of technology and research on retrofitting concrete structures, 2003.
65. Johansson T, Täljsten B. End peeling of mineral based CFRP strengthened concrete structures – A parametric study. In: Proceedings of the international symposium on bond behaviour of FRP in structures (BBFS 2005); 2005;197-204.

66. Khalifa A, Gold WJ, Nanni A, Abdel Aziz MI. Contribution of externally bonded FRP to shear capacity of RC flexural members. J Compos Constr ASCE 1998;2(4):195-202.
67. Lam L, Teng JG. Design-oriented stress-strain model for FRP-confined concrete. Constr Build Mater 2003;17(6-7):471-89.
68. Leung CKY, Yang Y. Energy-based modeling approach for debonding of FRP pòate from concrete substrate. J Eng Mech, ASCE 2006;132(6):583-93.
69. Liu K, Wu YF. Analytical identification of bond-slip relationship of EB-FRP joints. Compos - Part B: Eng 2012;43:1955-63.
70. Lu XZ, Teng JG, Ye LP, Jiang JJ. Bond-slip models for FRP sheets/plates bonded to concrete. Eng Struct 2005;27:920-37.
71. Martinelli E, Czaderski C, Montavalli M. Modeling in-plane and out-of-plane displacement fields in pull-off tests FRP strips. Eng Struct 2011;33(12):3715-25.
72. Mazzotti C, Savoia M, Ferracuti B. An experimental study on delamination of FRP plates bonded to concrete. Constr Build Mater 2008;22:1409-21.
73. Mazzucco G, Salomoni VA, Majorana CE. Three-dimensional contact-damage coupled modeling of FRP reinforcements - simulation of the delamination and long term process. Comp Struct 2012;110-111:15-31.
74. Nakaba K, Kanakubo T, Furuta T, Yoshizawa H. Bond behaviour between fiber-reinforced polymer laminates and concrete. ACI Struct J 2001;98(3):359-67.
75. Neubauer U, Rostasy FS. Bond failure of concrete fiber reinforced polymer plates at inclined cracks – experiments and fracture mechanics model. In: Proceedings of the 4th international symposium: non-metallic (FRP) reinforcement for concrete structures. ACI SP-188, Baltimore, MD, 1999:369-82.
76. Neubauer U, Rostàsy FS. Design aspects of concrete structures strengthened with externally bonded FRP plates. In: Proceedings of 7th international conference on structural faults and repairs. Edinburgh, UK, 1997;2:109–18.
77. Nguyen DM, Chan TK, Cheong HK. Brittle failure and bond development length of CFRP-concrete beams. J Compos Constr ASCE 2001;5(1):12-7.
78. Ombres L. Confinement effectiveness in concrete strengthened with fiber reinforced cement based composite jackets. In: Proceedings of the 8th international symposium on fiber reinforced polymer reinforcement for concrete structures, FRPRCS-8, Patras, GR, 2007.
79. Ombres L. Debonding analysis of reinforced concrete beams strengthened with fibre reinforced cementitious mortar. Eng Fract Mech 2012;81:94-109.
80. Orosz K, Täljsten B, Fischer G. CFRP strengthening with mineral based composites loaded in shear. In: Proceedings of the 8th international symposium on fiber reinforced polymer reinforcement for concrete structures, FRPRCS-8, Patras, GR, 2007.
81. Peled A. Confinement of damaged and nondamaged structural concrete with FRP and TRC sleeves. J Compos Constr, ASCE 2007;11(5):514-22.

82. Pellegrino C, Majorana E, Modena C. FRP strengthening of steel and steel-concrete composite structures: an analytical approach. Mater Struct 2009;42(3):353-63.
83. Pellegrino C, Modena C. An experimentally based analytical model for shear capacity of FRP strengthened reinforced concrete beams. Mech Compos Mater 2008;44(3):231-44.
84. Pellegrino C, Modena C. Analytical model for FRP confinement of concrete columns with and without internal steel reinforcement. J Compos Constr ASCE 2010;14(6):693-705.
85. Pellegrino C, Modena C. Flexural strengthening of real-scale RC and PRC beams with end-anchored pre-tensioned FRP laminates. ACI Struct J 2009;106(3):319-28.
86. Pellegrino C, Modena C. FRP shear strengthening of RC beams with transverse steel reinforcement. J Compos Constr ASCE 2002;6(2):104-11.
87. Pellegrino C, Modena C. FRP shear strengthening of RC beams: experimental study and analytical modelling. ACI Struct J 2006;103(5):720-8.
88. Pellegrino C, Modena C. Influence of axial rigidity on FRP-concrete behavior between concrete and FRP reinforcement. Adv Struct Eng 2009;12(5):639-49.
89. Pellegrino C, Tinazzi D, Modena C. Experimental study on bond behavior between concrete and FRP reinforcement. J Compos Constr ASCE 2008;12(2):180-89.
90. Pellegrino C, Vasic M. Assessment of design procedures for the use of externally bonded FRP composites in shear strengthening of reinforced concrete beams. Compos - Part B: Eng 2013; 45(1):727-41.
91. Rahimi H, Hutchinson A. Concrete beams strengthened with externally bonded FRP plates. J Compos Constr ASCE 2001;5(1):44-56.
92. Rosenboom O, Rizkalla S. Modeling of IC debonding of FRP-strengthened concrete flexural members. J Compos Constr ASCE 2008;12(2):168-79.
93. Ruredil. X mesh gold data sheet. Ruredil S.p.A 2009, Milan, Italy. http://english.ruredil.it/SchedeProdottoENG/RuredilXMeshGOLD_ing_1.pdf
94. Saadatmanesh H, Malek AM. Design guidelines for flexural strengthening of RC beams with FRP plates. J Compos Constr ASCE 1998;2(4):158-64.
95. Salomoni VA, Mazzucco G, Pellegrino C, Majorana CE. Three-dimensional modelling of bond behaviour between concrete and FRP reinforcement. Eng Comput 2011;28(1):5-29.
96. Sebastian W. Significance of midspan debonding failure in FRP-plated concrete beams. J Struct Eng 2001;127(1):792-8.
97. Smith ST, Teng JG. FRP-strengthened RC beams-II: assessment of debonding strength models. Eng Struct 2002;24(4):397-417.
98. Subramaniam KV, Carloni C, Nobile L. An understanding of the width effect in FRP-concrete debonding. Strain 2011;47:127-37.
99. Subramaniam KV, Carloni C, Nobile L. Width effect in the interface fracture during debonding of FRP sheets from concrete. Eng Fract Mech 2007;74(4):578-94.
100. Sutton MA, Orteu JJ, Shreier HW. Image correlation for shape, motion and deformation measurements. Springer , New York, 2009.

101. Sutton MA, Wolters WJ Peters WH, Ranson WF, McNeill SR. Determination of displacements using an improved digital correlation method. Image Vis Comput 1983;1(3):133-9.
102. Täljsten B, Blanksvärd T. Mineral based bonding of carbon FRP to strengthen concrete structures. J Compos Constr, ASCE 2007;11(2):120–8.
103. Taljsten B. Defining anchor lengths of steel and CFRP plates bonded to concrete. Inter J Adhes Adhes 1997;17(4):319-27.
104. Taljsten B. Strengthening of concrete prism using the plate-bonding technique. Inter J Fract 1996;82:253-66.
105. Teng JG, Smith ST, Yao J, Chen JF. Intermediate crack-induced in RC beams and slabs. Constr Build Mater 2003;17:447-62.
106. Toutanji H, Deng Y. Comparison between organic and inorganic matrices for RC beams strengthened with carbon fiber sheets. J Compos Constr, ASCE 2007;11(5):507-13.
107. Toutanji H, Saxena P, Zhao L, Ooi T. Prediction of interfacial bond failure of FRP-Concrete surface. J Compos Constr ASCE 2007;11(4):427-36.
108. Toyobo. Zylon© (PBO fiber) technical information. Toyobo Co 2005, Ltd, Osaka, Japan. http://www.toyobo-global.com/seihin/kc/pbo/Technical_Information_2005.pdf
109. Triantafillou TC, Papanicolaou CG, Zissinopoulos P, Laourdekis T. Concrete confinement with textile-reinforced mortar jackets. ACI Struct J 2006;103(1):28–37.
110. Triantafillou TC. Shear strengthening of reinforced concrete beams using epoxy-bonded FRP composites. ACI Struct J 1998;95(2):107-15.
111. Valluzzi MR, Grinzato E, Pellegrino C, Modena C. IR thermography for interface analysis of FRP laminates externally bonded to RC beams. Mater Struct 2009;42(1):25-34.
112. Van Gemert D. Force transfer in epoxy-bonded steel–concrete joints. Int J Adhes Adhes 1980;1:67-72.
113. Wan B, Sutton MA, Petrou MF, Harries KA, Li N. Investigation on bond between fiber reinforced polymer and concrete undergoing global mixed mode I/II loading. J Eng Mech 2004;130(12):1467-75.
114. Wiberg A. Strengthening of concrete beams using cementitious carbon fibre composites. PhD thesis, Royal Institute of Technology, Stockholm, SW, 2003.
115. Wu YF, Xu XS, Sun JB, Jiang C. Analytical solution for the bond strength of externally bonded reinforcement. Compos Struct 2012;94:3232-939.
116. Wu ZS, Niu H. Prediction of crack-induced debonding failure in R/C structures flexurally strengthened with externally bonded FRP composites. Doboku Gakkai Ronbunshuu E 2007;63(4):620-39.
117. Wu ZS, Yuan H, Niu H. Stress transfer and fracture propagation in different kinds of adhesive joints. J Eng Mech, ASCE 2002;128(5):562-73.
118. Yao J, Teng JG, Chen JF. Experimental study on FRP-to-concrete bonded joints. Compos - Part B: Eng 2005;36:99-113.

119. Yuan H, Wu Z, Yoshizawa H. Theoretical solution on interfacial stress transfer of externally bonded steel/composite laminates. Struct Eng/Earth Eng 2001;18(1):27-39.
120. Zhou YW, Wu YF, Yun Y. Analytical modeling of the bond-slip relationship at FRP-concrete interfaces for adhesively-bonded joints. Compos - Part B: Eng 2010;41:423-33.

APPENDIX A. TEST DATABASE

The geometrical and mechanical characteristics of the tested specimens included in the database are reported in the following tables. Single-lap and double-lap direct-shear tests are included in Table A.1 and Table A.2, respectively. The characteristic of the RC beams tested in bending are shown in Table A.3, whereas Table A.4 report the corresponding characteristics of the FRP strengthening used. The following notation is adopted:

FRP = strengthening material preparation, C_S = carbon post-impregnated sheets, G_S = glass post-impregnated sheets, C_L = carbon pre-impregnated laminates, G_L = glass pre-impregnated laminates; f_f = FRP tensile strength; n_f = number of FRP layers; t_f = thickness of one FRP layer; P_u = experimental maximum load; h = height of the RC beam; A_s = area of the reinforcing steel in tension; A'_s = area of the reinforcing steel in compression; d_s = depth of the reinforcing steel in tension; d'_s = depth of the reinforcing steel in compression; f_y = yielding strength of the steel in tension; f'_y = yielding strength of the steel in compression. All the remaining symbols were explained into the text.

Table A.1. Geometrical and mechanical characteristics of the specimens tested using single-lap direct-shear test set-up.

Reference	Specimen name	Concrete		FRP strengthening							Test results	
		b [mm]	f_c [MPa]	FRP	n_f	t_f [mm]	b_f [mm]	l_b [mm]	E_f [MPa]	f_f [MPa]	P_u [kN]	l_e [mm]
[18]	BN6	150	34.50	G_S	1	1.000	25.4	180.0	29200	472	11.41	75
	BN20	150	34.50	G_S	2	2.000	25.4	320.0	29200	472	21.40	100
	BN25	150	34.50	C_S	1	0.330	25.4	160.0	75700	1014	8.50	55
	BN32	150	34.50	C_S	2	0.660	25.4	320.0	75700	1014	15.10	70
[32]	C1	228.6	36.1	G_L	1	1.016	25.4	76.2	1084708	1655	8.46	-
	C2	228.6	47.1	G_L	1	1.016	25.4	76.2	108470	1655	9.93	-
	C3	228.6	47.1	G_L	1	1.016	25.4	76.2	108470	1655	10.64	-
	C4	228.6	47.1	G_L	1	1.016	25.4	76.2	108470	1655	10.64	-
	C5	228.6	43.6	G_L	1	1.016	25.4	76.2	108470	1655	10.53	-
	C6	228.6	43.6	G_L	1	1.016	25.4	76.2	108470	1655	8.96	-
	C7	228.6	43.6	G_L	1	1.016	25.4	76.2	108470	1655	9.61	-
	C8	228.6	43.6	G_L	1	1.016	25.4	76.2	108470	1655	10.52	-
	C9	228.6	43.6	G_L	1	1.016	25.4	76.2	108470	1655	11.20	-
	C10	228.6	24	G_L	1	1.016	25.4	76.2	108470	1655	9.87	-
	C11	228.6	28.9	G_L	1	1.016	25.4	76.2	108470	1655	9.34	-
	C12	228.6	43.7	G_L	1	1.016	25.4	76.2	108470	1655	11.20	-
	C13	228.6	36.4	G_L	1	1.016	25.4	50.8	108470	1655	8.09	-
	C14	228.6	36.4	G_L	1	1.016	25.4	101.6	108470	1655	12.81	-
	C15	152.4	36.4	G_L	1	1.016	25.4	152.4	108470	1655	11.92	-

Reference	Specimen name	Concrete		FRP	n_f	FRP strengthening					Test results	
		b [mm]	f_c [MPa]			t_f [mm]	b_f [mm]	l_b [mm]	E_f [MPa]	f_f [MPa]	P_u [kN]	l_e [mm]
	C16	152.4	36.4	G_L	1	1.016	25.4	203.2	108470	1655	11.57	-
	C100 50A	200	54.15*	C_L	1	1.250	50	100.0	170000	2497	17.30	-
	C200 50A	200	59.84*	C_L	1	1.250	50	200.0	170000	2497	27.50	-
	C300 50A	200	65.82*	C_L	1	1.250	50	300.0	170000	2497	35.10	-
	C400 50A	200	65.82*	C_L	1	1.250	50	400.0	170000	2497	26.90	-
[118]	I-1	150	23.0	C_S	1	0.165	25	75.0	256000	4114	4.75	-
	I-2	150	23.0	C_S	1	0.165	25	85.0	256000	4114	5.69	-
	I-3	150	23.0	C_S	1	0.165	25	95.0	256000	4114	5.76	-
	I-4	150	23.0	C_S	1	0.165	25	95.0	256000	4114	5.76	-
	I-5	150	23.0	C_S	1	0.165	25	95.0	256000	4114	6.17	-
	I-6	150	23.0	C_S	1	0.165	25	115.0	256000	4114	5.96	-
	I-7	150	23.0	C_S	1	0.165	25	145.0	256000	4114	5.95	-
	I-8	150	23.0	C_S	1	0.165	25	190.0	256000	4114	6.68	-
	I-9	150	23.0	C_S	1	0.165	25	190.0	256000	4114	6.35	-
	I-10	150	23.0	C_S	1	0.165	25	95.0	256000	4114	6.17	-
	I-11	150	23.0	C_S	1	0.165	25	75.0	256000	4114	5.72	-
	I-12	150	23.0	C_S	1	0.165	25	85.0	256000	4114	6.00	-
	I-13	150	23.0	C_S	1	0.165	25	95.0	256000	4114	6.14	-
	I-14	150	23.0	C_S	1	0.165	25	115.0	256000	4114	6.19	-
	I-15	150	23.0	C_S	1	0.165	25	145.0	256000	4114	6.27	-
	I-16	150	23.0	C_S	1	0.165	25	190.0	256000	4114	7.03	-
	II-1	150	22.9	C_S	1	0.165	25	95.0	256000	4114	5.20	-
	II-2	150	22.9	C_S	1	0.165	25	95.0	256000	4114	6.75	-
	II-3	150	22.9	C_S	1	0.165	25	95.0	256000	4114	5.51	-
	II-4	150	22.9	C_S	1	0.165	25	190	256000	4114	7.02	-
	II-5	150	22.9	C_S	1	0.165	25	190.0	256000	4114	7.07	-
	II-6	150	22.9	C_S	1	0.165	25	190.0	256000	4114	6.98	-
	III-1	150	27.1	C_S	1	0.165	25	100.0	256000	4114	5.94	-
	III-2	150	27.1	C_S	1	0.165	50	100.0	256000	4114	11.66	-
	III-3	150	27.1	C_S	1	0.165	75	100.0	256000	4114	14.63	-
	III-4	150	27.1	C_S	1	0.165	100	100.0	256000	4114	19.07	-
	III-5	100	27.1	C_S	1	0.165	85	100.0	256000	4114	15.08	-
	III-6	100	27.1	C_S	1	0.165	100	100.0	256000	4114	15.75	-
	III-7	100	27.1	G_L	1	1.270	25.3	100.0	22500	351	4.78	-
	III-8	100	27.1	G_L	1	1.270	50.6	100.0	22500	351	8.02	-
	IV-1	150	18.9	C_S	1	0.165	25	95.0	256000	4114	5.86	-
	IV-2	150	18.9	C_S	1	0.165	25	95.0	256000	4114	5.90	-
	IV-3	150	19.8	C_S	1	0.165	25	95.0	256000	4114	5.43	-
	IV-4	150	19.8	C_S	1	0.165	25	95.0	256000	4114	5.76	-
	IV-5	150	18.9	C_S	1	0.165	25	95.0	256000	4114	5.00	-
	IV-6	150	19.8	C_S	1	0.165	25	95.0	256000	4114	7.08	-
	IV-7	150	18.9	C_S	1	0.165	25	95.0	256000	4114	5.50	-
	IV-8	150	19.8	C_S	1	0.165	25	95.0	256000	4114	5.93	-
	IV-9	150	18.9	C_S	1	0.165	25	95.0	256000	4114	5.38	-

Reference	Specimen name	Concrete		FRP	n_f	FRP strengthening					Test results	
		b [mm]	f_c [MPa]			t_f [mm]	b_f [mm]	l_b [mm]	E_f [MPa]	f_f [MPa]	P_u [kN]	l_e [mm]
	IV-10	150	19.8	C_S	1	0.165	25	95.0	256000	4114	6.60	-
	IV-11	150	18.9	C_S	1	0.165	25	95.0	256000	4114	5.51	-
	IV-12	150	19.8	C_S	1	0.165	25	95.0	256000	4114	5.67	-
	IV-13	150	18.9	C_S	1	0.165	25	95.0	256000	4114	6.31	-
	IV-14	150	19.8	C_S	1	0.165	25	95.0	256000	4114	6.19	-
	V-1	150	21.1	C_S	1	0.165	15	95.0	256000	4114	3.81	-
	V-2	150	21.1	C_S	1	0.165	15	95.0	256000	4114	4.41	-
	V-3	150	21.1	C_S	1	0.165	25	95.0	256000	4114	6.26	-
	V-4	150	21.1	C_S	1	0.165	50	95.0	256000	4114	12.22	-
	V-5	150	21.1	C_S	1	0.165	75	95.0	256000	4114	14.29	-
	V-6	150	21.1	C_S	1	0.165	100	95.0	256000	4114	15.58	-
	V-7	100	21.1	C_S	1	0.165	80	95.0	256000	4114	14.27	-
	V-8	100	21.1	C_S	1	0.165	80	95.0	256000	4114	13.78	-
	V-9	100	21.1	C_S	1	0.165	90	95.0	256000	4114	13.56	-
	V-10	100	21.1	C_S	1	0.165	90	95.0	256000	4114	15.66	-
	V-11	100	21.1	C_S	1	0.165	100	95.0	256000	4114	15.57	-
	V-12	100	21.1	C_S	1	0.165	100	95.0	256000	4114	17.43	-
	VI-1	150	21.9	C_S	1	0.165	25	95.0	256000	4114	6.01	-
	VI-2	150	21.9	C_S	1	0.165	25	95.0	256000	4114	5.85	-
	VI-3	150	21.9	C_S	1	0.165	25	145.0	256000	4114	5.76	-
	VI-4	150	21.9	C_S	1	0.165	25	145.0	256000	4114	5.73	-
	VI-5	150	21.9	C_S	1	0.165	25	190.0	256000	4114	5.56	-
	VI-6	150	21.9	C_S	1	0.165	25	190.0	256000	4114	5.58	-
	VI-7	150	21.9	C_S	1	0.165	25	240.0	256000	4114	5.91	-
	VI-8	150	21.9	C_S	1	0.165	25	240.0	256000	4114	5.05	-
	VII-1	150	24.9	C_S	1	0.165	25	95.0	256000	4114	6.8	-
	VII-2	150	24.9	C_S	1	0.165	25	95.0	256000	4114	6.62	-
	VII-3	150	24.9	C_S	1	0.165	25	145.0	256000	4114	7.33	-
	VII-4	150	24.9	C_S	1	0.165	25	145.0	256000	4114	6.49	-
	VII-5	150	24.9	C_S	1	0.165	25	190.0	256000	4114	7.07	-
	VII-6	150	24.9	C_S	1	0.165	25	190	256000	4114	7.44	-
	VII-7	150	24.9	C_S	1	0.165	25	240.0	256000	4114	7.16	-
	VII-8	150	24.9	C_S	1	0.165	25	240.0	256000	4114	6.24	-
[70]	1-11	100	2.86	C_S	1	0.167	40	100.0	230000	3481	8.75	-
	1-12	100	2.74	C_S	1	0.167	40	100.0	230000	3481	8.85	-
	1-21	100	2.86	C_S	1	0.167	40	200.0	230000	3481	9.30	-
	1-22	100	2.74	C_S	1	0.167	40	200.0	230000	3481	8.50	-
	1-31	100	2.86	C_S	1	0.167	40	300.0	230000	3481	9.30	-
	1-32	100	2.74	C_S	1	0.167	40	300.0	230000	3481	8.30	-
	1-41	100	2.86	C_S	1	0.167	40	500.0	230000	3481	8.05	-
	1-42	100	2.86	C_S	1	0.167	40	500.0	230000	3481	8.05	-
	1-51	100	2.73	C_S	1	0.167	40	500.0	230000	3481	8.45	-
	1-52	100	2.73	C_S	1	0.167	40	500.0	230000	3481	7.30	-
	2-11	100	2.64	C_S	1	0.167	40	100.0	230000	3481	8.75	-

Reference	Specimen name	Concrete		FRP	n_f	FRP strengthening					Test results	
		b [mm]	f_c [MPa]			t_f [mm]	b_f [mm]	l_b [mm]	E_f [MPa]	f_f [MPa]	P_u [kN]	l_e [mm]
	2-12	100	2.64	C_S	1	0.167	40	100.0	230000	3481	8.85	-
	2-13	100	2.71	C_S	1	0.167	40	100.0	230000	3481	7.75	-
	2-14	100	2.71	C_S	1	0.167	40	100.0	230000	3481	7.65	-
	2-15	100	2.61	C_S	1	0.167	40	100.0	230000	3481	9.00	-
	2-21	100	2.64	C_S	1	0.334	40	100.0	230000	3481	12.00	-
	2-22	100	2.64	C_S	1	0.334	40	100.0	230000	3481	10.80	-
	2-31	100	2.64	C_S	1	0.501	40	100.0	230000	3481	12.65	-
	2-32	100	2.64	C_S	1	0.501	40	100.0	230000	3481	14.35	-
	2-41	100	2.61	C_S	1	0.165	40	100.0	373000	2942	11.55	-
	2-42	100	2.61	C_S	1	0.165	40	100.0	373000	2942	11.00	-
	2-51	100	2.71	C_S	1	0.167	40	100.0	230000	3481	9.85	-
	2-52	100	2.71	C_S	1	0.167	40	100.0	230000	3481	9.50	-
	2-61	100	2.71	C_S	1	0.167	40	100.0	230000	3481	8.80	-
	2-62	100	2.71	C_S	1	0.167	40	100.0	230000	3481	9.25	-
	2-71	100	2.71	C_S	1	0.167	40	100.0	230000	3481	7.65	-
	2-72	100	2.71	C_S	1	0.167	40	100.0	230000	3481	6.80	-
	2-81	100	3.87	C_S	1	0.167	40	100.0	230000	3481	7.75	-
	2-82	100	3.87	C_S	1	0.167	40	100.0	230000	3481	8.08	-
	2-91	100	2.61	C_S	1	0.167	40	100.0	230000	3481	6.75	-
	2-92	100	2.61	C_S	1	0.167	40	100.0	230000	3481	6.80	-
	2-101	100	2.64	C_S	1	0.111	40	100.0	230000	3481	7.70	-
	2-102	100	2.71	C_S	1	0.111	40	100.0	230000	3481	6.95	-
	NJ2	150	2.08	C_S	1	0.083	100	100.0	240000	3550	11.00	-
	NJ3	150	2.08	C_S	1	0.083	100	150.0	240000	3550	11.25	-
	NJ4	150	2.87	C_S	1	0.083	100	100.0	240000	3550	12.50	-
	NJ5	150	2.87	C_S	1	0.083	100	150.0	240000	3550	12.25	-
	NJ6	150	2.87	C_S	1	0.083	100	150.0	240000	3550	12.75	-
	Ueda_B1	500	2.64	C_S	1	0.110	100	200.0	230000	3479	20.60	-
	Ueda_B2	500	3.49	C_S	1	0.330	100	200.0	230000	3479	38.00	-
	Ueda_B3	500	3.71	C_S	1	0.330	100	200.0	230000	3479	34.10	-
	S-CFS-400-25a	100	4.21	C_S	1	0.222	40	250.0	230000	4200	15.40	-
	S-CFS-400-25b	100	4.21	C_S	1	0.222	40	250.0	230000	4200	13.90	-
	S-CFS-400-25c	100	4.21	C_S	1	0.222	40	250.0	230000	4200	13.00	-
	S-CFM-300-25a	100	4.21	C_S	1	0.167	40	250.0	390000	4400	12.00	-
	S-CFM-300-25b	100	4.21	C_S	1	0.167	40	250.0	390000	4400	11.90	-
	S-CFM-900-25a	100	4.21	C_S	1	0.500	40	250.0	390000	4400	25.90	-
	S-CFM-900-25b	100	4.21	C_S	1	0.5	40	250	390000	4400	23.40	-
	S-CFM-900-25c	100	4.21	C_S	1	0.500	40	250.0	390000	4400	23.70	-
	DLUT15-2G	150	2.50	C_S	1	0.507	20	150.0	83000	3271	5.81	-
	DLUT15-5G	150	2.50	C_S	1	0.507	50	150.0	83000	3271	10.60	-
	DLUT15-7G	150	2.50	C_S	1	0.507	80	150.0	83000	3271	18.23	-
	DLUT30-1G	150	3.22	C_S	1	0.507	20	100.0	83000	3271	4.63	-
	DLUT30-2G	150	3.22	C_S	1	0.507	20	150.0	83000	3271	5.77	-
	DLUT30-3G	150	3.22	C_S	1	0.507	50	60.0	83000	3271	9.42	-

Reference	Specimen name	Concrete		FRP	n_f	FRP strengthening					Test results	
		b [mm]	f_c [MPa]			t_f [mm]	b_f [mm]	l_b [mm]	E_f [MPa]	f_f [MPa]	P_u [kN]	l_e [mm]
	DLUT30-4G	150	3.22	C_S	1	0.507	50	100.0	83000	3271	11.03	-
	DLUT30-6G	150	3.22	C_S	1	0.507	50	150.0	83000	3271	11.80	-
	DLUT30-7G	150	3.22	C_S	1	0.507	80	100.0	83000	3271	14.65	-
	DLUT30-8G	150	3.22	C_S	1	0.507	80	150.0	83000	3271	16.44	-
	DLUT50-1G	150	3.60	C_S	1	0.507	20	100.0	83000	3271	5.99	-
	DLUT50-2G	150	3.60	C_S	1	0.507	20	150.0	83000	3271	5.90	-
	DLUT50-4G	150	3.60	C_S	1	0.507	50	100.0	83000	3271	9.84	-
	DLUT50-5G	150	3.60	C_S	1	0.507	50	150.0	83000	3271	12.28	-
	DLUT50-6G	150	3.60	C_S	1	0.507	80	100.0	83000	3271	14.02	-
	DLUT50-7G	150	3.60	C_S	1	0.507	80	150.0	83000	3271	16.71	-
	DLUT15-2C	150	2.50	C_S	1	0.330	20	150.0	207000	3890	5.48	-
	DLUT15-5C	150	2.50	C_S	1	0.330	50	150.0	207000	3890	10.02	-
	DLUT15-7C	150	2.50	C_S	1	0.330	80	150.0	207000	3890	19.27	-
	DLUT30-1C	150	3.22	C_S	1	0.330	20	100.0	207000	3890	5.54	-
	DLUT30-2C	150	3.22	C_S	1	0.330	20	150.0	207000	3890	4.61	-
	DLUT30-4C	150	3.22	C_S	1	0.330	50	100.0	207000	3890	11.08	-
	DLUT30-5C	150	3.22	C_S	1	0.330	50	100.0	207000	3890	16.10	-
	DLUT30-6C	150	3.22	C_S	1	0.330	50	150.0	207000	3890	21.71	-
	DLUT30-7C	150	3.22	C_S	1	0.330	80	100.0	207000	3890	22.64	-
	DLUT50-1C	150	3.60	C_S	1	0.330	20	100.0	207000	3890	5.78	-
	DLUT50-4C	150	3.60	C_S	1	0.330	50	100.0	207000	3890	12.95	-
	DLUT50-5C	150	3.60	C_S	1	0.330	50	150.0	207000	3890	16.72	-
	DLUT50-6C	150	3.60	C_S	1	0.330	80	100.0	207000	3890	16.24	-
	DLUT50-7C	150	3.60	C_S	1	0.330	80	150.0	207000	3890	22.80	-
	D-AR-280-30a	100	61.30	C_L	1	1.000	100	300.0	23900	4400	12.75	-
	D-AR-280-30b	100	61.30	C_L	1	1.000.	100	300.0	23900	4400	12.85	-
	D-AR-280-30c	100	61.30	C_L	1	1.000	100	300.0	23900	4400	11.90	-
[107]	I-1	200	17.00	C_S	3	0.165	50	100.0	110000	660	7.56	-
	I-2	200	17.00	C_S	4	0.165	50	100.0	110000	660	9.29	-
	I-3	200	17.00	C_S	5	0.165	50	100.0	110000	660	11.64	-
	I-4	200	17.00	C_S	6	0.165	50	100.0	110000	660	12.86	-
	II-1	200	46.00	C_S	3	0.165	50	100.0	110000	660	12.55	-
	II-2	200	46.00	C_S	4	0.165	50	100.0	110000	660	14.25	-
	II-3	200	46.00	C_S	5	0.165	50	100.0	110000	660	17.72	-
	II-4	200	46.00	C_S	6	0.165	50	100.0	110000	660	18.86	-
	III-1	200	61.50	C_S	3	0.165	50	100.0	110000	660	13.24	-
	III-2	200	61.50	C_S	4	0.165	50	100.0	110000	660	15.17	-
	III-3	200	61.50	C_S	5	0.165	50	100.0	110000	660	18.86	-
	III-4	200	61.50	C_S	6	0.165	50	100.0	110000	660	19.03	-
[30]	C150_100_1	150	21.58	C_S	1	0.165	100	150.0	230000	4800	18.97	-
	C150_100_2	150	21.58	C_S	1	0.165	100	150.0	230000	4800	16.51	-
	C150_100_3	150	21.58	C_S	1	0.165	100	150.0	230000	4800	14.26	-
	C150_100_4	150	21.58	C_S	1	0.165	100	150	230000	4800	15.10	-
	C150_100_2L_1	150	21.58	C_S	2	0.165	100	100.0	230000	4800	20.12	-

Reference	Specimen name	Concrete		FRP strengthening							Test results	
		b [mm]	f_c [MPa]	FRP	n_f	t_f [mm]	b_f [mm]	l_b [mm]	E_f [MPa]	f_f [MPa]	P_u [kN]	l_e [mm]
	C150_100_2L_2	150	21.58	C_S	2	0.165	100	100.0	230000	4800	19.87	-
	C100_100_1	150	21.58	C_S	1	0.165	100	100.0	230000	4800	13.63	-
	C100_100_2	150	21.58	C_S	1	0.165	100	100.0	230000	4800	13.36	-
	C150_50_1	150	21.58	C_S	1	0.165	50	150.0	230000	4800	9.80	-
	C150_50_2	150	21.58	C_S	1	0.165	50	150.0	230000	4800	6.00	-
	C150_50_3	150	21.58	C_S	1	0.165	50	150.0	230000	4800	7.00	-
	C150_50_2L_1	150	21.58	C_S	2	0.165	50	150.0	230000	4800	11.44	-
	C150_50_2L_2	150	21.58	C_S	2	0.165	50	150.0	230000	4800	9.97	-
	C150_50_2L_3	150	21.58	C_S	2	0.165	50	150.0	230000	4800	10.04	-
	C150_25_1	150	21.58	C_S	1	0.165	25	150.0	230000	4800	6.00	-
	C150_25_2	150	21.58	C_S	1	0.165	25	150.0	230000	4800	3.70	-
	C150_25_3	150	21.58	C_S	1	0.165	25	150.0	230000	4800	5.80	-
	C150_75_1	150	21.58	C_S	1	0.165	75	150.0	230000	4800	14.40	-
	C150_75_2	150	21.58	C_S	1	0.165	75	150.0	230000	4800	12.96	-
[99]	W-1	125	39.00	C_S	1	0.167	46	152.0	230000	3830	12.90	80
	W-2	125	39.00	C_S	1	0.167	46	152.0	230000	3830	12.05	76
	W-3	125	39.00	C_S	1	0.167	46	152.0	230000	3830	13.20	75
	W-4	125	39.00	C_S	1	0.167	38	152.0	230000	3830	10.09	81
	W-5	125	39.00	C_S	1	0.167	38	152.0	230000	3830	10.02	73
	W-6	125	39.00	C_S	1	0.167	25	152.0	230000	3830	5.54	80
	W-7	125	39.00	C_S	1	0.167	25	152.0	230000	3830	5.44	76
	W-8	125	39.00	C_S	1	0.167	25	152.0	230000	3830	5.36	69
	W-9	125	39.00	C_S	1	0.167	19	152.0	230000	3830	4.27	75
	W-10	125	39.00	C_S	1	0.167	19	152.0	230000	3830	4.05	78
[98]	Test 7	52	31.00	C_S	1	0.167	25	152.0	230000	3830	8.65	74
	Test 8	52	31.00	C_S	1	0.167	25	152.0	230000	3830	6.89	73
	Test 12	52	31.00	C_S	1	0.167	22	152.0	230000	3830	7.44	72
	Test 13	52	31.00	C_S	1	0.167	22	152.0	230000	3830	7.17	81
	DS_2	52	31.00	C_S	1	0.167	20	152.0	230000	3830	6.15	75
	DS_3	52	31.00	C_S	1	0.167	20	152.0	230000	3830	6.45	78
[24]	DS-S1	125	35.00	C_S	1	0.167	25	152.0	230000	3830	8.04	79
	DS-S2	125	35.00	C_S	1	0.167	25	152.0	230000	3830	7.74	76
	DS-S3	125	35.00	C_S	1	0.167	25	152.0	230000	3830	7.01	85
[23]	DS-ST_1	125	35.00	C_S	1	0.167	25	152.0	230000	3830	5.80	76
	DS-ST_2	125	35.00	C_S	1	0.167	25	152.0	230000	3830	6.30	72
	DS-ST_3	125	35.00	C_S	1	0.167	25	152.0	230000	3830	6.00	73

Table A.2. Geometrical and mechanical characteristics of the specimens tested using double-lap direct-shear test set-up.

Reference	Specimen name	Concrete		FRP strengthening							Test results	
		b [mm]	f_c [MPa]	FRP	n_f	t_f [mm]	b_f [mm]	l_b [mm]	E_f [MPa]	f_f [MPa]	P_u [kN]	l_e [mm]
[70]	Ueda_A1	100	2.55	C_S	1	0.110	50	75	230000	3479	6.25	-
	Ueda_A2	100	3.48	C_S	1	0.110	50	150	230000	3479	9.20	-
	Ueda_A3	100	3.48	C_S	1	0.110	50	300	230000	3479	11.95	-
	Ueda_A4	100	3.60	C_S	1	0.220	50	75	230000	3479	10.00	-
	Ueda_A5	100	3.56	C_S	1	0.110	50	150	230000	3479	7.30	-
	Ueda_A6	100	3.56	C_S	1	0.165	50	65	372000	2940	9.55	-
	Ueda_A7	100	3.57	C_S	1	0.220	50	150	230000	3479	16.25	-
	Ueda_A8	100	3.57	C_S	1	0.110	50	700	230000	3479	11.00	-
	Ueda_A9	100	3.43	C_S	1	0.110	50	150	230000	3479	10.00	-
	Ueda_A10	100	2.59	C_S	1	0.110	10	150	230000	3479	2.40	-
	Ueda_A11	100	2.59	C_S	1	0.110	20	150	230000	3479	5.35	-
	Ueda_A12	100	2.59	C_S	1	0.330	20	150	230000	3479	9.25	-
	Ueda_A13	100	2.64	C_S	1	0.550	20	150	230000	3479	11.75	-
	D-CFS-150-30a	100	3.71	C_S	1	0.083	100	300	230000	4200	12.20	-
	D-CFS-150-30b	100	4.21	C_S	1	0.083	100	300	230000	4200	11.80	-
	D-CFS-150-30c	100	4.21	C_S	1	0.083	100	300	230000	4200	12.25	-
	D-CFS-300-30a	100	4.21	C_S	1	0.167	100	300	230000	4200	18.90	-
	D-CFS-300-30b	100	4.21	C_S	1	0.167	100	300	230000	4200	16.95	-
	D-CFS-300-30c	100	4.21	C_S	1	0.167	100	300	230000	4200	16.65	-
	D-CFS-600-30a	100	4.21	C_S	1	0.333	100	300	230000	4200	25.65	-
	D-CFS-600-30b	100	4.21	C_S	1	0.333	100	300	230000	4200	25.35	-
	D-CFS-600-30c	100	4.21	C_S	1	0.333	100	300	230000	4200	27.25	-
	D-CFM-300-30a	100	4.21	C_S	1	0.167	100	300	390000	4400	19.50	-
	D-CFM-300-30b	100	4.21	C_S	1	0.167	100	300	390000	4400	19.50	-
	PG1-11	100	2.90	C_S	1	0.169	50	130	97000	2777	7.78	-
	PG1-12	100	2.90	C_S	1	0.169	50	130	97000	2777	9.19	-
	PG1-1W1	100	2.90	C_S	1	0.169	75	130	97000	2777	10.11	-
	PG1-1W2	100	2.90	C_S	1	0.169	75	130	97000	2777	13.95	-
	PG1-1L11	100	2.90	C_S	1	0.169	50	100	97000	2777	6.87	-
	PG1-1L12	100	2.90	C_S	1	0.169	50	100	97000	2777	9.20	-
	PG1-1L21	100	2.90	C_S	1	0.169	50	70	97000	2777	6.46	-
	PG1-1L22	100	2.90	C_S	1	0.169	50	70	97000	2777	6.66	-
	PG1-21	100	2.90	C_S	1	0.338	50	130	97000	2777	10.49	-
	PG1-22	100	2.90	C_S	1	0.338	50	130	97000	2777	11.43	-
	PG1-1C1	100	2.90	C_S	1	0.111	50	130	235000	3500	7.97	-
	PG1-1C2	100	2.90	C_S	1	0.111	50	130	235000	3500	9.19	-
	M1	100	40.80	C_S	1	0.110	50	75	230000	3500	5.80	-
	M2	100	40.80	C_S	1	0.110	50	150	230000	3500	9.20	-
	M3	100	43.30	C_S	1	0.110	50	300	230000	3500	11.95	-
	M4	100	42.40	C_S	1	0.165	50	75	230000	3500	10.00	-
	M5	100	42.40	C_S	1	0.165	50	150	230000	3500	7.30	-
	M6	100	42.70	C_S	1	0.220	50	65	230000	3500	9.55	-

Reference	Specimen name	Concrete		FRP	FRP strengthening						Test results	
		b [mm]	f_c [MPa]		n_f	t_f [mm]	b_f [mm]	l_b [mm]	E_f [MPa]	f_f [MPa]	P_u [kN]	l_e [mm]
[89]	M7	100	42.70	C_S	1	0.220	50	150	230000	3500	16.25	-
	M8	100	44.70	C_S	1	0.11	50	700	230000	3500	10.00	-
	S1C1a	100	55.00	C_S	1	0.165	50	200	230000	3430	19.98	72.5
	S1C5a	100	55.00	C_S	1	0.165	50	200	390000	3000	21.33	-
	S1C5b	100	55.00	C_S	1	0.165	50	200	390000	3000	16.76	-
	S1C5c	100	50.00	C_S	1	0.165	50	280	390000	3000	18.79	87.5
	S1C5d	100	50.00	C_S	1	0.165	50	200	390000	3000	12.11	65.0
	S2C1a	100	55.00	C_S	2	0.165	50	200	230000	3430	21.74	77.5
	S2C1b	100	50.00	C_S	2	0.165	50	200	230000	3430	24.67	85.0
	S2C1c	100	50.00	C_S	2	0.165	50	280	230000	3430	28.21	77.5
	S3C1a	100	55.00	C_S	3	0.165	50	200	230000	3430	28.44	106.0
	S3C1b	100	50.00	C_S	3	0.165	50	200	230000	3430	25.99	108.0
	S3C1c	100	50.00	C_S	3	0.165	50	200	230000	3430	29.33	107.5
	S2C5a	100	55.00	C_S	2	0.165	50	280	390000	3000	25.55	107.5
	S2C5b	100	50.00	C_S	2	0.165	50	200	390000	3000	27.10	100.0
	S3C5a	100	55.00	C_S	3	0.165	50	200	390000	3000	26.41	107.5
	S3C5b	100	55.00	C_S	3	0.165	50	200	390000	3000	29.73	130.0
	S3C5c	100	50.00	C_S	3	0.165	50	200	390000	3000	29.79	120.0

Table A.3. Geometrical and mechanical characteristics of the RC beams tested in bending.

Reference	Specimen name	Concrete			Steel reinforcement					
		b [mm]	h [mm]	f_c [MPa]	A_s [mm^2]	A'_s [mm^2]	d_s [mm]	d'_s [mm]	f_y [MPa]	f'_y [MPa]
[9]	AF.2	125	225	41.00	157.1	56.5	202.5	22.5	568	553
	AF.2-1	125	225	41.00	157.1	56.5	202.5	22.5	568	553
	AF.4	125	225	41.00	157.1	56.5	202.5	22.5	568	553
	DF.1	125	225	42.00	157.1	56.5	202.5	22.5	568	553
[46]	F5	155	240	80	339.3	226.2	203	37	532	532
	F6	155	240	80	339.3	226.2	203	37	532	532
	F7	155	240	80	339.3	226.2	203	37	532	532
	F8	155	240	80	339.3	226.2	203	37	532	532
	F9	155	240	80	339.3	226.2	203	37	532	532
	F10	155	240	80	339.3	226.2	203	37	532	532
[91]	A4	200	150	54.00	157.1	100.5	120	30	575	575
	A5	200	150	54.00	157.1	100.5	120	30	575	575
	A6	200	150	54.00	157.1	100.5	120	30	575	575
	A7	200	150	54.00	157.1	100.5	120	30	575	575
	A8	200	150	54.00	157.1	100.5	120	30	575	575
	A9	200	150	54.00	157.1	100.5	120	30	575	575
	A10	200	150	54.00	157.1	100.5	120	30	575	575
	A11	200	150	54.00	157.1	100.5	120	30	575	575
	B3	200	150	54.00	157.1	100.5	120	30	575	575
	B4	200	150	54.00	157.1	100.5	120	30	575	575
	B5	200	150	54.00	157.1	100.5	120	30	575	575
	B6	200	150	54.00	157.1	100.5	120	30	575	575
	B7	200	150	54.00	157.1	100.5	120	30	575	575
	B8	200	150	54.00	157.1	100.5	120	30	575	575
	C3	200	150	54.00	401.9	100.5	120	30	575	575
	C4	200	150	54.00	401.9	100.5	120	30	575	575
	C5	200	150	54.00	401.9	100.5	120	30	575	575
	C6	200	150	54.00	401.9	100.5	120	30	575	575
	C7	200	150	54.00	401.9	100.5	120	30	575	575
	C8	200	150	54.00	401.9	100.5	120	30	575	575
[97]	DF.2	125	225	46.00	151	57	193	32	568	553
	DF.3	125	225	46.00	151	57	193	32	568	553
	DF.4	125	225	46.00	151	57	193	32	568	553
	AF3	125	225	46.00	151	57	193	32	568	553
	CF2-1	125	225	46.00	151	57	193	32	568	553
	CF3-1	125	225	46.00	151	57	193	32	568	553
	CF4-1	125	225	46.00	151	57	193	32	568	553
	VR5	120	250	33.60	157	57	214	34	565	738
	VR6	120	250	33.60	157	57	214	34	565	738
	VR7	120	250	33.60	157	57	214	34	565	738
	VR8	120	250	33.60	157	57	214	34	565	738
	VR9	120	250	33.60	157	57	214	34	565	738
	VR10	120	250	33.60	157	57	214	34	565	738

Reference	Specimen name	Concrete			Steel reinforcement					
		b [mm]	h [mm]	f_c [MPa]	A_s [mm^2]	A'_s [mm^2]	d_s [mm]	d'_s [mm]	f_y [MPa]	f'_y [MPa]
	A3	150	300	51.70	792	-	250	-	427	-
	A8	150	300	51.70	792	-	250	-	427	-
	C2	150	300	51.70	792	-	250	-	427	-
	C	152	305	39.80	253	-	251	30.5	414	-
	D	152	305	39.80	253	-	251	30.5	414	-
	G	152	305	43.00	253	-	251	30.5	414	-
	I	152	305	39.80	253	-	251	30.5	414	-
	M	152	305	43.00	253	-	251	30.5	414	-
	B2	100	100	43.99	85	57	84	16	350	350
	B3	100	100	43.99	85	57	84	16	350	350
	B4	100	100	43.99	85	57	84	16	350	350
	B6	100	100	43.99	85	57	84	16	350	350
	1Au	100	100	49.05	85	57	84	16	350	350
	1Bu	100	100	49.05	85	57	84	16	350	350
	1B2u	100	100	49.05	85	57	84	16	350	350
	1Cu	100	100	49.05	85	57	84	16	350	350
	2Au	100	100	49.05	85	57	84	16	350	350
	2Bu	100	100	49.05	85	57	84	16	350	350
	2Cu	100	100	49.05	85	57	84	16	350	350
	3Au	100	100	49.05	85	57	84	16	350	350
	3Bu	100	100	49.05	85	57	84	16	350	350
	3Cu	100	100	49.05	85	57	84	16	350	350
	B1U, 2.3	130	230	39.01	236	101	206	25	556	556
	P2	150	300	40.00	308	-	257	30	500	-
	P3	150	300	40.00	308	-	257	30	500	-
	P4	150	300	40.00	308	-	257	30	500	-
	P5	150	300	40.00	308	-	257	30	500	-
	2	150	250	36.77	157	157	205	45	537	537
	4	150	250	37.60	157	157	205	45	537	537
	5	150	250	42.16	157	157	205	45	537	537
	6	150	250	41.42	157	157	205	45	537	537
	7	150	250	39.01	157	157	205	45	537	537
	B	205	455	35	1013	253	400	55	456	456
	SB1	200	300	53.12	402	402	252	48	527	527
	SB2	200	300	53.95	402	402	252	48	527	527
	SB3	200	300	53.95	402	402	252	48	527	527
	MB1	200	300	58.10	402	402	252	48	527	527
	HB1	200	300	58.10	402	402	252	48	527	527
	FB1	200	300	53.12	402	402	252	48	527	527
	B7	75	150	37	14	151	131	22	190	470
	1B	200	200	54.8	143	143	152	48	410	410
	1C	200	200	54.8	143	143	152	48	410	410
	2B	200	200	54.8	253	143	152	48	410	410
	2C	200	200	54.8	253	143	152	48	410	410

Reference	Specimen name	Concrete			Steel reinforcement					
		b [mm]	h [mm]	f_c [MPa]	A_s [mm^2]	A'_s [mm^2]	d_s [mm]	d'_s [mm]	f_y [MPa]	f'_y [MPa]
	2D	200	200	54.8	253	143	152	48	410	410
	3B	200	200	54.8	396	143	152	48	410	410
	3C	200	200	54.8	396	143	152	48	410	410
	3D	200	200	54.8	396	143	152	48	410	410
[105]	A1	150	300	51.70	792	-	250	-	427	-
	A2	200	200	51.70	792	-	251	-	427	-
	A7	200	200	51.70	792	-	252	-	427	-
	C1	200	200	51.70	792	-	253	-	427	-
	B2	270	400	22.60	900	142	341	54	484	507
	CS1	303	150.8	22.24	157	-	115.3	-	343	-
	GS1	302	151.2	23.41	157	-	117.9	-	343	-
	E	205	455	35	253	-	400	-	456	-
	B1u, 4.5	145	230	39.01	33	-	114	-	517	-
	4	76	127	44.7	33	-	111	-	517	-
	5	76	127	44.7	33	-	112	-	517	-
	6	76	127	44.7	33	-	113	-	517	-
	7	76	127	44.7	33	-	114	-	517	-
	8	76	127	44.7	33	-	115	-	517	-
	CP1	301.5	150.5	28.05	314	-	117.4	-	343	-
	CP2	303.6	151.9	39.09	314	-	111.3	-	343	-
	CP3	302.7	150	13.11	157	-	108.2	-	343	-
	CP5	304	149	26.56	157	-	117.4	-	355	-
[50]	Cantilever 1U	100	100	64	157.1	226.2	90	10	350	350
	Cantilever 1A	100	100	64	157.1	226.2	90	10	350	350
	Cantilever 2U	100	100	64	157.1	226.2	90	10	350	350
	Cantilever 4U	100	100	64	157.1	226.2	90	10	350	350
	Cantilever 5U	100	100	64	157.1	226.2	90	10	350	350
	Cantilever 2A	100	100	64	157.1	226.2	90	10	350	350
[77]	A950	120	150	32.1	236	57	120	25	384	400
	A1100	120	150	32.1	236	57	120	25	384	400
	A1150	120	150	32.1	236	57	120	25	384	400
	B1	120	150	44.6	57	57	120	27	400	400
	B2*	120	150	44.6	628	57	120	20	466	400
	C5*	120	150	25.1	236	57	140	5	384	400
	C10*	120	150	25.1	236	57	135	10	384	400
	C20*	120	150	25.1	236	57	125	20	384	400

*Not used for the bond strength models assessment.

Table A.4. Geometrical and mechanical characteristics of the FRP strengthening used for the RC beams tested in bending (Table A.3).

Reference	Specimen name	FRP strengthening							Test results	
		FRP	n_f	t_f	b_f	l_b	E_f	f_f	P_u	l_e
				[mm]	[mm]	[mm]	[MPa]	[MPa]	[kN]	[mm]
[9]	AF.2	C_S	2	0.167	75	1100	240000	3500	83.00	-
	AF.2-1	C_S	2	0.167	75	1200	240000	3500	85.70	-
	AF.4	C_S	2	0.167	75	1400	240000	3500	111.00	-
	DF.1	C_S	1	0.167	75	1400	240000	3500	118.00	-
[46]	F5	C_L	1	1.2	120	2030	155000	2400	100.00	-
	F6	C_L	1	1.2	120	2030	155000	2400	103.00	-
	F7	C_L	1	1.2	120	1876	155000	2400	97.50	-
	F8	C_L	1	1.2	120	1876	155000	2400	64.00	-
	F9	C_L	1	1.2	120	1700	155000	2400	62.00	-
	F10	C_L	1	1.2	120	1700	155000	2400	82.00	-
[91]	A4	C_S	4	0.2	150	1930	127000	1532	61.90	-
	A5	C_S	4	0.2	150	1930	127000	1532	63.20	-
	A6	C_S	6	0.2	150	1930	127000	1532	59.40	-
	A7	C_S	6	0.2	150	1930	127000	1532	70.60	-
	A8	C_S	4	0.2	150	1930	127000	1532	65.20	-
	A9	C_S	4	0.2	150	1930	127000	1532	63.90	-
	A10	C_S	4	0.2	150	1930	127000	1532	67.50	-
	A11	C_S	4	0.2	150	1930	127000	1532	69.40	-
	B3	C_S	2	0.2	150	1930	127000	1532	55.20	-
	B4	C_S	2	0.2	150	1930	127000	1532	52.50	-
	B5	C_S	6	0.2	150	1930	127000	1532	69.70	-
	B6	C_S	6	0.2	150	1930	127000	1532	69.60	-
	B7	C_S	12	0.15	150	1930	127000	1532	59.10	-
	B8	C_S	12	0.15	150	1930	127000	1532	61.60	-
	C3	C_S	2	0.2	150	1930	127000	1532	74.90	-
	C4	C_S	2	0.2	150	1930	127000	1532	77.52	-
	C5	C_S	6	0.2	150	1930	127000	1532	103.10	-
	C6	C_S	6	0.2	150	1930	127000	1532	101.40	-
	C7	C_S	12	0.15	150	1930	127000	1532	87.10	-
	C8	C_S	12	0.15	150	1930	127000	1532	86.70	-
[97]	DF.2	C_S	2	0.167	75	1400	240000	3500	60.30	-
	DF.3	C_S	3	0.167	75	1400	240000	3500	60.00	-
	DF.4	C_S	4	0.167	75	1400	240000	3500	62.80	-
	AF3	C_S	2	0.167	75	1300	240000	3500	48.30	-
	CF2-1	C_S	2	0.167	75	1300	240000	3500	52.40	-
	CF3-1	C_S	2	0.167	75	1300	240000	3500	59.10	-
	CF4-1	C_S	2	0.167	75	1300	240000	3500	70.10	-
	VR5	C_S	4	0.11	120	2200	230000	3400	51.10	-
	VR6	C_S	4	0.11	120	2200	230000	3400	50.30	-
	VR7	C_S	7	0.11	120	2200	230000	3400	62.10	-
	VR8	C_S	7	0.11	120	2200	230000	3400	62.00	-
	VR9	C_S	10	0.11	120	2200	230000	3400	64.80	-

Reference	Specimen name	FRP strengthening							Test results	
		FRP	n_f	t_f	b_f	l_b	E_f	f_f	P_u	l_e
				[mm]	[mm]	[mm]	[MPa]	[MPa]	[kN]	[mm]
	VR10	C_S	10	0.11	120	2200	230000	3400	68.50	-
	A3	C_S	3	0.165	150	2130	230000	3400	86.10	-
	A8	C_S	6	0.165	75	2130	230000	3400	98.20	-
	C2	C_S	3	0.165	150	2130	230000	3400	79.30	-
	C	G_L	1	4.76	152	2032	11720	161	55.40	-
	D	G_L	1	4.76	151	2032	11720	161	59.60	-
	G	G_L	1	4.19	152	2438	10340	184	62.90	-
	I	C_L	1	4.06	150	2032	27580	319	50.60	-
	M	C_L	1	1.27	152	2438	117900	1489	72.10	-
	B2	G_L	1	1.2	80	860	49000	1078	17.00	-
	B3	G_L	1	1.2	30	860	49000	1078	12.30	-
	B4	G_L	1	1.6	60	860	49000	1078	17.50	-
	B6	C_L	1	1.2	80	860	118500	987	20.40	-
	1Au	C_L	1	0.5	90	860	111000	1273	19.80	-
	1Bu	C_L	1	0.7	65	860	111000	1273	18.30	-
	1B2u	C_L	1	0.7	65	860	111000	1273	18.20	-
	1Cu	C_L	1	1	45	860	111000	1273	16.00	-
	2Au	C_L	1	0.5	90	860	111000	1273	19.30	-
	2Bu	C_L	1	0.7	65	860	111000	1273	17.00	-
	2Cu	C_L	1	1	45	860	111000	1273	17.80	-
	3Au	C_L	1	0.5	90	861	111000	1273	19.50	-
	3Bu	C_L	1	0.7	65	862	111000	1273	17.30	-
	3Cu	C_L	1	1	45	863	111000	1273	15.40	-
	B1U, 2.3	C_L	1	1.28	90	2120	115000	1284	50.20	-
	P2	C_L	1	1.2	100	2400	150000	2400	68.00	-
	P3	C_L	1	1.2	100	2400	150000	2400	71.10	-
	P4	C_L	1	2.4	100	2400	150000	2400	78.00	-
	P5	C_L	1	2.4	100	2400	150000	2400	79.50	-
	2	G_L	1	1.32	150	800	19720	259	53.00	-
	4	G_L	1	1.32	150	1100	19720	259	65.40	-
	5	G_L	1	2.64	150	1400	19720	259	79.40	-
	6	G_L	1	1.32	150	1100	19720	259	63.10	-
	7	G_L	1	1.32	150	800	19720	259	53.90	-
	B	G_L	1	6	152	4265	372300	400	125.00	-
	SB1	C_L	1	1.4	120	3300	155000	2400	71.40	-
	SB2	C_L	1	1.4	120	3200	155000	2400	75.50	-
	SB3	C_L	1	1.4	120	3000	155000	2400	73.90	-
	MB1	C_L	1	1.4	120	3300	210000	2000	79.60	-
	HB1	C_L	1	1.4	100	3300	300000	1400	80.10	-
	FB1	C_L	1	2.4	150	3300	95000	1800	74.40	-
	B7	C_L	1	1.2	50	1480	150000	2400	12.50	-
	1B	C_L	1	0.45	200	2740	138000	2206	40.10	-
	1C	C_L	1	0.45	200	2740	138000	2206	35.60	-
	2B	C_L	1	0.45	200	2740	138000	2206	49.00	-

Reference	Specimen name	FRP strengthening							Test results	
		FRP	n_f	t_f	b_f	l_b	E_f	f_f	P_u	l_e
				[mm]	[mm]	[mm]	[MPa]	[MPa]	[kN]	[mm]
	2C	C_L	1	0.45	200	2740	138000	2206	35.60	-
	2D	C_L	1	0.45	200	2740	138000	2206	40.10	-
	3B	C_L	1	0.45	200	2740	138000	2206	54.50	-
	3C	C_L	1	0.45	200	2740	138000	2206	54.10	-
	3D	C_L	1	0.45	200	2740	138000	2206	54.30	-
[105]	A1	C_S	3	0.165	150	2130	230000	3400	86.10	-
	A2	C_S	6	0.165	75	2130	230000	3400	98.20	-
	A7	C_S	3	0.165	150	2130	230000	3400	79.30	-
	C1	C_S	1	0.165	150	2130	230000	3400	72.80	-
	B2	C_S	2	0.165	150	2130	230000	3400	84.90	-
	CS1	C_S	2	0.165	75	2130	230000	3400	86.10	-
	GS1	G_S	1	0.165	150	2130	230000	3400	77.20	-
	E	G_L	1	6	152	4265	37200	400	32.50	-
	B1u, 4.5	C_L	1	1.28	90	4320	115000	1284	30.00	-
	4	C_L	1	0.65	63.2	1070	186000	1450	14.80	-
	5	C_L	1	0.65	63.2	1070	186000	1450	15.30	-
	6	C_L	1	0.9	63.3	1070	186000	1450	14.00	-
	7	C_L	1	0.9	63.3	1070	186000	1450	12.80	-
	8	C_L	1	1.9	63.9	1070	186000	1450	18.70	-
	CP1	C_L	1	1.2	50	900	165000	2800	19.95	-
	CP2	C_L	1	12.2	50	900	165000	2800	17.58	-
	CP3	C_L	1	1.2	50	900	165000	2800	13.31	-
	CP5	C_L	1	1.2	50	900	165000	2800	10.00	-
[50]	Cantilever 1U	C_L	1	0.82	67	920	111000	1414	16.45	-
	Cantilever 1A	C_L	1	0.82	67	920	111000	1414	32.45	-
	Cantilever 2U	C_L	1	0.82	67	920	111000	1414	19.31	-
	Cantilever 4U	C_L	1	0.82	67	920	111000	1414	15.43	-
	Cantilever 5U	C_L	1	0.82	67	920	111000	1414	11.33	-
	Cantilever 2A	C_L	1	0.82	67	920	111000	1414	11.59	-
[77]	A950	C_L	1	1.2	80	950	181000	3140	56.2	250
	A1100	C_L	1	1.2	80	1100	181000	3140	57.3	250
	A1150	C_L	1	1.2	80	1150	181000	3140	58.9	250
	B1	C_L	1	1.2	80	1100	181000	3140	49.2	250
	B2*	C_L	1	1.2	80	1100	181000	3140	130.1	220
	C5*	C_L	1	1.2	80	1100	181000	3140	71	240
	C10*	C_L	1	1.2	80	1100	181000	3140	68	240
	C20*	C_L	1	1.2	80	1100	181000	3140	63	240

*Not used for the bond strength models assessment.